Local Imaging of Optoelectronic Properties and Film Degradation in Polymer/Fullerene Solar Cells with Electrostatic Force Microscopy

Phillip Alexander Cox

A dissertation

submitted in partial fulfillment of the

requirements for the degree of

Doctor of Philosophy

University of Washington

2016

Reading Committee:

David S. Ginger, Chair

Munira Khalil

Xiaosong Li

Program Authorized to Offer Degree:

Chemistry

University of Washington

Abstract

Local Imaging of Optoelectronic Properties and Film Degradation in Polymer/Fullerene Solar Cells with Electrostatic Force Microscopy

Phillip Alexander Cox

Chair of the Supervisory Committee:
Professor David S. Ginger
Chemistry

With power conversion efficiencies on the rise, organic photovoltaics (OPVs) hold promise as a next-generation thin-film solar technology. However, both device performance and stability are inextricably linked to local film structure. Methods capable of probing nanoscale electronic properties as a function of film structure are thus a crucial component of the rational design of efficient and robust devices. This dissertation describes the use of three scanning probe methods for studying local charge generation and photodegradation in polymer/fullerene solar cells. First, we show that time-resolved electrostatic force microscopy (trEFM) is capable of resolving local photocurrent from sub-bandgap excitation down to attoampere level currents, a result unattainable by traditional contact-mode methods. We find that the local charging rates measured with trEFM are proportional to external quantum efficiency (EQE) measurements made on completed devices, making trEFM images equivalent to local EQE maps across the entire solar

spectrum. For both phase-segregated and well-mixed MDMO-PPV:PCBM film morphologies, we show that the local distribution of photocurrent is invariant to excitation wavelength, providing local evidence for the controversial result that the probability of generating separated charge carriers does not depend on whether excitons are formed at the singlet state or charge transfer state. Next, we describe how local dissipation imaging can be performed with commercially-available frequency-modulated electrostatic force microscopy (FM-EFM) and show that dissipation maps are highly sensitive to photo-oxidative effects in organic semiconductors. We show that photo-oxidation induced changes in cantilever energy dissipation are proportional to device performance losses. We further develop dissipation imaging by implementing ringdown imaging, which directly measures the quality factor of the cantilever, enabling quantitative dissipation mapping. Using organic photovoltaic materials as a testbed, we study macroscopic device degradation as a function of photooxidation for three different film morphologies. According to EQE measurements, we find that the stability of the macroscopic devices is very sensitive to processing conditions, with films processed with the solvent additive 1,8-diiodooctane being the most stable. At the microscopic level, we compare the evolution of cantilever power dissipation as a function of photochemical degradation for three different polymer/fullerene blend morphologies, and show that the evolution of local power dissipation correlates with device stability. Lastly, we show that cantilever power dissipation increases more rapidly over large fullerene aggregates than in well-mixed polymer/fullerene regions, suggesting that local photochemistry on the fullerene contributes strongly to the dissipation signal.

TABLE OF CONTENTS

LIST OF FIGURES

LIST OF TABLES

ACKNOWLEDGEMENTS

I would like to acknowledge Prof. David S. Ginger, Dr. Rajiv Giridharagopal, Prof. Dean Waldow, Dr. David Moerman, Dr. Micah Glaz, Jeffrey Harrison, Sam Peurifoy, and Torin Dupper.

DEDICATION

This dissertation is dedicated to my parents, John and Diana Cox, who are the most wonderful and supportive parents anyone could ever hope for.

Chapter 1. Introduction

1.1 MOTIVATION

Emerging energy technologies strive toward cost-effective means of producing, storing and delivering energy for a broad range of applications. For years the high cost of silicon solar cells was the driving force behind research on alternative solar materials such as polymer-based organic solar cells or most recently, hugely popular devices made from organometal halide perovskites.[1] But with the price of silicon solar panels now under one dollar per watt,[2] the cost-effectiveness argument for alternative energy materials has become less important. Recently, studies have shown that factors beyond cost are important to consider, such as damage to ecosystem, human health, and resources.[3] In all three categories, the least damaging solar module to produce is the organic solar cell, with the zinc oxide variant of perovskites in a close second. The impact that crystalline and even amorphous silicon solar cells has on these factors is up to an order of magnitude higher, providing ample evidence for continuing research on alternative energy materials.

The materials comprising many low environmental impact electronic devices are Earth-abundant, typically in the form of solutions-processable thin films that can be deposited onto thin or even flexible substrates. The performance of these devices is intimately tied to the morphological structure of the film, with a majority of the underlying electrical processes occurring over the same length scales in which the materials are arranged. Due to this inextricable link between structure and function, methods that can probe electrical responses at the nanoscale have become increasingly more important in the rational design of future functional materials.

The content of this dissertation focuses on organic photovoltaics (OPVs), which have seen significant increases in performance over the past decade, with power conversion efficiencies rising from about 3% in 2001 up to 11.5% for the most recent record-holding single-junction organic solar cell.[4] While these increases have been monumental, efficiencies still lag behind theoretical capabilities and alternative solar technologies, with much left to be understood regarding the underlying processes that govern charge carrier generation and transport, and perhaps most importantly for commercialization, materials breakdown due to photochemical

degradation. In most cases, these properties are profoundly affected by film morphology, or in other words, how the materials in the active layer of the solar cell are intermixed.

1.2 OPV OPERATION

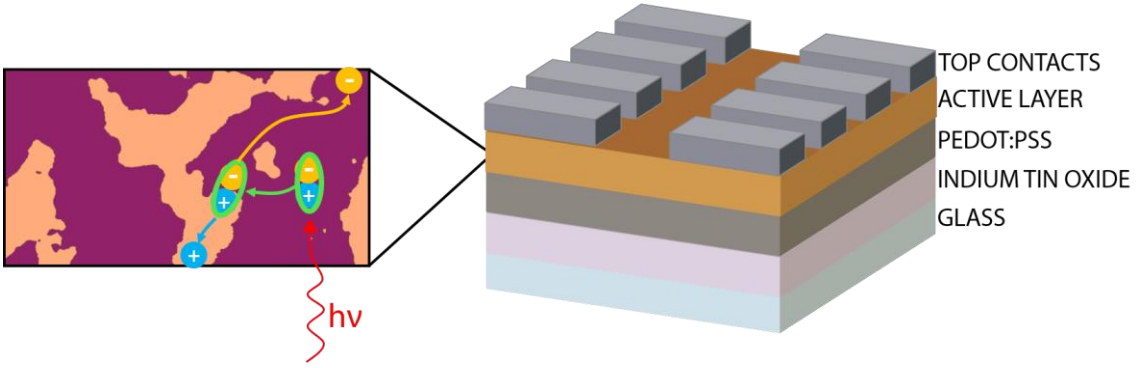

Figure 1.1 (Right) A basic diagram of a bulk heterojunction organic solar cell. The basic architecture for all devices in this dissertation follows the Glass/ITO/PEDOT:PSS/Active Layer/Top Contact structure. The ITO serves as the bottom electrode, with PEDOT:PSS acting as a hole-transporting layer. (Left) A photon is absorbed in the active layer forming an electron-hole pair (exciton). The exciton diffuses to a donor/acceptor interface where the charge carriers separate and diffuse to their respective electrodes.

The active layer in OPVs is typically composed of two semiconducting materials, the most common being an electron donating polymer (donor) and an electron accepting fullerene (acceptor).[5] The two components are mixed in solution and cast into a thin film on a conductive substrate which is most commonly a transparent conducting oxide such as indium tin oxide (ITO) on glass. The resulting active layer film forms a bulk heterojunction, which is a complex mixture of varying degrees of phase separation, with domain sizes ranging in length scales from tens of nanometers to microns, depending on a broad range of factors including (but not limited to) chemical structure, casting temperature, solvent choice or the use of thermal annealing. Upon absorption of a photon, a Coulombically bound electron-hole pair called an exciton is formed on the light-absorbing materials within the active layer (shown in Figure 1.1, as well as a diagram of the basic device architecture for all devices studied here.). Since the binding energy of the exciton is greater than kT (on the order of 500 meV),[6] the exciton must reach a donor/acceptor interface

where the offset in energy levels of the two materials and existence of interfacial energy states drives exciton dissociation. The lifetime of the exciton is every short and will recombine if it does not diffuse to a donor/acceptor interface within 10 - 20 nm.[1] Thus, an efficient film will have a morphology with a great degree of intermixing between the two materials. Additionally, since photogenerated charge carriers can take part in photochemical reactions with the organic components of the active layer,[7] film morphology also has a profound effect on device stability.[8] Instrumentation that can measure these electrical processes over the same length scales as film morphology is essential for a better understanding of the device structure-function relationship.

1.3 Atomic Force Microscopy

Atomic force microscopy (AFM) can be employed in a number of modes, the two most common being contact mode and AC mode. In contact mode, the probe, a small metal cantilever normally 100 – 200 μm in length with a tip at the end that comes to a point of ~20 nm, is raster scanned with the tip in contact with the sample surface. As the probe moves over tall and short features on the sample surface, the cantilever bends up or down depending on the height of the topological feature. A laser is reflected off the back of the cantilever and the signal is collected by a four-quadrant photodiode, which changes in magnitude depending on the amount of bend in the cantilever and is directly related to the topography of the sample. Contact mode AFM can be used to probe electronic sample properties as well by using a conductive tip as the top electrode to locally inject charges upon applied bias (cAFM) or collect current (pcAFM) generated in an electronically active sample. cAFM and pcAFM thus provide local information regarding charge injection, transport, and generation in (semi)conducting materials.[9, 10] The drawback of these methods is the potential for causing mechanical damage to a soft sample material, such as the polymers used in OPVs, when the sharp metal tip of the cantilever is dragged across the surface of the material. Therefore, to image soft materials such as those described later in this dissertation, non-contact AFM modes are employed.

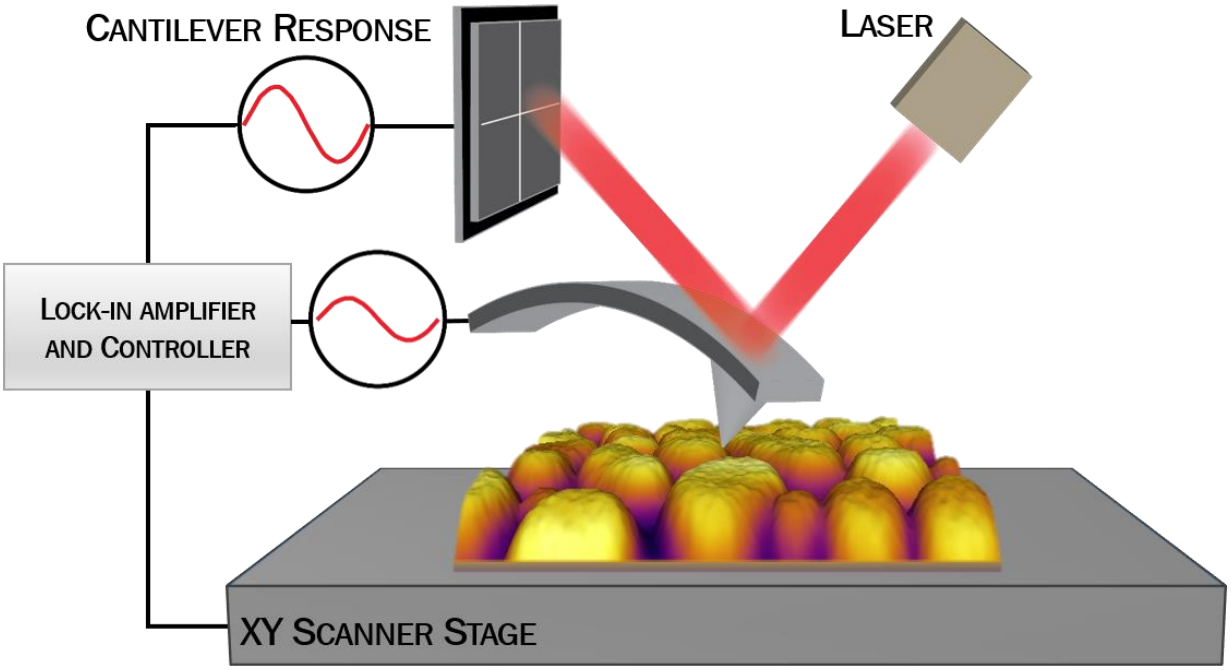

Figure 1.2 A basic diagram of AC mode atomic force microscopy. The cantilever oscillates at a particular amplitude by applying an AC signal to a piezoelectric element coupled to the cantilever, and as the sample is raster scanned underneath the tip, changes in oscillation amplitude arise due to variations in sample topography. The cantilever response is measured by reflecting a laser off the back of the cantilever and collecting the signal with a photodiode. The system uses a feedback loop keep the tip-sample separation constant.

In AC mode AFM, depicted in Figure 1.2, the cantilever is oscillated at its resonance frequency at a particular amplitude and phase. As the tip is brought near the sample surface, repulsive van der Waal's forces cause a decrease in oscillation amplitude. Taller features in the sample surface will damp oscillation amplitude to a greater extent, while short features damp oscillation less. The system uses a feedback loop to adjust the separation between tip and surface in order to keep the oscillation amplitude constant. These changes in separation distance are directly related to the topography of the sample. Much like contact mode AFM, conductive cantilevers can be used in AC mode operation, though normally the tip is backed away further from the surface to interact solely through electrostatic interactions, and in this case is more commonly referred to as non-contact mode. However, rather than directly collecting current at the

tip, differences in the electrostatic forces between tip and sample cause changes in oscillation frequency, amplitude, and phase.[11] Depending on the operation conditions of the instrumentation, many different materials properties can be probed in non-contact AFM using a conductive cantilever, the umbrella term for which is electrostatic force microscopy (EFM). Many variations of EFM are employed to measure different materials properties, such as time-resolved electrostatic force microscopy (trEFM)[12] for local quantum efficiency measurements and charge transport properties, and scanning Kelvin probe microscopy for sample work function and charge carrier recombination.[13]

1.4 SUMMARY

This dissertation describes three EFM methods for studying optoelectronic properties and degradation in polymer/fullerene solar cells: time-resolved EFM, dissipation imaging *via* frequency-modulated EFM, and dissipation imaging *via* cantilever ringdown. In each case, the general experimental setups are identical, but minor variations in AFM operation give rise to measurement of different solar cell properties. Detailed descriptions of each technique are included in their respective chapters.

First we describe the use of trEFM for studying the sub-bandgap charge transfer state in polymer/fullerene solar cells, an electronic state that plays a critical role in charge carrier separation. We show that local trEFM measurements are proportional to device external quantum efficiency (EQE) across the solar spectrum, making trEFM a powerful local EQE probe even for the low EQEs associated with sub-gap excitation. We further compare the above- and below-gap excitation properties for two morphologies of the MDMO-PPV:PCBM system, and find that while the local distribution of EQEs depends on film composition, it does not depend on excitation wavelength.

Next we present the use of frequency-modulated electrostatic force microscopy (FM-EFM) for mapping cantilever power dissipation in photo-oxidized organic semiconductor materials. FM-EFM is a commercially available variant of EFM that utilizes a feedback loop to keep the cantilever at resonance. When this condition is satisfied, the amplitude of the cantilever is inversely proportional to cantilever power dissipation. We show that local dissipation maps are highly

sensitive to photo-oxidative changes in polymer/fullerene solar cells, and that the use of the processing additive 1,8-diiodooctane improves the stability of PTB7:$PC_{71}BM$ solar cells.

Lastly, we build upon on our work with dissipation imaging, this time developing an imaging method for quantitative measurement of cantilever energy dissipation, enabling image to image and even sample to sample comparisons. We accomplish this by measuring the ringdown time of an oscillating conductive cantilever, a property that is directly related to cantilever energy dissipation. We show that when decreasing charge carrier density in photodegraded blends of PTB7:$PC_{71}BM$ is accounted for, the dissipation per mobile charge carrier increases throughout the functional lifetime of the device, doing so at a faster rate in phase-separated polymer/fullerene blends. By taking multiple dissipation maps as a function of device degradation, we show that the largest photochemical changes occur at the fullerene aggregates, providing local evidence for the important role fullerene plays in device breakdown.

1.5 REFERENCES

1. Dou, L.; You, J.; Hong, Z.; Xu, Z.; Li, G.; Street, R. A.; Yang, Y. 25th Anniversary Article: A Decade of Organic/Polymeric Photovoltaic Research. *Adv. Mater. (Weinheim, Ger.)* **2013,** *25*, 6642-6671.
2. EnergyTrend http://pv.energytrend.com/pricequotes.html (02/05/2016),
3. Gong, J.; Darling, S. B.; You, F. Perovskite Photovoltaics: Life-Cycle Assessment of Energy and Environmental Impacts. *Energy & Environmental Science* **2015,** *8*, 1953-1968.
4. NREL http://www.nrel.gov/ncpv/images/efficiency_chart.jpg (02/04/2016),
5. Thompson, B. C.; Frechet, J. M. J. Organic Photovoltaics - Polymer-Fullerene Composite Solar Cells. *Angew. Chem., Int. Ed. Engl.* **2008,** *47*, 58-77.
6. Kippelen, B.; Bredas, J.-L. Organic Photovoltaics. *Energy & Environmental Science* **2009,** *2*, 251-261.
7. Jorgensen, M.; Norrman, K.; Gevorgyan, S. A.; Tromholt, T.; Andreasen, B.; Krebs, F. C. Stability of Polymer Solar Cells. *Adv. Mater. (Weinheim, Ger.)* **2012,** *24*, 580-612.
8. Cox, P. A.; Waldow, D. A.; Dupper, T. J.; Jesse, S.; Ginger, D. S. Mapping Nanoscale Variations in Photochemical Damage of Polymer/Fullerene Solar Cells with Dissipation Imaging. *ACS Nano* **2013,** *7*, 10405-10413.
9. Pingree, L. S. C.; Reid, O. G.; Ginger, D. S. Imaging the Evolution of Nanoscale Photocurrent Collection and Transport Networks During Annealing of Polythiophene/Fullerene Solar Cells. *Nano Lett.* **2009,** *9*, 2946-2952.
10. Coffey, D. C.; Reid, O. G.; Rodovsky, D. B.; Bartholomew, G. P.; Ginger, D. S. Mapping Local Photocurrents in Polymer/Fullerene Solar Cells with Photoconductive Atomic Force Microscopy. *Nano Lett.* **2007,** *7*, 738-744.
11. Silveira, W. R.; Marohn, J. A. Microscopic View of Charge Injection in an Organic Semiconductor. *Phys. Rev. Lett.* **2004,** *93*, 116104.

12. Coffey, D. C.; Ginger, D. S. Time-Resolved Electrostatic Force Microscopy of Polymer Solar Cells. *Nat. Mater.* **2006,** *5*, 735-740.
13. Shao, G.; Glaz, M. S.; Ma, F.; Ju, H.; Ginger, D. S. Intensity-Modulated Scanning Kelvin Probe Microscopy for Probing Recombination in Organic Photovoltaics. *ACS Nano* **2014,** *8*, 10799-10807.

Chapter 2. Imaging Charge Transfer State Excitations in Polymer/Fullerene Solar Cells with Time-Resolved Electrostatic Force Microscopy[1]

2.1 INTRODUCTION

Organic photovoltaics (OPVs) offer many potential advantages as a next-generation thin-film solar technology. They have been demonstrated with over 10% power conversion efficiencies,[1, 2] are made from inherently earth-abundant and non-toxic materials, can be processed from greener, non-halogenated solvents,[3, 4] and accelerated stability testing has predicted lifetimes exceeding seven years.[5] Furthermore, there is seemingly still room to improve overall performance, as a number of studies have estimated that the ultimate power conversion efficiency limits for OPVs should be in the range of 20-27%.[6, 7]

However, continued improvements in OPV performance will require better understanding of the fundamental recombination loss mechanisms taking place in organic semiconductors.[7] Currently, the most efficient OPVs comprise a donor and acceptor material arranged in a bulk heterojunction morphology that has a profound effect on charge generation, recombination, transport, and hence device efficiency.[8-10] In addition, many authors have identified the charge transfer (CT) state that forms at the donor/acceptor interface as having a key influence on device performance.[7, 11-15] For instance, the V_{oc} of organic solar cells shows a strong empirical correlation with the energy of the CT state.[16-19]

Because of the importance of morphology, there has been a great deal of work both to characterize the structure of polymer/fullerene blends, as well as to develop methods that can correlate local morphology with local variations in device performance.[20-27] Likewise, researchers have used a wide range of optical spectroscopic probes and device measurement techniques to characterize the energetics and kinetics of sub-gap CT states in OPV blends,[12, 28-32] as well as sub-gap excitations in related nanostructured solar materials, such as quantum dot solar cells[33, 34] and

[1] This chapter adapted from Phillip A. Cox, Micah S. Glaz, Jeffrey S. Harrison, Sam R. Peurifoy, David C. Coffey, David S. Ginger, *J. Phys. Chem. Lett.*, **2015**, 6 (15), pp 2852-2858, DOI: 10.1021/acs.jpclett.5b01360

organometal halide perovskites.[35] Despite the large body of work demonstrating substantial spatial heterogeneity in charge generation, recombination, and transport associated with above-gap photoexcitation of OPV blends,[36-43] performing similar experiments to map spatial variations in CT state photocurrents is challenging because of the extremely small EQEs (10^{-3} – 10^{-6} or lower) associated with exciting the weakly allowed CT transition. Indeed, measuring photocurrents from CT states in macroscopic devices typically requires sensitive lock-in[31] or Fourier-Transform Photocurrent Spectroscopy methods.[30, 44]

Here we demonstrate that time-resolved electrostatic force microscopy (trEFM)[23, 25, 45] can be used to map local variations in EQE across the solar spectrum, including direct sub-gap excitation of the CT state. We compare trEFM maps taken with above- and below-gap excitation and show that while morphology influences local variations in carrier generation and collection, excitation wavelength does not.

trEFM is a non-contact atomic force microscopy technique that measures capacitive force gradients and surface potentials between the sample and a conductive AFM cantilever.[23, 24] Non-contact scanning probe methods like trEFM are useful for imaging soft samples as they greatly reduce the chance of damaging both the cantilever tip and thin film components, enabling repeated imaging of the same area under various conditions. As such, we have previously used trEFM to assess the role of morphology on both performance and photochemical damage in organic photovoltaics and we have demonstrated that photoinduced charging rates in trEFM are proportional to the external quantum efficiency of bulk devices under a range of conditions in model polymer/polymer blends.[23, 25, 45]

Figure 2.1A shows a schematic of the trEFM setup we used for probing sub-gap CT excitation. Briefly, we photoexcite a partially-completed polymer/fullerene solar cell through the transparent bottom substrate (indium tin oxide coated glass) with a short (4 ms) LED pulse that creates charge carriers in the active layer. A positive bias on the AFM cantilever causes negative charge carriers to move toward the sample surface, and these carriers lead to a decrease in the resonance frequency of the AFM cantilever.[46, 47] By tracking the frequency as a function of time, we can thus determine how rapidly the photoinduced carrier population builds up at the film surface under the AFM tip. The experiment essentially measures the time it takes to charge the tip-

sample capacitor with the local photocurrent generated under the tip. The rise times are thus associated with the magnitude of the local EQE/photocurrent (*not* the exciton dissociation event itself, which typically occurs on femtosecond scales[29, 48] in these materials).

Figure 2.1B shows a raw data trace of a single pixel in an image during the trEFM measurement cycle for two different light intensities. The rise time of interest is the one following the LED pulse as indicated in the figure. In this example, the tip-sample junction charges faster with a brighter pulse. However, for a constant light intensity, local variations in EQE lead to variation in the charging rate between pixels.[23] A trEFM image is generated by plotting the inverse tau from an exponential decay fit taken at each pixel location.

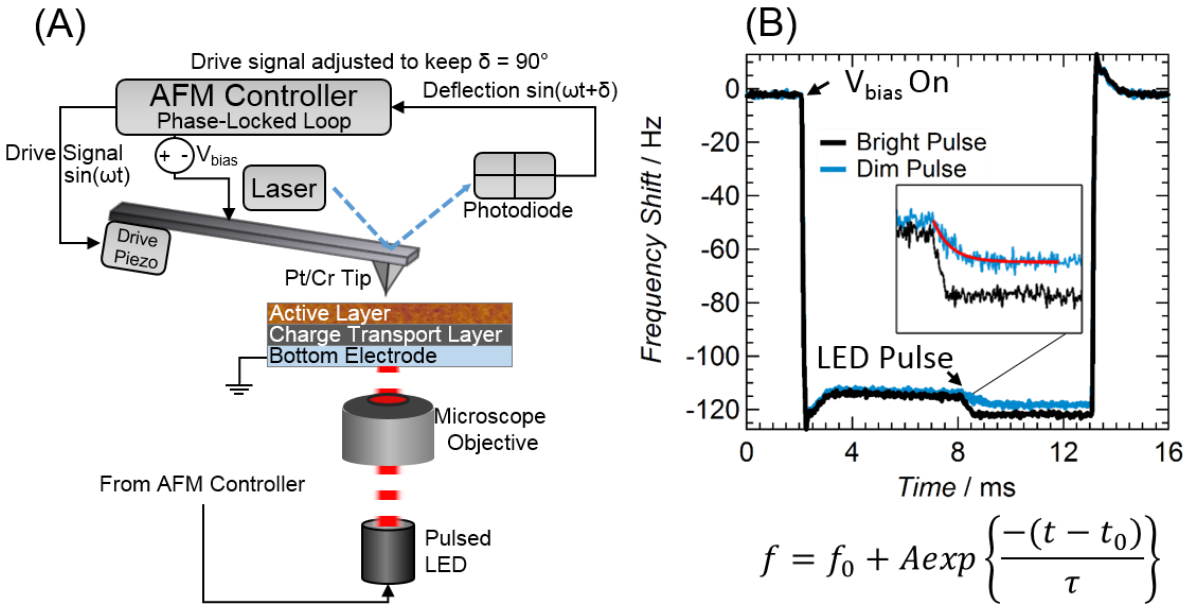

Figure 2.1 (A) Schematic of the time-resolved electrostatic force microscopy technique. (B) A raw data trace plotting cantilever frequency shift vs. time during a measurement cycle at a single pixel as the measurement voltage and then illumination are turned on. We fit the frequency shift vs. time after the LED pulse to the exponential decay (red trace) function shown, where the inverse of tau is characteristic of the local photocharging rate of the tip-sample junction, a value that is proportional to local EQE.

In this study we use the model system poly[2-methoxy-5-(3',7'-dimethyloctyloxy)-1,4-phenylenevinylene] (MDMO-PPV):[6,6]-phenyl C_{61} butyric acid methyl ester (PCBM). The film

morphology of this blend is easily tailored by choice of casting solvent,[8] and both the morphology and charge transfer state properties of MDMO-PPV:PCBM devices have been studied in detail,[8, 11, 49] making it an ideal system to test the ability of trEFM to resolve charge carriers arising from both above- and below-gap photoexcitation.

2.2 RESULTS

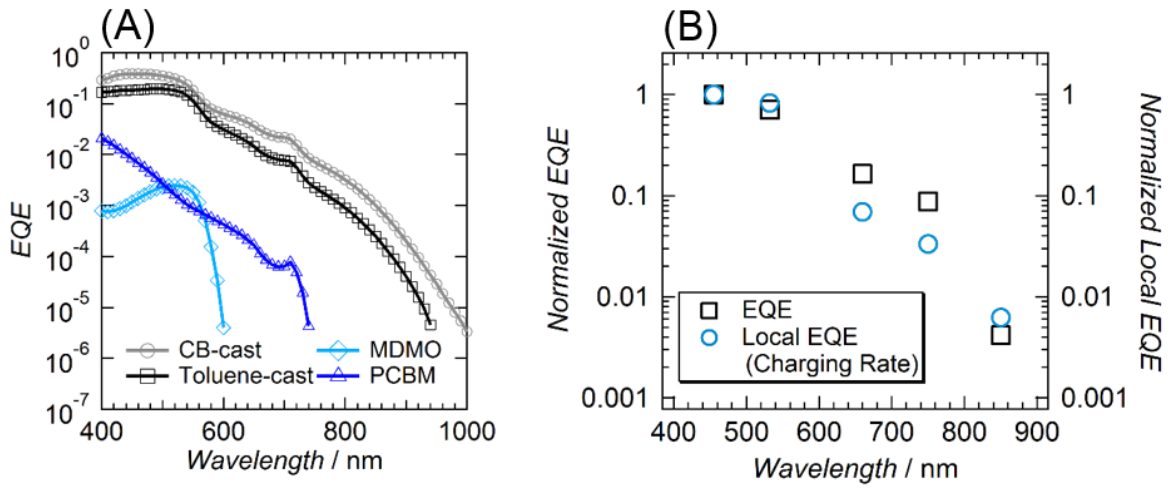

Figure 2.2 (A) Lock-in amplifier-detected EQE of neat MDMO-PPV, neat PCBM, 1:4 MDMO-PPV:PCBM blend cast from chlorobenzene, and 1:4 MDMO-PPV:PCBM cast from toluene. (B) Comparison between bulk device EQE and photon-flux normalized trEFM charging rates (local EQE) as a function of wavelength for a device cast from chlorobenzene.

Figure 2.2A shows the lock-in detected external quantum efficiencies of macroscopic solar cells made from neat MDMO-PPV, neat PCBM, and blends of the two materials in a 1:4 wt/wt ratio cast from both chlorobenzene and toluene. The pure MDMO-PPV alone shows an EQE peak around ~550 nm before sharply dropping off by 600 nm, while PCBM exhibits a longer tail but drops off steeply at 750 nm. As expected, the MDMO-PPV:PCBM blends show higher overall EQEs that resemble a superposition of the MDMO-PPV and PCBM spectra at shorter wavelengths, but include a broad red tail in the near IR.[11] This sub-gap EQE tail is broader than the sum of the individual components, and arises due to sub-gap excitation directly into the interfacial CT states comprising an electron on a fullerene and a hole on the MDMO-PPV.[8]

We have previously shown that the trEFM charging rates correlate well with EQE for both pristine and photo-oxidized films.[23, 45] Here we explore if this relationship holds true for photocarriers generated via sub-gap excitation of CT states by comparing the wavelength-dependence of the device EQE and trEFM charging rate. Figure 2.2B (blue circles) plots the wavelength-dependent, photon-flux normalized trEFM charging rates measured on an MDMO-PPV:PCBM blend cast from chlorobenzene. Figure 2.2B also plots the device EQEs measured at the same wavelengths (see Appendix Figure A.1 and A.2). The close agreement between the traces for the device EQE and the trEFM charging rates as they both change by over two orders of magnitude as the wavelength changes from 455-850 nm shows that trEFM can indeed be used to map local EQEs, even for direct excitation of sub-gap CT states. While the EQE for this CB blend is ~0.1% (10^{-3}) at 850 nm, we can use trEFM to measure down to levels as low as 0.001% (10^{-5}) (Appendix Figure A.6). Recording a local sub-gap photocurrent with conventional photoconductive AFM would require measurement of attoAmpere level currents. This level of detection is made possible by the sensitivity of EFM methods to local force gradients: under favorable conditions, sensitivity to single charges is even possible.[50]

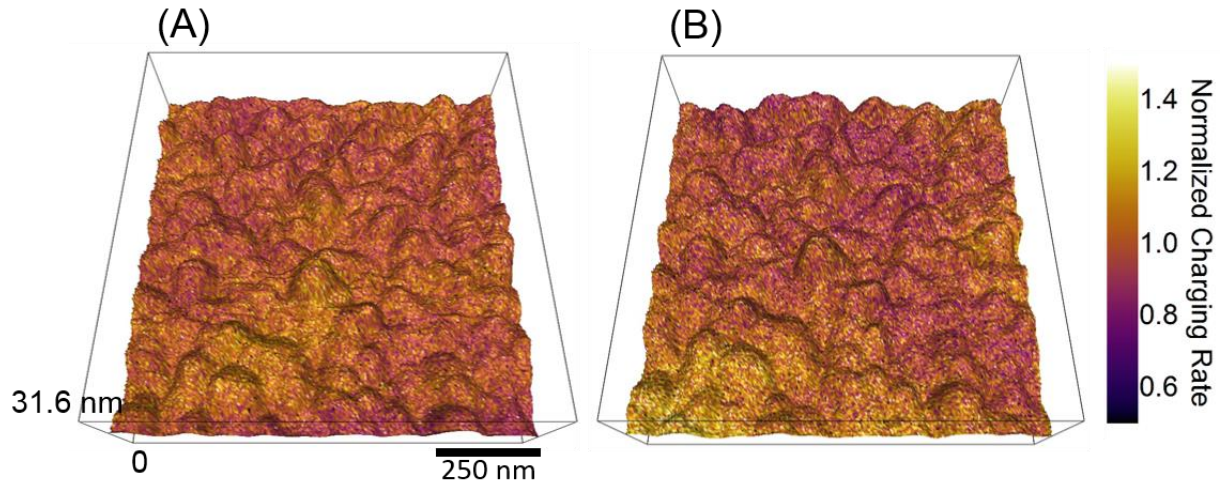

Figure 2.3 (A) Normalized singlet state charging rate (532 nm LED) and (B) CT state charging rate (850 nm LED with 850 nm longpass filter) overlaid on film topography of a 1:4 MDMO-PPV:PCBM film cast from chlorobenzene.

Figures 2.3A and 2.3B show charging rate images taken at 532 and 850 nm excitation overlaid on AFM topography of a 1:4 MDMO-PPV:PCBM film cast from chlorobenzene (frequency shift images included in Appendix Figure A.4). The morphology consists of small features on the order of 30-60 nm with a relatively smooth surface roughness. Figure 2.3A shows a typical charging rate map where the sample was photoexcited with a 532 nm LED. We normalized this image (and all subsequent images presented here), by dividing every pixel by the average charging rate. This process highlights spatial variations relative to the film average. However, for both above- and below-gap excitation we find little to no local variation in charging rate for films cast from chlorobenzene, regardless of excitation wavelength or local morphology. This lack of observable variation is expected given the very small scale of the features in a chlorobenzene-cast MDMO-PPV:PCBM blend. To explore spatial variations in photocurrent collection more easily as a function of wavelength, we next turn to examine blends spin-coated from toluene.

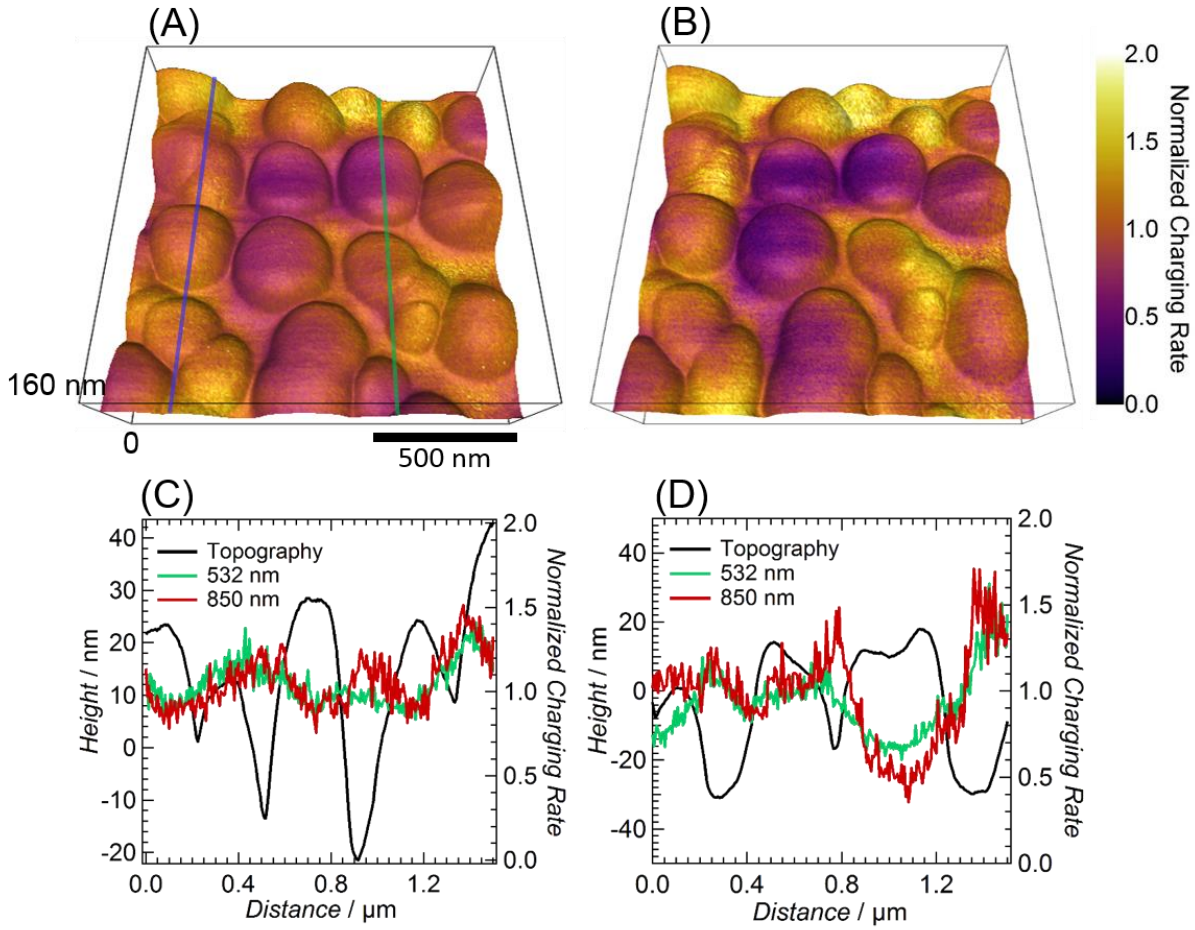

Figure 2.4 (A) Normalized singlet state charging rate (532 nm LED) and (B) CT state charging rate (850 nm LED with 850 nm longpass filter) overlaid on film topography of a 1:4 MDMO-PPV:PCBM film cast from toluene. (C) and (D) Line traces of topography height and charging rates at both 532 nm and 850 nm excitation taken at the blue (C) and green (D) lines shown in (A).

Figures 2.4A and B show trEFM charging rate images taken at 532 nm and 850 nm overlaid on the AFM topography for a 1:4 MDMO-PPV:PCBM film cast from toluene (frequency shift images included in Supporting Figure A.3). This blend forms films consisting of large aggregates, roughly 250-500 nm in diameter, separated by flat valleys. The structure of MDMO-PPV:PCBM devices cast from toluene has been meticulously studied and reported elsewhere.[8, 51, 52] Briefly, the large aggregates are PCBM domains, which can be covered with a mixed MDMO-PPV:PCBM capping layer. The valleys are regions of mixed MDMO-PPV and PCBM. For above-gap photoexcitation, charging mainly occurs in between, and at the edges of fullerene aggregates, as

well as on top of some of the aggregates. These locations are where there is the most polymer, which is responsible for most absorption at 532 nm. Photoconductive-AFM (pcAFM) measurements show that current collection mainly occurs at the aggregate boundaries but not in the flat, mixed domains.[36] While the structure and overall charging rate trends in these trEFM images are generally consistent with pcAFM on the same films, the trEFM images show subtle differences that we attribute to the ability of trEFM to detect and resolve photocurrent variations in the areas between fullerene aggregates, a result that is difficult to achieve with contact-mode pcAFM (see Appendix Figure A.7).

Figure 2.4B shows similar charging rate images obtained by exciting only the CT state with an 850 nm LED and 850 nm longpass filter. Surprisingly, the trEFM images in Fig. 2.4A and 2.4B are very similar, despite being taken at very different excitation energies. Notably, the line traces shown in Fig. 2.4C and 2.4D show virtually the same spatial variation with small deviations. We attribute the small observed deviations to the result of random noise associated with measuring what is the equivalent of attoAmpere level currents. We provide additional analysis and discussion in Appendix Fig. A.8, showing that the correlation between the images taken with above-gap and below-gap excitation is as high as can be expected between successive AFM scans under these experimental conditions and imperfect spatial matching. We thus take the strong correlation between the two images to be evidence that the local distribution of EQEs is insensitive to excitation wavelength as explained below.

At first, it may seem unexpected that the EQE maps taken at 532 and 850 nm excitation show the same spatial structure. If we *had* observed structure in the trEFM maps that differed systematically between above-gap (excitonic) and below-gap (CT state) excitation as a function of position, it would imply that either the local absorption varies due to local composition or that the local yield of free carriers per absorbed photon (internal quantum efficiency, IQE) changed from region to region depending on excitation wavelength. On the other hand, the lack of change in structure upon change in wavelength implies that either (A) the features at 532 nm and 850 nm share both the same spatial variations in absorption and charge separation (IQE), or (B) the local variations in absorption and IQE are coincidentally inversely proportional everywhere so as to exactly cancel (further discussion provided in Appendix A Section 9). Since the excitonic (above gap) and charge transfer state (below gap) absorptions both involve MDMO-PPV, and it is known

that the MDMO-PPV phases contain molecularly dispersed PCBM,[8, 53] it seems reasonable that both excitonic and CT absorption track MDMO-PPV concentration in this blend. Therefore, we conclude that the probability of forming charge carriers from an absorbed photon must be essentially equal at above- and below-gap photoexcitation. If this was not the case, then to preserve the local distribution in EQEs between singlet and CT excitation, the IQE and EQE would have to coincidentally anti-correlate everywhere in the film. Due to the unlikeliness of this possibility, we propose that IQE is independent of excitation wavelength.

Notably, Vandewal *et al.*[12] recently reported that the internal quantum efficiency (IQE) of a number of polymer/fullerene blends (including MEH-PPV, a polymer closely related to MDMO-PPV) is independent of excitation wavelength. Although we emphasize that our trEFM measurements probe EQE, not IQE, we still conclude that the strong correlation between the EQE maps at above- and below-gap excitation shown in Fig. 2.3 and 2.4 are local evidence consistent with the findings of Vandewal and coworkers. In other words, the only likely way to have the macroscopic IQE be the same at two different wavelengths in a sample with significant spatial heterogeneity is if the microscopic variations in IQE are also independent of excitation wavelength.

2.3 CONCLUSIONS

We have employed time-resolved electrostatic force microscopy to acquire nanoscale images of the charge-transfer state in MDMO-PPV:PCBM solar cells. Over the range of the solar spectrum, even at sub-bandgap wavelengths, we find that the charging rates from trEFM point scans are proportional to the EQE of a bulk device, demonstrating that trEFM can be used as a local probe for EQE, even for very weakly absorbing states, with EQEs as low as 10^{-5}. The high sensitivity of trEFM to local carrier generation makes it ideal for dynamic characterization of a broad range of nanostructured materials, such as intermediate band quantum dot solar cells and singlet fission solar cells where carriers generated from weak sub-gap excitations are of interest. For heterogeneous OPV device morphologies, we found that the charging rates for both above- and below-gap photoexcitation are fastest in areas where MDMO-PPV and PCBM are well mixed, with the slowest charging rates occurring in the pure PCBM phase. These results provide local evidence in support of recent work suggesting that IQE is insensitive to excitation wavelength.

2.4 METHODS

2.4.1 *Device Preparation*

Pre-coated ITO slides (Thin Film Devices, Inc.) were sonicated in sequential solutions of acetone and isopropanol for 20 minutes each and then dried with nitrogen. The substrates were plasma-cleaned for 5 minutes and then immediately spincoated with a ~30 nm layer of PEDOT:PSS (Clevios P VP 4083 Al, H.C. Stark Chemicals) before annealing at 150 °C for 20 minutes under dry nitrogen. MDMO-PPV (synthesized by Lee Park's group, Williams College)[54] and PCBM (nano-c) solutions were created separately in either toluene or chlorobenzene solvent and stirred overnight at 60 °C. In a nitrogen glovebox, 80 µL of 1:4 wt/wt MDMO-PPV:PCBM solution was spincoated onto the PEDOT:PSS layer to a thickness of ~85 nm. For films used in EQE measurements, 80 nm aluminum contacts were thermally evaporated onto the active layer through a shadow mask.

2.4.2 *Device Testing*

External quantum efficiency measurements were performed with a monochromated (Acton Research Corporation Microspec 2300i) 250 W lamp (Princeton Instruments), sourcemeter (Keithley 2400), lock-in amplifier (Stanford Research Systems SR830) and calibrated Si photodiode (OSI-Optoelectronics). A device mask ensured the same 0.0122 cm^2 of light exposure to all devices and the photodiode.

2.4.3 *Atomic Force Microscopy*

AFM measurements were carried out on an Asylum Research MFP-3D Bio atomic force microscope on top of an inverted Nikon Eclipse Ti microscope and Table Stable vibration isolation stage. 75 kHz resonance frequency BudgetSensor silicon cantilevers with a Pt/Cr conductive coating were used. Devices were sealed from the environment in an Asylum Research closed flow cell with a constant stream of dry nitrogen. Excitation light sources were LEDEngin 455, 532, 660, 750, and 850 nm LZ4-series LEDs. The LEDs were attached to a side input of the microscope where they were reflected off one full mirror and then a 50/50 beam splitter (850 used a full mirror) filter cube before going through a 40x Nikon Pan Flour objective. For CT-excitation images, an

850 nm longpass filter (ThorLabs FEL0850) was used in front of the 850 nm LED to ensure no singlet state excitation (see Supporting Figure A.5). In comparing macroscopic EQE to local trEFM measurements, the macroscopic EQEs were weighted to the emission spectra of the LEDs used in the trEFM measurements (see supporting information Fig. A.1). All trEFM images are 256x256 pixels with 10 averages per pixel and fit to the Igor software's built-in exponential decay function with realistic constraints for the time constant. All trEFM imaging and analysis was carried out with our custom Igor code operating within the Asylum Research AFM software.

2.5 ACKNOWLEDGEMENTS

This work was completed under NSF DMR-1306079. The authors thank Dr. David Moerman for helpful discussions.

2.6 REFERENCES

1. You, J.; Dou, L.; Yoshimura, K.; Kato, T.; Ohya, K.; Moriarty, T.; Emery, K.; Chen, C.; Gao, J.; Li, G.*; et al.* A Polymer Tandem Solar Cell with 10.6% Power Conversion Efficiency. *Nat. Commun.* **2013,** *4*, 1446.
2. Liu, Y.; Zhao, J.; Li, Z.; Mu, C.; Ma, W.; Hu, H.; Jiang, K.; Lin, H.; Ade, H.; Yan, H. Aggregation and Morphology Control Enables Multiple Cases of High-Efficiency Polymer Solar Cells. *Nat. Commun.* **2014,** *5*, 5293.
3. Chen, K.-S.; Yip, H.-L.; Schlenker, C. W.; Ginger, D. S.; Jen, A. K. Y. Halogen-Free Solvent Processing for Sustainable Development of High Efficiency Organic Solar Cells. *Org. Electron.* **2012,** *13*, 2870-2878.
4. Chueh, C.-C.; Yao, K.; Yip, H.-L.; Chang, C.-Y.; Xu, Y.-X.; Chen, K.-S.; Li, C.-Z.; Liu, P.; Huang, F.; Chen, Y.*; et al.* Non-Halogenated Solvents for Environmentally Friendly Processing of High-Performance Bulk-Heterojunction Polymer Solar Cells. *Energy Environ. Sci.* **2013,** *6*, 3241-3248.
5. Peters, C. H.; Sachs-Quintana, I. T.; Kastrop, J. P.; Beaupré, S.; Leclerc, M.; McGehee, M. D. High Efficiency Polymer Solar Cells with Long Operating Lifetimes. *Adv. Energy Mater.* **2011,** *1*, 491-494.
6. Giebink, N. C.; Wiederrecht, G. P.; Wasielewski, M. R.; Forrest, S. R. Thermodynamic Efficiency Limit of Excitonic Solar Cells. *Phys. Rev. B* **2011,** *83*, 195326.
7. Koster, L. J. A.; Shaheen, S. E.; Hummelen, J. C. Pathways to a New Efficiency Regime for Organic Solar Cells. *Adv. Energy Mater.* **2012,** *2*, 1246-1253.
8. Hoppe, H.; Sariciftci, N. S. Morphology of Polymer/Fullerene Bulk Heterojunction Solar Cells. *J. Mater. Chem.* **2006,** *16*, 45-61.
9. Brabec, C. J.; Gowrisanker, S.; Halls, J. J.; Laird, D.; Jia, S.; Williams, S. P. Polymer-Fullerene Bulk-Heterojunction Solar Cells. *Adv. Mater.* **2010,** *22*, 3839-3856.

10. Thompson, B. C.; Frechet, J. M. J. Organic Photovoltaics - Polymer-Fullerene Composite Solar Cells. *Angew. Chem., Int. Ed. Engl.* **2008,** *47*, 58-77.
11. Vandewal, K.; Gadisa, A.; Oosterbaan, W. D.; Bertho, S.; Banishoeib, F.; Van Severen, I.; Lutsen, L.; Cleij, T. J.; Vanderzande, D.; Manca, J. V. The Relation between Open-Circuit Voltage and the Onset of Photocurrent Generation by Charge-Transfer Absorption in Polymer : Fullerene Bulk Heterojunction Solar Cells. *Adv. Funct. Mater.* **2008,** *18*, 2064-2070.
12. Vandewal, K.; Albrecht, S.; Hoke, E. T.; Graham, K. R.; Widmer, J.; Douglas, J. D.; Schubert, M.; Mateker, W. R.; Bloking, J. T.; Burkhard, G. F.*; et al.* Efficient Charge Generation by Relaxed Charge-Transfer States at Organic Interfaces. *Nat. Mater.* **2014,** *13*, 63-68.
13. Maurano, A.; Hamilton, R.; Shuttle, C. G.; Ballantyne, A. M.; Nelson, J.; O'Regan, B.; Zhang, W.; McCulloch, I.; Azimi, H.; Morana, M.*; et al.* Recombination Dynamics as a Key Determinant of Open Circuit Voltage in Organic Bulk Heterojunction Solar Cells: A Comparison of Four Different Donor Polymers. *Adv. Mater.* **2010,** *22*, 4987-92.
14. Rao, A.; Chow, P. C. Y.; Gelinas, S.; Schlenker, C. W.; Li, C.-Z.; Yip, H.-L.; Jen, A. K. Y.; Ginger, D. S.; Friend, R. H. The Role of Spin in the Kinetic Control of Recombination in Organic Photovoltaics. *Nature* **2013,** *500*, 435-439.
15. Schlenker, C. W.; Chen, K.-S.; Yip, H.-L.; Li, C.-Z.; Bradshaw, L. R.; Ochsenbein, S. T.; Ding, F.; Li, X. S.; Gamelin, D. R.; Jen, A. K. Y.*; et al.* Polymer Triplet Energy Levels Need Not Limit Photocurrent Collection in Organic Solar Cells. *J. Am. Chem. Soc.* **2012,** *134*, 19661-19668.
16. Vandewal, K.; Tvingstedt, K.; Gadisa, A.; Inganas, O.; Manca, J. V. On the Origin of the Open-Circuit Voltage of Polymer-Fullerene Solar Cells. *Nat. Mater.* **2009,** *8*, 904-909.
17. Vandewal, K.; Tvingstedt, K.; Gadisa, A.; Inganäs, O.; Manca, J. V. Relating the Open-Circuit Voltage to Interface Molecular Properties of Donor:Acceptor Bulk Heterojunction Solar Cells. *Phys. Rev. B* **2010,** *81*, 125204.
18. Piersimoni, F.; Chambon, S.; Vandewal, K.; Mens, R.; Boonen, T.; Gadisa, A.; Izquierdo, M.; Filippone, S.; Ruttens, B.; D'Haen, J.*; et al.* Influence of Fullerene Ordering on the Energy of the Charge-Transfer State and Open-Circuit Voltage in Polymer:Fullerene Solar Cells. *J. Phys. Chem. C* **2011,** *115*, 10873-10880.
19. Rand, B. P.; Burk, D. P.; Forrest, S. R. Offset Energies at Organic Semiconductor Heterojunctions and Their Influence on the Open-Circuit Voltage of Thin-Film Solar Cells. *Phys. Rev. B* **2007,** *75*, 115327.
20. Brenner, T. J. K.; McNeill, C. R. Spatially Resolved Spectroscopic Mapping of Photocurrent and Photoluminescence in Polymer Blend Photovoltaic Devices. *J. Phys. Chem. C* **2011,** *115*, 19364-19370.
21. Justin L. Luria, N. H., Robert Bruce, Andrew R. Jacobs, Chris Groves, John A. Marohn. Spectroscopic Imaging of Photopotentials and Photoinduced Potential Fluctuations in a Bulk Heterojunction Solar Cell Film. *ACS Nano* **2012,** *6*, 9392-9401.
22. Cox, P. A.; Waldow, D. A.; Dupper, T. J.; Jesse, S.; Ginger, D. S. Mapping Nanoscale Variations in Photochemical Damage of Polymer/Fullerene Solar Cells with Dissipation Imaging. *ACS Nano* **2013,** *7*, 10405-10413.
23. Coffey, D. C.; Ginger, D. S. Time-Resolved Electrostatic Force Microscopy of Polymer Solar Cells. *Nat. Mater.* **2006,** *5*, 735-740.
24. Giridharagopal, R.; Rayermann, G. E.; Shao, G.; Moore, D. T.; Reid, O. G.; Tillack, A. F.; Masiello, D. J.; Ginger, D. S. Submicrosecond Time Resolution Atomic Force Microscopy for Probing Nanoscale Dynamics. *Nano Lett.* **2012,** *12*, 893-898.

25. Reid, O. G.; Rayermann, G. E.; Coffey, D. C.; Ginger, D. S. Imaging Local Trap Formation in Conjugated Polymer Solar Cells: A Comparison of Time-Resolved Electrostatic Force Microscopy and Scanning Kelvin Probe Imaging†. *J. Phys. Chem. C* **2010,** *114*, 20672-20677.
26. Wong, C. Y.; Penwell, S. B.; Cotts, B. L.; Noriega, R.; Wu, H.; Ginsberg, N. S. Revealing Exciton Dynamics in a Small-Molecule Organic Semiconducting Film with Subdomain Transient Absorption Microscopy. *J. Phys. Chem. C* **2013,** *117*, 22111-22122.
27. Balke, N.; Maksymovych, P.; Jesse, S.; Kravchenko, I. I.; Li, Q.; Kalinin, S. V. Exploring Local Electrostatic Effects with Scanning Probe Microscopy: Implications for Piezoresponse Force Microscopy and Triboelectricity. *ACS Nano* **2014,** *8*, 10229-10236.
28. Bakulin, A. A.; Rao, A.; Pavelyev, V. G.; van Loosdrecht, P. H. M.; Pshenichnikov, M. S.; Niedzialek, D.; Cornil, J.; Beljonne, D.; Friend, R. H. The Role of Driving Energy and Delocalized States for Charge Separation in Organic Semiconductors. *Science* **2012,** *335*, 1340-1344.
29. Gélinas, S.; Rao, A.; Kumar, A.; Smith, S. L.; Chin, A. W.; Clark, J.; van der Poll, T. S.; Bazan, G. C.; Friend, R. H. Ultrafast Long-Range Charge Separation in Organic Semiconductor Photovoltaic Diodes. *Science* **2014,** *343*, 512-516.
30. Vandewal, K.; Goris, L.; Haeldermans, I.; Nesládek, M.; Haenen, K.; Wagner, P.; Manca, J. V. Fourier-Transform Photocurrent Spectroscopy for a Fast and Highly Sensitive Spectral Characterization of Organic and Hybrid Solar Cells. *Thin Solid Films* **2008,** *516*, 7135-7138.
31. Street, R. A.; Hawks, S. A.; Khlyabich, P. P.; Li, G.; Schwartz, B. J.; Thompson, B. C.; Yang, Y. Electronic Structure and Transition Energies in Polymer–Fullerene Bulk Heterojunctions. *J. Phys. Chem. C* **2014,** *118*, 21873-21883.
32. Coffey, D. C.; Larson, B. W.; Hains, A. W.; Whitaker, J. B.; Kopidakis, N.; Boltalina, O. V.; Strauss, S. H.; Rumbles, G. An Optimal Driving Force for Converting Excitons into Free Carriers in Excitonic Solar Cells. *J. Phys. Chem. C* **2012,** *116*, 8916-8923.
33. Martí, A.; Antolín, E.; Stanley, C. R.; Farmer, C. D.; López, N.; Díaz, P.; Cánovas, E.; Linares, P. G.; Luque, A. Production of Photocurrent Due to Intermediate-to-Conduction-Band Transitions: A Demonstration of a Key Operating Principle of the Intermediate-Band Solar Cell. *Phys. Rev. Lett.* **2006,** *97*, 247701.
34. Elborg, M.; Noda, T.; Mano, T.; Jo, M.; Sakuma, Y.; Sakoda, K.; Han, L. Voltage Dependence of Two-Step Photocurrent Generation in Quantum Dot Intermediate Band Solar Cells. *Sol. Energy Mater. Sol. Cells* **2015,** *134*, 108-113.
35. Leijtens, T.; Stranks, S. D.; Eperon, G. E.; Lindblad, R.; Johansson, E. M. J.; McPherson, I. J.; Rensmo, H.; Ball, J. M.; Lee, M. M.; Snaith, H. J. Electronic Properties of Meso-Superstructured and Planar Organometal Halide Perovskite Films: Charge Trapping, Photodoping, and Carrier Mobility. *ACS Nano* **2014,** *8*, 7147-7155.
36. Coffey, D. C.; Reid, O. G.; Rodovsky, D. B.; Bartholomew, G. P.; Ginger, D. S. Mapping Local Photocurrents in Polymer/Fullerene Solar Cells with Photoconductive Atomic Force Microscopy. *Nano Lett.* **2007,** *7*, 738-744.
37. Pingree, L. S. C.; Reid, O. G.; Ginger, D. S. Imaging the Evolution of Nanoscale Photocurrent Collection and Transport Networks During Annealing of Polythiophene/Fullerene Solar Cells. *Nano Lett.* **2009,** *9*, 2946-2952.
38. Lombardo, C. J.; Glaz, M. S.; Ooi, Z.-E.; Vanden Bout, D. A.; Dodabalapur, A. Scanning Photocurrent Microscopy of Lateral Organic Bulk Heterojunctions. *Phys. Chem. Chem. Phys.* **2012,** *14*, 13199-13203.
39. Gao, Y.; Martin, T. P.; Niles, E. T.; Wise, A. J.; Thomas, A. K.; Grey, J. K. Understanding Morphology-Dependent Polymer Aggregation Properties and Photocurrent Generation in

Polythiophene/Fullerene Solar Cells of Variable Compositions. *J. Phys. Chem. C* **2010,** *114*, 15121-15128.
40. Collins, B. A.; Li, Z.; Tumbleston, J. R.; Gann, E.; McNeill, C. R.; Ade, H. Absolute Measurement of Domain Composition and Nanoscale Size Distribution Explains Performance in Ptb7:Pc71bm Solar Cells. *Adv. Energy Mater.* **2013,** *3*, 65-74.
41. Hammond, M. R.; Kline, R. J.; Herzing, A. A.; Richter, L. J.; Germack, D. S.; Ro, H.-W.; Soles, C. L.; Fischer, D. A.; Xu, T.; Yu, L.*; et al.* Molecular Order in High-Efficiency Polymer/Fullerene Bulk Heterojunction Solar Cells. *ACS Nano* **2011,** *5*, 8248-8257.
42. Ostrowski, D. P.; Vanden Bout, D. A. Correlation of Morphology with Photocurrent Generation in a Polymer Blend Photovoltaic Device. *Small* **2014,** *10*, 1821-1829.
43. Guide, M.; Dang, X.-D.; Nguyen, T.-Q. Nanoscale Characterization of Tetrabenzoporphyrin and Fullerene-Based Solar Cells by Photoconductive Atomic Force Microscopy. *Adv. Mater. (Weinheim, Ger.)* **2011,** *23*, 2313-2319.
44. Vanecek, M.; Poruba, A. Fourier Transform Photocurrent Spectroscopy Applied to a Broad Variety of Electronically Active Thin Films (Silicon, Carbon, Organics). *Thin Solid Films* **2007,** *515*, 7499-7503.
45. Shao, G.; Rayermann, G. E.; Smith, E. M.; Ginger, D. S. Morphology-Dependent Trap Formation in Bulk Heterojunction Photodiodes. *J. Phys. Chem. B* **2013,** *117*, 4654-4660.
46. Cherniavskaya, O.; Chen, L.; Weng, V.; Yuditsky, L.; Brus, L. E. Quantitative Noncontact Electrostatic Force Imaging of Nanocrystal Polarizability. *J. Phys. Chem. B* **2003,** *107*, 1525-1531.
47. Silveira, W. R.; Marohn, J. A. Microscopic View of Charge Injection in an Organic Semiconductor. *Phys. Rev. Lett.* **2004,** *93*, 116104.
48. Kaake, L. G.; Jasieniak, J. J.; Bakus, R. C.; Welch, G. C.; Moses, D.; Bazan, G. C.; Heeger, A. J. Photoinduced Charge Generation in a Molecular Bulk Heterojunction Material. *J. Am. Chem. Soc.* **2012,** *134*, 19828-19838.
49. Martens, T.; D'Haen, J.; Munters, T.; Beelen, Z.; Goris, L.; Manca, J.; D'Olieslaeger, M.; Vanderzande, D.; De Schepper, L.; Andriessen, R. Disclosure of the Nanostructure of Mdmo-Ppv:Pcbm Bulk Hetero-Junction Organic Solar Cells by a Combination of Spm and Tem. *Synth. Met.* **2003,** *138*, 243-247.
50. Krauss, T. D.; Brus, L. E. Charge, Polarizability, and Photoionization of Single Semiconductor Nanocrystals. *Phys. Rev. Lett.* **1999,** *83*, 4840-4843.
51. Shaheen, S. E.; Brabec, C. J.; Sariciftci, N. S.; Padinger, F.; Fromherz, T.; Hummelen, J. C. 2.5% Efficient Organic Plastic Solar Cells. *Appl. Phys. Lett.* **2001,** *78*, 841-843.
52. Hoppe, H.; Niggemann, M.; Winder, C.; Kraut, J.; Hiesgen, R.; Hinsch, A.; Meissner, D.; Sariciftci, N. S. Nanoscale Morphology of Conjugated Polymer/Fullerene-Based Bulk-Heterojunction Solar Cells. *Adv. Funct. Mater.* **2004,** *14*, 1005-1011.
53. Wise, A. J.; Precit, M. R.; Papp, A. M.; Grey, J. K. Effect of Fullerene Intercalation on the Conformation and Packing of Poly-(2-Methoxy-5-(3′-7′-Dimethyloctyloxy)-1,4-Phenylenevinylene). *ACS Appl. Mater. Interfaces* **2011,** *3*, 3011-3019.
54. Park, L. Y.; Munro, A. M.; Ginger, D. S. Controlling Film Morphology in Conjugated Polymer:Fullerene Blends with Surface Patterning. *J. Am. Chem. Soc.* **2008,** *130*, 15916-15926.

Chapter 3. Mapping Nanoscale variations in Photochemical Damage of Polymer/Fullerene Solar Cells with Dissipation Imaging[2]

3.1 INTRODUCTION

With champion-cell power conversion efficiencies now crossing the long-sought 10% threshold, organic photovoltaics (OPVs) are gaining more attention as a cost-competitive, renewable energy source.[1, 2] For nearly a decade, the major focus of OPV research has been on increasing device efficiencies.[3-5] During this time, comparatively less attention has been given to the stability of these devices.[6-9] While accelerated lifetime testing of encapsulated OPV devices have already been reported to exceed seven years,[10] the lifetimes of OPVs are still far shorter than the multi-decade lifetimes often attributed to traditional inorganic photovoltaics.[6] It thus remains an open challenge to better understand the pathways leading to the degradation of OPVs in order to design longer lasting materials and device structures.

To date, lifetime studies have yielded important insights into the aging mechanisms of current generations of OPVs.[11-19] For instance, Peters *et al.* tracked power conversion efficiencies of P3HT- and PCDTBT-based solar cells over thousands of hours to understand the "burn-in loss" dominating the degradation timescale.[10] Madsen *et al*. used highly concentrated light of up to 150 suns to accelerate degradation in P3HT films, finding degradation to scale linearly with light intensity.[17] Alem *et al.* have employed conventional techniques such as NMR, XPS, and UV-visible spectroscopy to study oxygen bond formation in the degradation of polymers containing a central benzo[1,2-b:4,5-b′]dithiophene unit.[18] These studies and others have provided valuable evidence for device degradation mechanisms including the effects of contacts, thermal morphology coarsening, impurities, the role of oxygen and water exposure,[19] and photo-oxidation of active layer materials.[6] While the use of inverted structures to eliminate reactive metal interfaces,[20-23] crosslinking to reduce morphological coarsening,[24, 25] and advances in encapsulation have led to significant increases in practical lifetimes,[26, 27] the photochemical

[2] This chapter adapted from Phillip A. Cox, Dean A. Waldow, Torin J. Dupper, Stephen Jesse, David S. Ginger, *ACS Nano*, **2013**, 7 (11), pp 10405 – 10413, DOI: 10.1021/nn404920t.

stability of the active layers remains an important factor in the long-term lifetime limits that can be achieved.

While most OPV degradation studies so far have relied primarily on measuring bulk device properties as a function of light and oxygen exposure, there is reason to believe that active layer morphology might also play a role in determining photochemical stability. For instance, photocurrent collection maps[28-35] and device models that incorporate energetic disorder[36, 37] indicate that even in fairly efficient devices, the current can be collected predominantly along pathways representing a small fraction of the total film volume. An alternative hypothesis suggests that more ordered regions of a film should exhibit a lower density of tail states, leading to a higher local stability in these regions.[38]

To test such hypotheses, it is important to have tools capable of measuring local variations in electronic properties of OPV films. Scanning kelvin probe microscopy (SKPM) has also been applied to study photodegradation in model OPV materials,[39, 40] though generally without resolving variations due to local composition. In recent studies, our group has used time-resolved electrostatic force microscopy (trEFM)[41] to study photochemical degradation[40, 42] in model polymer/polymer donor/acceptor blends and found that device degradation is not uniform across the active area, but can depend on active layer morphology. While trEFM is well-suited to degradation studies, its time resolution is insufficient for the study of high-efficiency OPVs under typical solar illumination intensities. We have also developed a next-generation method – fast, free trEFM (FF-trEFM)[43] – but this method is not yet commercially available.

Motivated by the work of Denk and Pohl,[44] who demonstrated that the dissipation of an oscillating atomic force microscope (AFM) cantilever could be used to measure doping induced variations in sample conductivity in inorganic semiconductors, our goal herein is to show that dissipation mapping using frequency-modulated electrostatic force microscopy (FM-EFM) can provide a sensitive, non-contact probe of photochemically induced changes in the electronic properties of bulk heterojunction organic photovoltaics. In FM-EFM, as implemented on our system (Asylum MFP-3D), the cantilever is lifted to a particular height above the sample (typically ~10 nm) and kept at constant phase relative to the drive by modulating the frequency of the shake piezo. A positive DC bias is applied to the cantilever while the active layer of the sample is

photoexcited. The electrostatic interactions between the tip and the sample lead to a force gradient which changes the cantilever resonance frequency and can be used to image variations in surface potential and capacitive gradient.[45] In addition, *via* long-range Coulomb interactions, the cantilever can lose energy to the motion of charges in the sample[44, 46] resulting in a reduction in cantilever amplitude – even while the frequency feedback is adjusted to keep the cantilever on resonance.

Here, using model blends of PTB7:$PC_{71}BM$,[47] we show that maps of cantilever dissipation measured with FM-EFM are sensitive to photochemical damage in organic semiconductors, and that these maps are dependent on the chosen cantilever resonance frequency. Additionally, we compare dissipation maps between PTB7:$PC_{71}BM$ films with different processing parameters, and provide a link between morphology, bulk device performance, and aging behavior in this system.

3.2 RESULTS AND DISCUSSION

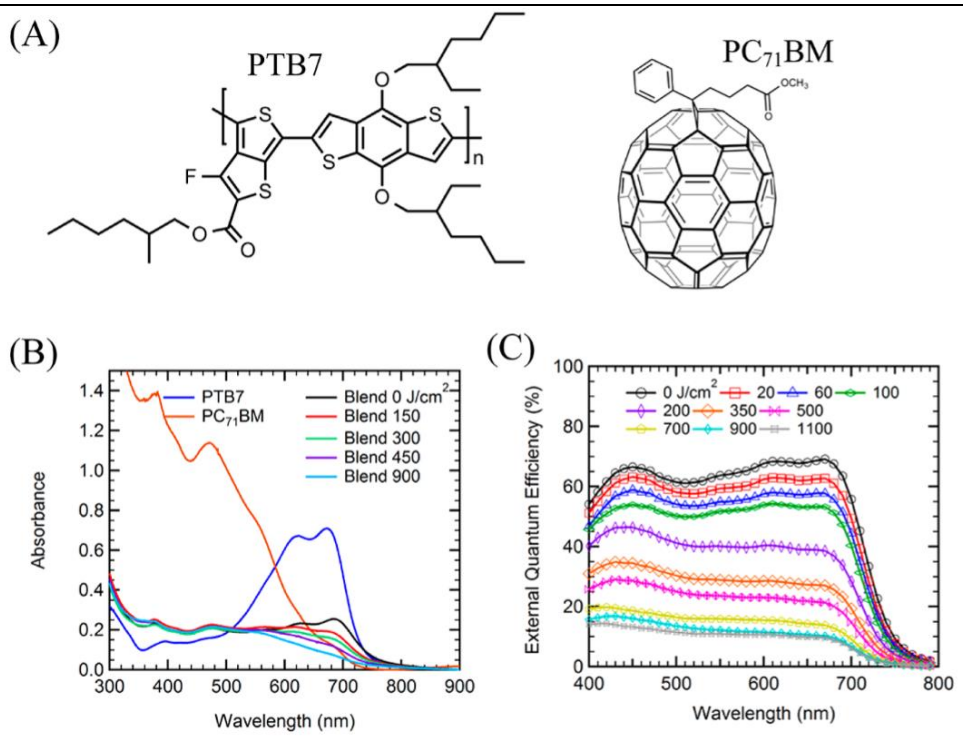

Figure 3.1 (A) Chemical structures of polymer PTB7 and fullerene $PC_{71}BM$. (B) UV-Vis spectra of neat PTB7 polymer and $PC_{71}BM$, as well as the blend film as a function of photon dose. (C) External quantum efficiencies of devices photo-oxidized over photon doses ranging from 0 to 1100 J/cm^2 as indicated in the legend.

Figure 3.1 shows the chemical structures, UV-Vis absorption spectra, and photovoltaic device properties for the PTB7:$PC_{71}BM$ blend devices we used in this study. PTB7 absorbs strongly between 600 - 700 nm, while the fullerene absorption contributes more at shorter wavelengths (300 – 600 nm). We photo-oxidized the blend films using a 660 nm LED (LEDEngin LZ1-10R200) to preferentially excite the polymer material during degradation. Figure 3.1B shows UV-Vis spectra collected after subjecting the blend films to a range of exposed photon doses from 150 J/cm^2 to 900 J/cm^2. Over this dose range, the fullerene contribution to the film absorbance at shorter wavelengths (300 – 600 nm) remains constant throughout the degradation process. However, the PTB7-dominated absorption at longer wavelengths (600 – 700 nm) diminishes gradually as a function of photon dose, eventually decreasing to ~40% of its original absorbance

value after an exposed photon dose of 900 J/cm^2, consistent with photobleaching of the PTB7 chromophore upon exposure to 660 nm light in air. Photobleaching leads to a decrease in light absorption and concomitant reduction in exciton generation that can account for some of the decrease in external quantum efficiency (EQE) we observe in the same spectral region shown in Figure 3.1B. However, the observed reduction in photocurrent *cannot* result solely from decreased light absorption: not only is the decrease in EQE much larger than the decrease in absorption at the PTB7 absorption maximum (see Appendix Figure B.1), but we observe a reduction in EQE at all wavelengths despite the lack of change in the absorption of the film in the shorter wavelength region (~300 – 600 nm). This behavior would be consistent with decreases in EQE arising from chemical degradation of the film that results in increasing recombination loss (poorer carrier collection), as well as a decrease in light absorption near the polymer peak.

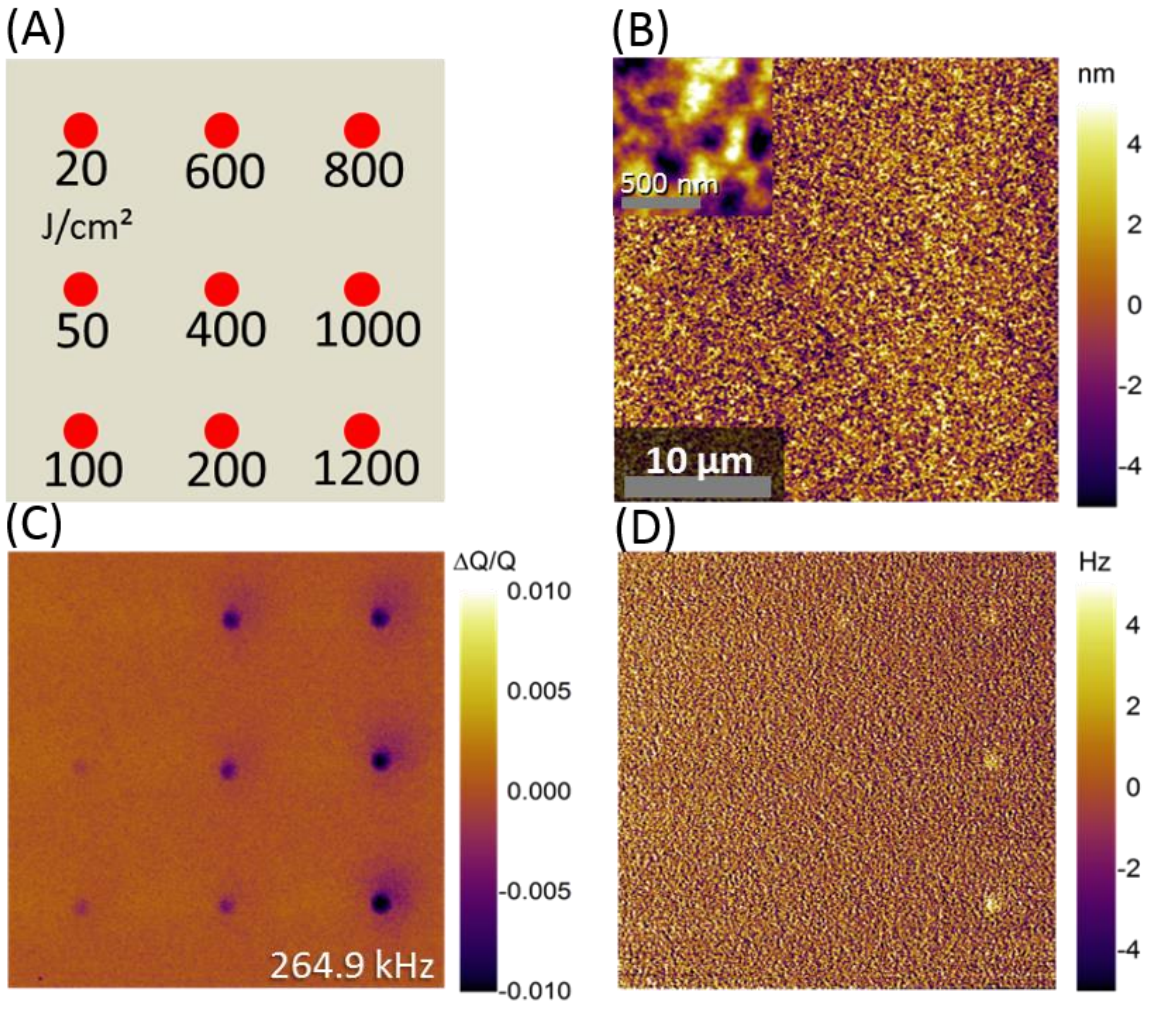

Figure 3.2 (A) Schematic of the *in situ* photon doses delivered to the sample with a 632.8 nm HeNe laser. (B) The topography (inset 1x1 µm with 500 nm scale bar), (C) ΔQ/Q, and (D) frequency shift measured while imaging a 3% DIO PTB7:$PC_{71}BM$ film photo-oxidized according to the schematic in (A) and imaged with a cantilever driven at 264.9 kHz under 5050 W/m^2 of cw 660 nm light. The scale bar is 10 µm with an overall image length and height of 30 µm.

In order to explore how photo-oxidation leads to local changes in device performance, we first photo-oxidized a film *in situ* using the focused spot (~ 1 µm in diameter) from a HeNe laser (intensity 6600 W/m^2) in air. We then purged the sample with dry nitrogen and imaged the same region of the film using FM-EFM under cw illumination, recording topography during the first pass, then cantilever frequency shift (Δω) and cantilever amplitude (A) during a second pass using a cantilever lift height of 10 nm to retrace the topography at a fixed distance.

Figure 3.2 shows typical data for a 3% DIO PTB7:$PC_{71}BM$ film imaged with FM-EFM. Figure 3.2A shows a plot of the photon doses that we used at each point, consisting of areas roughly 10 microns apart that were sequentially subjected to increasing photon doses (~20 – 1200 J/cm^2) in the presence of air. The topography of the film, shown in Figure 3.2B, appears unchanged by photo-oxidation at these doses. We plot the changes in cantilever dissipation at each position as change in cantilever quality factor (ΔQ) divided by the quality factor (Q). We calculate ΔQ/Q directly from ΔA/A (see supporting information). In contrast, to the topography, the ΔQ/Q image in Figure 3.2C shows clear contrast between the pristine and damaged regions of the film. Figure 3.2 shows that cantilever Q is very sensitive to local photodegradation: we measure an approximately 1% difference in Q between the fresh and most-degraded areas. In comparison, the relative cantilever frequency exhibits a change of only a few Hz, or about 0.0015%. In general, Q decreases over the degraded areas of the film, though this effect is frequency dependent (see below). While we have so far assumed these changes in Q result primarily from damage to the active layer, we estimate that even under photoexcitation conditions (carrier densities of ~10^{17}/cm^3) the probe depth of the cantilever would extend through the active layer film. We thus cannot rule out degradation in PEDOT:PSS as contributing to the observed changes in Q. However, as discussed below, the susceptibility of the film to photodamage is sensitive to the use of a solvent additive in the active layer, suggesting that changes in the active layer are the dominant effect.

Cantilever power dissipation is a well-studied phenomenon,[44, 48-54] but to our knowledge has not previously been applied to organic photovoltaics. The quality factor, Q, of a cantilever is inversely proportional to local power dissipation for frequency-modulated techniques[50, 55]:

$$P_{tip} = \frac{1}{2} k A^2 \omega_0 \left[\frac{1}{Q_0} - \frac{1}{Q}\right] \tag{3.1}$$

In Equation 1, k and A are the cantilever spring constant and tip amplitude, ω_0 and Q_0 are the resonance frequency and quality factor measured far from the sample surface, and Q is the quality factor close to the surface. The quality factor of the cantilever is proportional to the tip amplitude:

$$Q = \frac{A}{A_d} \tag{3.2}$$

This relationship is valid assuming (1) the tip amplitude is measured at the maximum height of the resonance curve, and (2) the cantilever motion is well described by a simple linear harmonic oscillator. We chose feedback settings to maintain condition (1), and verified that condition (2) held for our samples by obtaining Band Excitation[55, 56] images conducted at Oak Ridge (Appendix Figure B.2).

Under these conditions we can interpret the ΔQ/Q images presented here as maps of cantilever power dissipation in the sample, mediated by long range electrostatic interactions. The negative ΔQ/Q values we observe in Figure 3.2C are thus consistent with increased electrostatic damping of the cantilever motion over the photo-oxidized regions of the sample. We attribute this increased power dissipation to increased resistive losses associated with charge motion at frequencies near the cantilever resonance frequency, in response to the oscillating electric field of the cantilever.

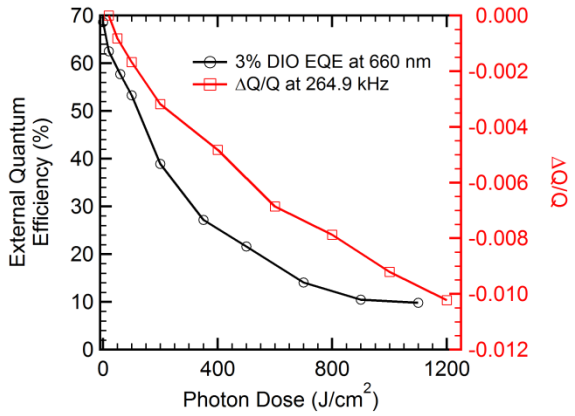

Figure 3.3 External quantum efficiencies for PTB7:$PC_{71}BM$ devices photo-oxidized in bulk and FM-EFM ΔQ/Q for a film degraded *in situ* as a function of photon dose.

By creating a grid of increasing photon doses such as that shown in Figure 3.2C, we are able to observe how the cantilever quality factor evolves over the entire lifetime of the device in a single image. Figure 3.3 compares the locally measured change in cantilever Q to the change in external quantum efficiency of a bulk device exposed to the same photon dose. We highlight that

ΔQ/Q correlates with EQE during the functional lifetime of the device (see supporting information). The correlation between these two properties suggests to us that measuring cantilever Q can be an effective method for tracking nanoscale variations in device performance. This result is particularly valuable because dissipation imaging is readily implemented on commercial instruments without any modification aside from an illumination source. Other methods for measuring local Q, such as band excitation,[55, 56] or acquiring resonance curves *via* point-by-point frequency sweeps, should allow users with access to a wide range of AFM hardware to probe spatial variation in photo-oxidation in OPV materials by measuring changes in local dissipation. While pcAFM[28-35] can be used to map local changes in photocurrent, pcAFM is a contact mode technique that is poorly suited to *repeated* imaging of soft polymer samples as is needed during degradation studies. Additionally, Q-imaging is more sensitive to changes in performance than conventional techniques, such as SKPM (Appendix Figure B.3),[40] which allows us to conduct studies on devices during the initial stages of degradation, before significant changes to surface photovoltage are detectable.

Denk and Pohl have suggested that dissipation imaging is measuring the loss term of the sample dielectric function.[44] This logical proposal would suggest that the choice of cantilever frequency should thus affect the results of a dissipation image. To test this hypothesis, we repeated the FM-EFM experiment depicted in Figure 3.2 on the same sample using three different cantilevers at five different resonance frequencies (for some cantilevers we excited both fundamental and higher harmonics).

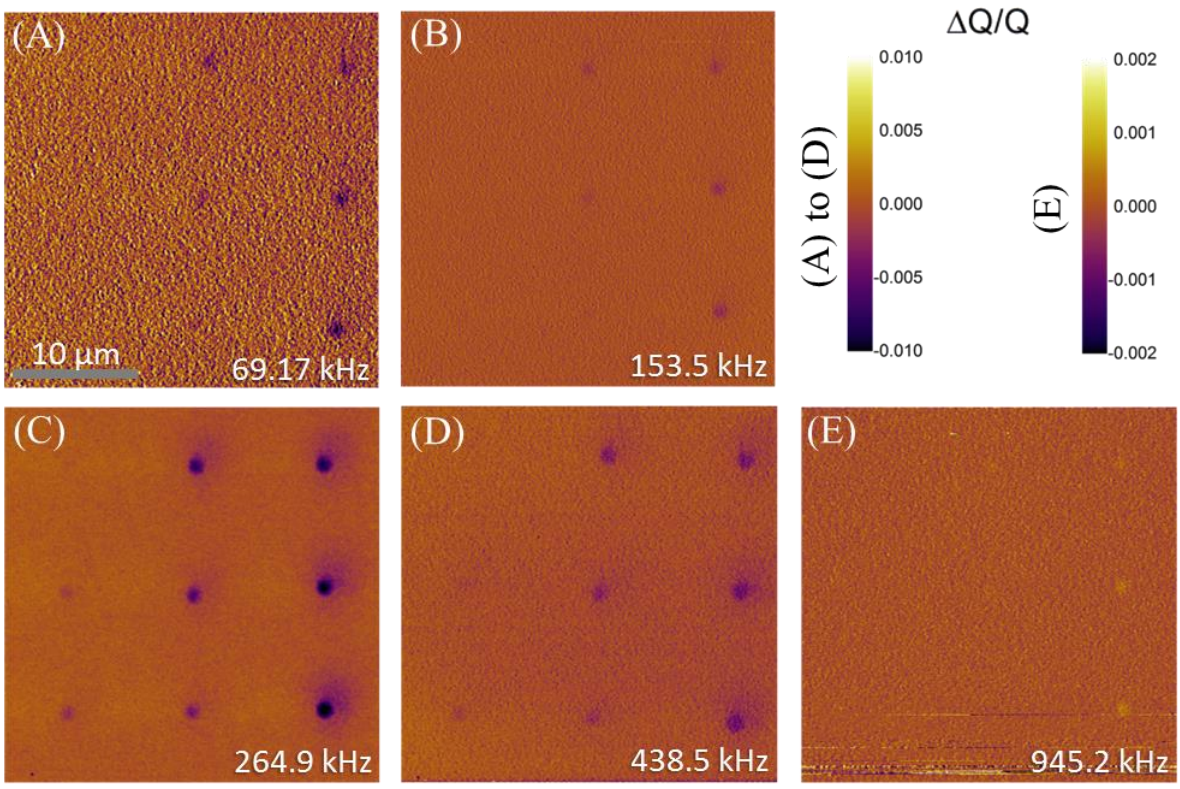

Figure 3.4 ΔQ/Q images for (A) 69.17 kHz, (B) 153.5 kHz, (C) 264.9 kHz, (D) 438.5 kHz, (E) 945.2 kHz cantilevers.

Figure 3.4 shows images of the same 30 micron area of photo-oxidized spots taken at five different cantilever resonance frequencies (69.17, 153.5, 264.9, 438.5, and 945.2 kHz), showing that both the magnitude and sign of the local power dissipation are sensitive functions of the cantilever resonance frequency. Of the frequencies measured, the maximum change in Q occurred with the 264.9 kHz cantilever. Changes in Q were significantly smaller at 153.5 kHz, but then increased again at the lowest point of 69.17 kHz. Above 264.9 kHz, the magnitude of the Q changes diminished until at 945.2 kHz Q actually changed sign to show less dissipation in the photo-oxidized areas. In all cases up to a dose of 1200 J/cm^2, the greatest ΔQ/Q always occurs over the most damaged area (we note that at very high levels of photo-oxidation, beyond those likely to be relevant for device operation, ΔQ/Q eventually begins to change slope, and even sign, as a function of dosage).

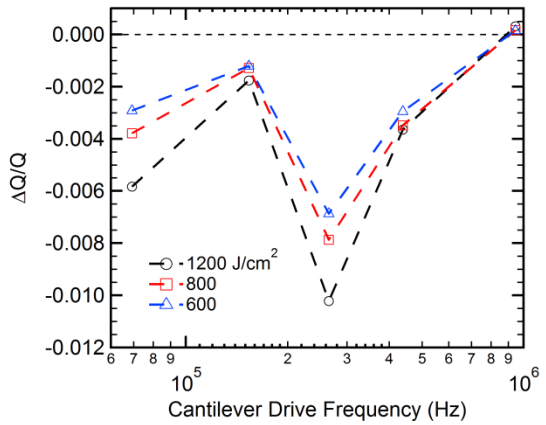

Figure 3.5 The relationship between ΔQ/Q and the log of cantilever drive frequency at 1200, 800, and 600 J/cm^2 photon doses.

Figure 3.5 plots ΔQ/Q as a function of cantilever frequency for three representative photon doses. If FM-EFM probes energy loss processes in the film, then a plot of cantilever power dissipation versus frequency should resemble the results of impedance spectroscopy measurements of the imaginary component of the relative permittivity. We note however that while the data in Fig. 3.5 would appear to reflect qualitatively the frequency dependence of the loss term of the local dielectric constant, making such a correlation quantitative would require accounting for the fact that in changing the frequency of our cantilevers, we also changed the cantilever force constants and free Q values (see Appendix Table B.1). Within the limited range of frequencies accessible using our current approach, there exists a qualitative similarity between the data in Figure 3.5 and that published previously by Armbruster and co-workers[57, 58] who showed that the imaginary part of the relative permittivity in P3HT:PCBM devices reaches a local maximum in the 10^5 Hz region, a minimum between 10^3 and 10^4 Hz, and then steadily rises as frequency approaches zero. In our PTB7:$PC_{71}BM$ films we seem to observe a minimum at a higher frequency (around 150 kHz), which could be the result of the differing device mobilities, carrier and trap densities in PTB7 vs. P3HT films, as well as the absence of the evaporated top metal contacts in our samples.

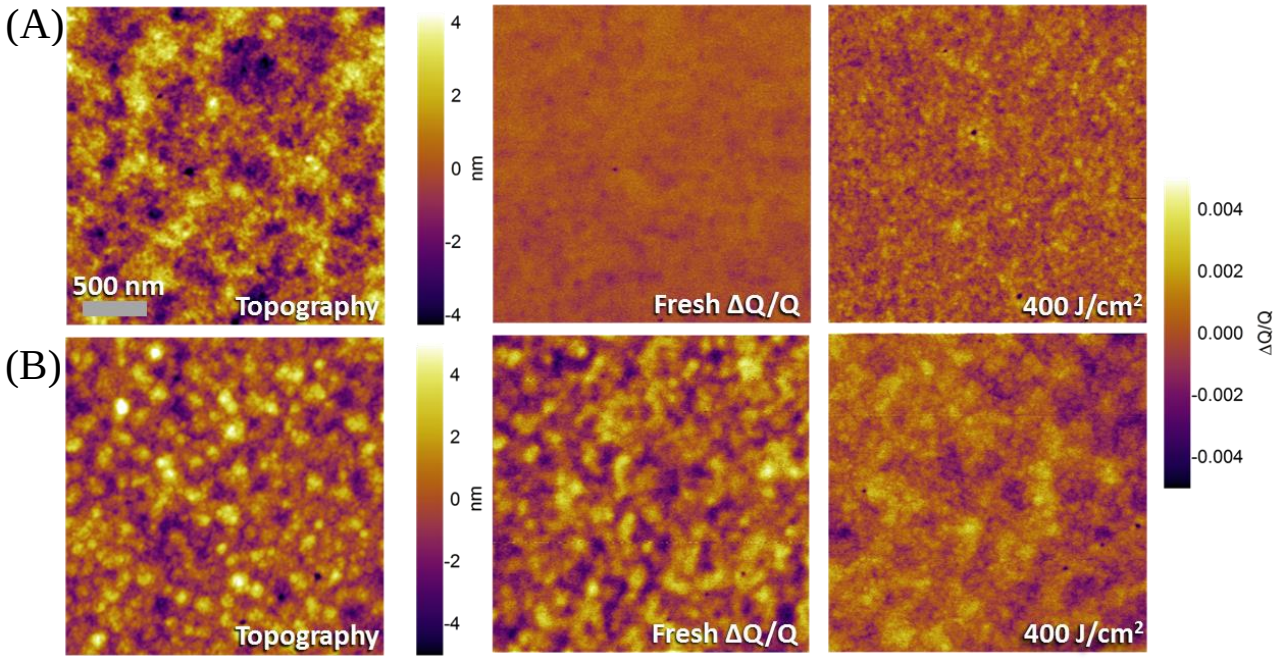

Figure 3.6 Topography and ΔQ/Q images for PTB7:$PC_{71}BM$ films processed with (A) 3% and (B) 0% solvent additive 1,8-diiodooctane. Both films were photo-oxidized with a 660 nm LED over a 2120 μm^2 area to an exposed photon dose of 400 J/cm^2. ΔQ/Q images at additional photon doses can be found in supporting information Figure B.5 and Figure B.6.

Finally, given that power dissipation appears to be a powerful way to image variations in photo-oxidative damage to films over time, we applied it to compare the effect of additive processing on the evolution of PTB7:$PC_{71}BM$ blends processed with and without the solvent additive 1,8-diiodooctane (DIO). DIO is a commonly used solvent additive that has previously been shown to improve morphology and performance (mostly by an increase in fill factor for PTB7:$PC_{71}BM$ devices[47]) of a number of polymer/fullerene bulk heterojunction solar cells.[59] However, how (and if) these changes in morphology are reflected in device aging has not been studied.

We used the same 660 nm excitation LED (operated at a higher intensity of 7500 W/m^2 to accelerate degradation) to degrade large (~2120 μm²) areas of the device, thereby achieving uniform doses over our imaging fields. As before, we conducted imaging after a thorough (>20 min.) purge with dry nitrogen so that damage would not continue during imaging. Figure 3.6 shows

topography and ΔQ/Q images of PTB7:$PC_{71}BM$ films processed (A) with and (B) without DIO before and after photo-oxidizing to a photon dose of 400 J/cm^2 (see Appendix Figure B.5 and Figure B.6 for ΔQ/Q images taken at photon doses up to 3000 J/cm^2). The ΔQ/Q image of the undamaged 3% DIO film is relatively uniform, indicating only minor detectable variations in carrier density/trap density/mobility on the ~10 nm and larger length scale in pristine devices processed with DIO. In contrast, Figure 3.6B shows the ΔQ/Q image for a fresh 0% DIO device, where we observe a clear variation in cantilever Q on the same length scale as the obvious variation in surface topography, consistent with compositionally-induced variations in electrical dissipation in these less-efficient blends. These local results are in line with the differing device fill factors which indicate that the series resistance/recombination loss is higher in films processed without DIO, as has previously been discussed.[47]

Interestingly, the use of DIO also affects the way in which the film *degrades*. After a dose of 400 J/cm^2 (which corresponds to an about 50% reduction in device performance) the 3% DIO film shows small scale variations in dissipation on ~ 40 nm length scales which were nearly invisible prior to photodegradation. On the other hand, the 0% DIO film shows faster degradation, with an overall decrease in the distribution of Q as the areas that started off as low-dissipation are photochemically damaged to a greater extent than the areas that began as lower-dissipation. Qualitatively then, the two new films exhibit clear variations in the evolution of the *distribution* of ΔQ/Q values recorded in each film as the device is further photo-oxidized (see Appendix Figure B.7). In the case of the 3% DIO film, the *distribution* of ΔQ/Q is maximized at the same photon dose where the largest shift in cantilever Q was observed in Figure 3.2C and then tapers off as photon dose approaches 3000 J/cm^2. For 0% DIO films, however, distribution of Q values simply decreases monotonically as a function of photon dose. We believe this difference is due to the decreased stability we see in 0% DIO devices (see Appendix Figures B.8 and B.9). A photon dose of 400 J/cm^2 to a 0% DIO device reduces performance by ~75%, but only ~50% in 3% DIO devices.

3.3 Conclusions

We have used frequency-modulated electrostatic force microscopy to measure changes in cantilever quality factor, or Q, as a function of photochemical damage in model PTB7:$PC_{71}BM$

solar cells processed with and without the solvent additive DIO. Our micron-spot photo-oxidations show that cantilever power dissipation is initially proportional to photon dose and as a result the quality factor of the cantilever declines as a function of damage over the functioning lifetime of the device. By making a direct comparison between our *in situ* dissipation measurements and device performance measurements, we were able to show that local changes in cantilever Q correlate well with measured external quantum efficiency changes of PTB7:$PC_{71}BM$ devices. Finally, we compared dissipation maps of PTB7:$PC_{71}BM$ films cast with and without the popular solvent additive DIO. Our results suggest that the morphology achieved when PTB7:$PC_{71}BM$ is processed with DIO leads to more uniform device degradation *via* elimination of hot-spots and bottlenecks throughout the film – consistent with the increased performance of those materials, and consistent with the better lifetimes of DIO-processed devices. We expect dissipation imaging by FM-EFM and Band Excitation can play an important role in the future design of efficient and stable organic photovoltaics through its ability to map local variations in charge transport, and possibly, to extract information reminiscent of that obtainable with frequency dependent local impedance spectroscopy.[60]

3.4 METHODS

3.4.1 *Device Preparation*

PTB7:$PC_{71}BM$ devices were made from separate solutions of 25 mg/mL PTB7 (poly[[4,8-bis[(2-ethylhexyl)oxy]benzo[1,2-b:4,5-b']dithiophene-2,6-diyl][3-fluoro-2-[(2-ethylhexyl)carbonyl]thieno[3,4-b]thiophenediyl]]) (1-Material) and $PC_{71}BM$ (3'H-cyclopropa[8,25][5,6]fullerene-C71-D5h(6)-3'-butanoicacid, 3'-phenyl-, methyl ester) (nano-c) dissolved in dichlorobenzene. After stirring and heating overnight at 60 °C, the solutions were transferred in 1:1.5 proportions by volume PTB7 to $PC_{71}BM$, where the solvent additive 1,8-diiodooctane was added at 3% by volume just prior to spincoating. The resultant solution was spin-coated to a final thickness of about 100 nm under nitrogen onto an ITO substrate with a 30 nm layer of PEDOT:PSS (Clevios™ P VP AI 4083, H. C. Stark. Chemicals). Films were dried overnight in vacuum. For bulk device performance measurements, aluminum contacts were evaporated to a final thickness of 80 nm. Aluminum contacts were evaporated after the degradation process. Bulk devices were degraded under ambient room conditions on a home-made photo-

oxidation setup using a 5 W 660 nm LED (LEDEngin LZ1-00R200) with an intensity of ~380 W/m^2. The intensity of the LED was measured with a calibrated Si-photodiode (OSI Optoelectronics) and Sourcemeter (Keithley 2400).

3.4.2 *Device Testing*

External quantum efficiencies were measured with a monochromated 450 W xenon lamp (Oriel) and Sourcemeter (Keithley 2400) and calculated using a calibrated Si-photodiode (OSI-optoelectronics). A device mask was used to cover the same area over each device and the photodiode. UV-Visible spectra (Agilent 8453) were collected under ambient conditions with either neat PTB7 (25 mg/mL), neat $PC_{71}BM$ (25mg/mL), or PTB7:$PC_{71}BM$ blend films spincoated directly onto glass substrates (no ITO or PEDOT:PSS).

3.4.3 *Atomic Force Microscopy*

AFM measurements were carried out on an Asylum Research MFP-3D BIO atomic force microscope seated on an inverted Nikon Eclipse Ti microscope and Table Stable vibration isolation stage. Silicon cantilevers (BudgetSensor) with conductive Cr/Pt coating (Multi75-G, Tap190-G, and Tap300-G) of three different resonance frequencies (69.17, 153.5, 264.9 kHz) were used. The 69 and 153 kHz cantilevers were operated in the second mode of the cantilever resonance to obtain the images at 438.5 and 945.2 kHz, respectively. All samples were housed in a flow-cell enclosure to control exposure to air or nitrogen. *In situ* photo-oxidations of ca. 1 micron spot size were performed with a 5 mW HeNe 632.8 nm laser (Research Electro-Optics), while photo-oxidations of ca. 2120 μm^2 were performed with a 660 nm LED (LEDEngin LZ10R200). Samples were purged in air for thirty minutes prior to laser exposure, and then purged in nitrogen for 30 minutes before imaging. During imaging, the sample was under constant illumination to generate charge carriers at 5050 W/m^2 using a 660 nm LED (LEDEngin LZ4-00R200). Both the laser and LED intensities were measured in the same manner as the bulk photo-oxidation LED. FM-EFM images were taken with a lift height of 10 nm and tip bias of +10 volts. The drive amplitude of the shake piezo during the EFM pass was set to half of the topography pass amplitude. During the EFM pass, the cantilever phase was held at 90° by modulating the drive frequency of the shake piezo. $\Delta Q/Q$ images are flattened to set the fresh areas of the film as a zero-point to demonstrate the difference

in amplitude between damaged and undamaged areas. The ΔQ/Q value at each photon dose is determined by individually masking each degraded area to get amplitude versus sample distance and then extracting the mean of a Gaussian fit.

3.5 ACKNOWLEDGEMENTS

This work was initially seeded by the National Science Foundation (NSF) DMR-1005504 and completed under NSF DMR-1306079. D. Waldow acknowledges NSF for research instrumentation (MRI-0619826). Band excitation measurements were conducted at the Center for Nanophase Materials Sciences, which is sponsored at Oak Ridge National Laboratory by the Scientific User Facilities Division, Office of Basic Energy Sciences, U.S. Department of Energy.

3.6 REFERENCES

1. Jingbiyou, L. D., Ken Yoshimura, Takehito Kato, Kenichiro Ohya, Tom Moriarty, Keith Emery, Chun-Chao Chen, Jing Gao, Gang Li, Yang Yang, A Polymer Tandem Solar Cell with 10.6% Power Conversion Efficiency. *Nat. Commun.* **2013**, 1446.
2. Darling, S. B.; You, F., The Case For Organic Photovoltaics. *R. Soc. Chem. Adv.* **2013**, 3, 17633.
3. Hoppe, H.; Sariciftci, N. S., Organic Solar Cells: An Overview. *J. Mater. Res.* **2004**, 19, 1924-1945.
4. Thompson, B. C.; Frechet, J. M. J., Organic Photovoltaics - Polymer-Fullerene Composite Solar Cells. *Angew. Chem., Int. Ed. Engl.* **2008**, 47, 58-77.
5. Jorgensen, M.; Norrman, K.; Gevorgyan, S. A.; Tromholt, T.; Andreasen, B.; Krebs, F. C., Stability of Polymer Solar Cells. *Adv. Mater. (Weinheim, Ger.)* **2012**, 24, 580-612.
6. Jørgensen, M.; Norrman, K.; Krebs, F. C., Stability/Degradation of Polymer Solar Cells. *Sol. Energy Mater. Sol. Cells* **2008**, 92, 686-714.
7. Lee, J. U.; Jung, J. W.; Jo, J. W.; Jo, W. H., Degradation and Stability of Polymer-Based Solar Cells. *J. Mater. Chem.* **2012**, 22, 24265.
8. Grossiord, N.; Kroon, J. M.; Andriessen, R.; Blom, P. W. M., Degradation Mechanisms in Organic Photovoltaic Devices. *Org. Electron.* **2012**, 13, 432-456.
9. Peters, C. H.; Sachs-Quintana, I. T.; Mateker, W. R.; Heumueller, T.; Rivnay, J.; Noriega, R.; Beiley, Z. M.; Hoke, E. T.; Salleo, A.; Mcgehee, M. D., The Mechanism of Burn-In Loss in a High Efficiency Polymer Solar Cell. *Adv. Mater. (Weinheim, Ger.)* **2012**, 24, 663-+.
10. Peters, C. H.; Sachs-Quintana, I. T.; Kastrop, J. P.; Beaupré, S.; Leclerc, M.; Mcgehee, M. D., High Efficiency Polymer Solar Cells with Long Operating Lifetimes. *Adv. Energy Mater.* **2011**, 1, 491-494.
11. Khelifi, S.; Decock, K.; Lauwaert, J.; Vrielinck, H.; Spoltore, D.; Piersimoni, F.; Manca, J.; Belghachi, A.; Burgelman, M., Investigation of Defects by Admittance Spectroscopy Measurements in Poly (3-Hexylthiophene):(6,6)-Phenyl C61-Butyric Acid Methyl Ester Organic Solar Cells Degraded Under Air Exposure. *J. Appl. Phys.* **2011**, 110, 094509.

12. Singh, V.; Arora, S.; Bhatnagar, P. K.; Arora, M.; Tandon, R. P., Effects of Aging on the Mobility and Lifetime of Carriers in Organic Bulk Heterojunction Solar Cells. *J. Renewable Sustainable Energy* **2011**, 3, 063111.
13. Golovnin, I. V.; Bakulin, A. A.; Zapunidy, S. A.; Nechvolodova, E. M.; Paraschuk, D. Y., Dramatic Enhancement of Photo-Oxidation Stability of a Conjugated Polymer in Blends with Organic Acceptor. *Appl. Phys. Lett.* **2008**, 92, 243311.
14. Krebs, F. C.; Gevorgyan, S. A.; Alstrup, J., A Roll-To-Roll Process to Flexible Polymer Solar Cells: Model Studies, Manufacture and Operational Stability Studies. *J. Mater. Chem.* **2009**, 19, 5442.
15. Kawano, K.; Pacios, R.; Poplavskyy, D.; Nelson, J.; Bradley, D. D. C.; Durrant, J. R., Degradation of Organic Solar Cells Due to Air Exposure. *Sol. Energy Mater. Sol. Cells* **2006**, 90, 3520-3530.
16. Aygül, U.; Hintz, H.; Egelhaaf, H.-J.; Distler, A.; Abb, S.; Peisert, H.; Chassé, T., Energy Level Alignment of a P3HT/Fullerene Blend During the Initial Steps of Degradation. *J. Phys. Chem. C* **2013**, 117, 4992-4998.
17. Madsen, M. V.; Tromholt, T.; Norrman, K.; Krebs, F. C., Concentrated Light for Accelerated Photo Degradation of Polymer Materials. *Adv. Energy Mater.* **2013**, 3, 424-427.
18. Alem, S.; Wakim, S.; Lu, J.; Robertson, G.; Ding, J.; Tao, Y., Degradation Mechanism of Benzodithiophene-Based Conjugated Polymers when Exposed to Light in Air. *ACS Appl. Mater. Interfaces* **2012**.
19. Nikiforov, M. P.; Strzalka, J.; Darling, S. B., Delineation of the Effects of Water and Oxygen on the Degradation of Organic Photovoltaic Devices. *Sol. Energy Mater. Sol. Cells* **2013**, - 110, - 42.
20. Hau, S. K.; Yip, H. L.; Baek, N. S.; Zou, J. Y.; O'Malley, K.; Jen, A. K. Y., Air-Stable Inverted Flexible Polymer Solar Cells Using Zinc Oxide Nanoparticles as an Electron Selective Layer. *Appl. Phys. Lett.* **2008**, 92.
21. Schumann, S.; Da Campo, R.; Illy, B.; Cruickshank, A. C.; Mclachlan, M. A.; Ryan, M. P.; Riley, D. J.; Mccomb, D. W.; Jones, T. S., Inverted Organic Photovoltaic Devices with High Efficiency and Stability Based on Metal Oxide Charge Extraction Layers. *J. Mater. Chem.* **2011**, 21, 2381-2386.
22. Li, C.-Y.; Wen, T.-C.; Lee, T.-H.; Guo, T.-F.; Huang, J.-C.-A.; Lin, Y.-C.; Hsu, Y.-J., An Inverted Polymer Photovoltaic Cell with Increased Air Stability Obtained by Employing Novel Hole/Electron Collecting Layers. *J. Mater. Chem.* **2009**, 19, 1643-1647.
23. Sahin, Y.; Alem, S.; De Bettignies, R.; Nunzi, J. M., Development of Air Stable Polymer Solar Cells Using an Inverted Gold on Top Anode Structure. *Thin Solid Films* **2005**, 476, 340-343.
24. He, D.; Du, X. Y.; Zhang, W.; Xiao, Z.; Ding, L. M., Improving the Stability of P3HT/PC61BM Solar Cells by a Thermal Crosslinker. *J. Mater. Chem. A.* **2013**, 1, 4589-4594.
25. Liu, B.; Png, R. Q.; Zhao, L. H.; Chua, L. L.; Friend, R. H.; Ho, P. K. H., High Internal Quantum Efficiency in Fullerene Solar Cells Based on Crosslinked Polymer Donor Networks. *Nat. Commun.* **2012**, 3.
26. Lungenschmied, C.; Dennler, G.; Neugebauer, H.; Sariciftci, S. N.; Glatthaar, M.; Meyer, T.; Meyer, A., Flexible, Long-Lived, Large-Area, Organic Solar Cells. *Sol. Energy Mater. Sol. Cells* **2007**, 91, 379-384.
27. Krebs, F. C., Encapsulation of Polymer Photovoltaic Prototypes. *Sol. Energy Mater. Sol. Cells* **2006**, 90, 3633-3643.

28. Pingree, L. S. C.; Reid, O. G.; Ginger, D. S., Imaging the Evolution of Nanoscale Photocurrent Collection and Transport Networks During Annealing of Polythiophene/Fullerene Solar Cells. *Nano Lett.* **2009**, 9, 2946-2952.
29. Giridharagopal, R.; Ginger, D. S., Characterizing Morphology in Bulk Heterojunction Organic Photovoltaic Systems. *J. Phys. Chem. Lett.* **2010**, 1, 1160-1169.
30. Rice, A. H.; Giridharagopal, R.; Zheng, S. X.; Ohuchi, F. S.; Ginger, D. S.; Luscombe, C. K., Controlling Vertical Morphology within the Active Layer of Organic Photovoltaics Using Poly(3-Hexylthiophene) Nanowires and Phenyl-C61-Butyric Acid Methyl Ester. *ACS Nano* **2011**, 5, 3132-3140.
31. Dang, X.-D.; Mikhailovsky, A.; Nguyen, T.-Q., Measurement of Nanoscale External Quantum Efficiency of Conjugated Polymer:Fullerene Solar Cells by Photoconductive Atomic Force Microscopy. *Appl. Phys. Lett.* **2010**, 97.
32. Dang, X.-D.; Tamayo, A. B.; Seo, J.; Hoven, C. V.; Walker, B.; Nguyen, T.-Q., Nanostructure and Optoelectronic Characterization of Small Molecule Bulk Heterojunction Solar Cells by Photoconductive Atomic Force Microscopy. *Adv. Funct. Mater.* **2010**, 20, 3314-3321.
33. Coffey, D. C.; Reid, O. G.; Rodovsky, D. B.; Bartholomew, G. P.; Ginger, D. S., Mapping Local Photocurrents in Polymer/Fullerene Solar Cells with Photoconductive Atomic Force Microscopy. *Nano Lett.* **2007**, 7, 738-744.
34. Xin, H.; Reid, O. G.; Ren, G.; Kim, F. S.; Ginger, D. S.; Jenekhe, S. A., Polymer Nanowire/Fullerene Bulk Heterojunction Solar Cells: How Nanostructure Determines Photovoltaic Properties. *ACS Nano* **2010**, 4, 1861-1872.
35. Hamadani, B. H.; Gergel-Hackett, N.; Haney, P. M.; Zhitenev, N. B., Imaging of Nanoscale Charge Transport in Bulk Heterojunction Solar Cells. *J. Appl. Phys.* **2011**, 109.
36. Van Der Holst, J. J. M.; Uijttewaal, M. A.; Ramachandhran, B.; Coehoorn, R.; Bobbert, P. A.; De Wijs, G. A.; De Groot, R. A., Modeling And Analysis of the Three-Dimensional Current Density in Sandwich-Type Single-Carrier Devices of Disordered Organic Semiconductors. *Phys. Rev. B* **2009**, 79, 085203.
37. Tessler, N.; Preezant, Y.; Rappaport, N.; Roichman, Y., Charge Transport in Disordered Organic Materials and its Relevance to Thin-Film Devices: A Tutorial Review. *Adv. Mater. (Weinheim, Ger.)* **2009**, 21, 2741-2761.
38. Kumar, A.; Hong, Z.; Sista, S.; Yang, Y., The Critical Role of Processing and Morphology in Determining Degradation Rates in Polymer Solar Cells. *Adv. Energy Mater.* **2011**, 1, 124-131.
39. Sengupta, E.; Domanski, A. L.; Weber, S. A. L.; Untch, M. B.; Butt, H.-J.; Sauermann, T.; Egelhaaf, H. J.; Berger, R., Photoinduced Degradation Studies of Organic Solar Cell Materials Using Kelvin Probe Force and Conductive Scanning Force Microscopy. *J. Phys. Chem. C* **2011**, 115, 19994-20001.
40. Reid, O. G.; Rayermann, G. E.; Coffey, D. C.; Ginger, D. S., Imaging Local Trap Formation in Conjugated Polymer Solar Cells: A Comparison of Time-Resolved Electrostatic Force Microscopy and Scanning Kelvin Probe Imaging†. *J. Phys. Chem. C* **2010**, 114, 20672-20677.
41. Coffey, D. C.; Ginger, D. S., Time-Resolved Electrostatic Force Microscopy Of Polymer Solar Cells. *Nat. Mater.* **2006**, 5, 735-740.
42. Shao, G.; Rayermann, G. E.; Smith, E. M.; Ginger, D. S., Morphology-Dependent Trap Formation in Bulk Heterojunction Photodiodes. *J. Phys. Chem. B* **2013**, 117, 4654-60.

43. Giridharagopal, R.; Rayermann, G. E.; Shao, G.; Moore, D. T.; Reid, O. G.; Tillack, A. F.; Masiello, D. J.; Ginger, D. S., Submicrosecond Time Resolution Atomic Force Microscopy for Probing Nanoscale Dynamics. *Nano Lett.* **2012**, 12, 893-8.
44. Denk, W.; Pohl, D. W., Local Electrical Dissipation Imaged by Scanning Force Microscopy. *Appl. Phys. Lett.* **1991**, 59, 2171.
45. Silveira, W.; Marohn, J., Microscopic View of Charge Injection in an Organic Semiconductor. *Phys. Rev. Lett.* **2004**, 93.
46. Lekkala, S.; Hoepker, N.; Marohn, J. A.; Loring, R. F., Charge Carrier Dynamics and Interactions in Electric Force Microscopy. *J. Chem. Phys.* **2012**, 137.
47. Liang, Y.; Xu, Z.; Xia, J.; Tsai, S. T.; Wu, Y.; Li, G.; Ray, C.; Yu, L., For the Bright Future-Bulk Heterojunction Polymer Solar Cells with Power Conversion Efficiency Of 7.4%. *Adv. Mater. (Weinheim, Ger.)* **2010**, 22, E135-8.
48. Stowe, T. D.; Kenny, T. W.; Thomson, D. J.; Rugar, D., Silicon Dopant Imaging by Dissipation Force Microscopy. *Appl. Phys. Lett.* **1999**, 75, 2785.
49. B. Anczykowski, B. G., H. Fuchs, J.P. Cleveland, V.B. Elings, How to Measure Energy Dissipation in Dynamic Mode Atomic Force Microscopy. *Appl. Surf. Sci.* **1998**, 140, 376-382.
50. Cleveland, J. P.; Anczykowski, B.; Schmid, A. E.; Elings, V. B., Energy Dissipation in Tapping-Mode Atomic Force Microscopy. *Appl. Phys. Lett.* **1998**, 72, 2613.
51. Dedkov, G. V., On The Dissipation Of Mechanical Energy in a Noncontact Dynamic Mode of a Scanning Probe Microscope Under Vacuum. *Phys. Solid State* **2006**, 48, 747-752.
52. Gannepalli, A.; Yablon, D. G.; Tsou, A. H.; Proksch, R., Mapping Nanoscale Elasticity and Dissipation Using Dual Frequency Contact Resonance AFM. *Nanotechnology* **2011**, 22, 355705.
53. Kareem, A. U.; Solares, S. D., Characterization of Surface Stiffness and Probe-Sample Dissipation Using the Band Excitation Method of Atomic Force Microscopy: A Numerical Analysis. *Nanotechnology* **2012**, 23, 015706.
54. Proksch, R.; Kalinin, S. V., Energy Dissipation Measurements in Frequency-Modulated Scanning Probe Microscopy. *Nanotechnology* **2010**, 21, 455705.
55. Jesse, S.; Kalinin, S. V.; Proksch, R.; Baddorf, A. P.; Rodriguez, B. J., The Band Excitation Method in Scanning Probe Microscopy for Rapid Mapping of Energy Dissipation on the Nanoscale. *Nanotechnology* **2007**, 18, 435503.
56. Jesse, S.; Kalinin, S. V., Band Excitation in Scanning Probe Microscopy: Sines of Change. *J. Phys. D: Appl. Phys.* **2011**, 44, 464006.
57. Armbruster, O.; Lungenschmied, C.; Bauer, S., Investigation of Trap States and Mobility in Organic Semiconductor Devices by Dielectric Spectroscopy: Oxygen-Doped P3HT:PCBM Solar Cells. *Phys. Rev. B* **2012**, 86.
58. Armbruster, O.; Lungenschmied, C.; Bauer, S., Dielectric Response of Doped Organic Semiconductor Devices: P3HT:PCBM Solar Cells. *Phys. Rev. B* **2011**, 84.
59. Lou, S. J.; Szarko, J. M.; Xu, T.; Yu, L.; Marks, T. J.; Chen, L. X., Effects of Additives on the Morphology of Solution Phase Aggregates Formed by Active Layer Components of High-Efficiency Organic Solar Cells. *J. Am. Chem. Soc.* **2011**, 133, 20661-3.
60. Lee, W.; Prinz, F. B.; Chen, X.; Nonnenmann, S.; Bonnell, D. A.; O'Hayre, R. P., Nanoscale Impedance and Complex Properties in Energy-Related Systems. *MRS Bulletin* **2012**, 37, 659-667.

Chapter 4. Dissipation Imaging *via* Cantilever Ringdown for the Study of Loss Processes in Polymer/Fullerene Solar Cells[3]

4.1 INTRODUCTION

While increases in power conversion efficiency have served as the main driving force behind polymer solar cell research for over a decade, device stability remains a major research challenge impeding progress in thin film solar technology.[1, 2] Specifically, the polymer/fullerene active layer is prone to photochemical degradation in the presence of light and oxygen.[3-5] Water exposure from air is another major cause for concern especially with respect to the commonly used hole-transport layer PEDOT:PSS.[6-8] Stability issues are broader than organics, indeed, the stability of hybrid perovskites has also become an important issue.[9, 10] In nanostructured materials like OPVs, the relationship between local film structure and device performance has been studied with a broad range of instrumentation in order to better understand charge carrier generation, transport, and collection.[11-15] However, the effects of morphology on device stability have received less attention,[2] with relatively few studies directly linking local structure with device stability.[16-19]

A commonly used technique for controlling morphology, and thus efficiency, of organic photovoltaics (OPVs) is the use of solvent additives.[20] Typically, additives such as 1,8-diiodooctane (DIO) are added in small volumes prior to spincoating the polymer/fullerene solution to increase the solubility of PCBM and mitigate its propensity for forming aggregates.[11, 21] For example, use of DIO in PTB7:$PC_{71}BM$ devices can increase device efficiency from 3.9% to 7.4% due to increases in short-circuit current density (J_{SC}) and fill factor (FF) brought about by increased mixing of the polymer and fullerene.[22] A less understood effect of the morphological changes induced by DIO is a more stable, longer-lasting device.[17] Clearly, the same morphological effects that contribute to increased device performance are inextricably linked to photochemical degradation of the active layer.

[3] This chapter adapted from Phillip A. Cox, Lucas Q. Flagg, Rajiv Giridharagopal, David S. Ginger, **2016**. To be submitted to *J. Phys. Chem. C.*

The ability to probe electrical properties at the nanoscale during the photochemical evolution of the semiconductor active layer is critical to understanding the relationship between device structure and stability. While many device lifetime studies focus on bulk measurements of completed devices[16, 23-26] we have previously shown that local dissipation measurements can be used to reveal nanoscale variations in organic semiconductor materials that arise from photochemical degradation.[17] For an electronically active sample, the power dissipation of the cantilever has contributions from Coulombic drag,[27] making dissipation imaging suited for studying polymer/fullerene solar cell degradation as materials breakdown causes changes in trap state density, charge carrier mobility and charge carrier density.[28-30] We previously used frequency-modulated electrostatic force microscopy (FM-EFM), a commercially-available atomic force microscopy (AFM) technique that can create fast, qualitative dissipation maps. FM-EFM can be used to map the quality factor (Q) of an oscillating atomic force microscope cantilever indirectly by utilizing a phase-locked feedback loop to keep the cantilever at resonance. Under these conditions, cantilever Q is equal to the tip amplitude divided by the drive piezo amplitude.[31-33] However, the challenge of calibrating the amplitude of the drive piezo can make quantitative comparisons between multiple images difficult. This difficulty arises because, while the drive voltage sent to the piezo is well known, the efficiency this energy is transferred to the cantilever depends on the mechanical mounting, and can change during the course of imaging with changes in environment, temperature, or coupling between the piezo and cantilever chip. Here, we instead measure cantilever power dissipation quantitatively through the straightforward method of cantilever ringdown imaging.

We have previously shown that cantilever power dissipation is much more sensitive to changes in film properties during photo-oxidation compared to other techniques that rely on changes in capacitive force gradient and sample work function such as SKPM.[17] Furthermore, power dissipation probes processes like changes in carrier transport and trapping, which can be more informative than measuring optical density losses[15, 34] as rates of photobleaching often do not track with the device performance characteristics of photodegraded polymer/fullerene blends.[17] While other AFM methods are also capable of measuring cantilever Q, such as dual-amplitude resonance tracking (DART)[35] and band excitation (BE),[33] these methods have most often been employed in contact resonance imaging modes for more structurally stable materials.

Here we show that quantitative and non-destructive dissipation imaging can be performed by measuring the ringdown time of a conductive AFM cantilever interacting electrostatically with charge carriers in an organic semiconductor film. We compare device EQE measurements and local power dissipation measurements as a function of photo-oxidative damage for three different PTB7:$PC_{71}BM$ film morphologies and show that our local dissipation measurements correlate with device stability. Furthermore, we show how power dissipation evolves with degradation as a function of local film structure in the most phase-segregated PTB7:$PC_{71}BM$ film to show that areas comprising large fullerene aggregates more rapidly exhibit changes in dissipation due to photo-oxidative damage. Using DIO during film processing reduces fullerene aggregate size, thereby improving device stability.

4.2 Results and Discussion

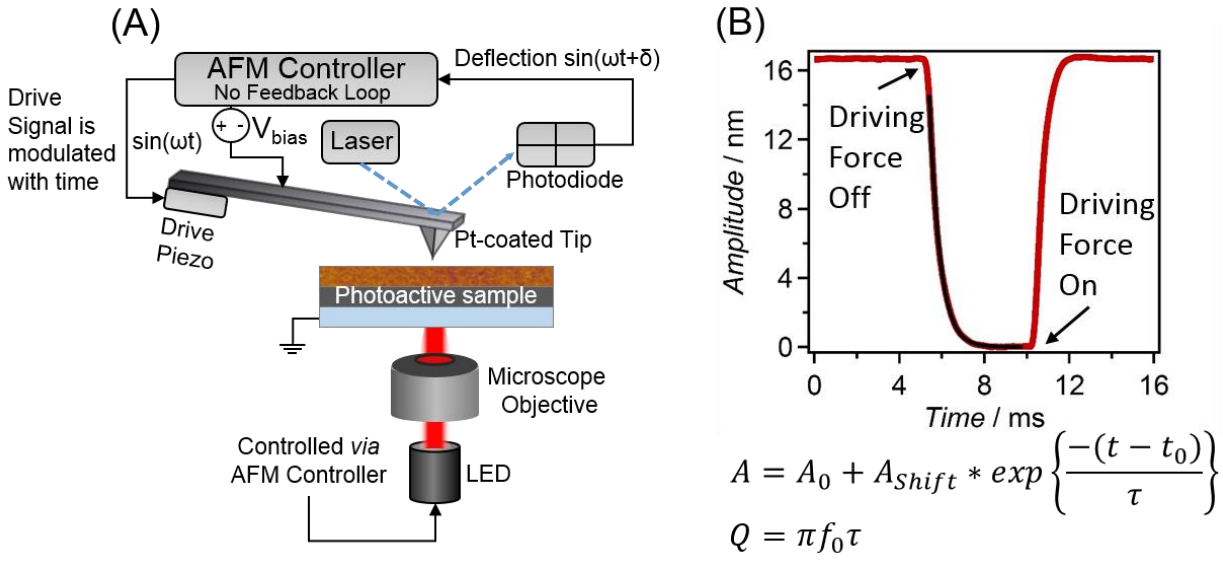

Figure 4.1 (A) Schematic of ringdown imaging experimental setup. (B) Raw data for a single image pixel showing amplitude versus time as the drive amplitude is switched off and on. The decay in amplitude is fit to the shown exponential decay function (black trace), from which tau is used to calculate cantilever Q by the equation shown, where f_0 is the resonance frequency of the cantilever.

Figure 4.1A shows our implementation of ringdown imaging. We use the two-pass method, where typical constant-amplitude AC-mode topography imaging is employed in the first pass, and the second pass follows a basic EFM setup where the tip is lifted away from the surface 10 - 50 nm and the oscillation amplitude is reduced to be sufficiently out of range of van der Waal's interactions. During the second pass the cantilever is biased at +10 V for highest signal to noise and driven at constant drive amplitude with no feedback loop, while an LED is used to create photogenerated charge carriers in the semiconductor film. During each measurement cycle, the cantilever driving force is turned off and the decaying amplitude signal is tracked in time. We allot a 5 ms pause before turning the driving force back on, which is sufficiently longer than the ringdown time of the cantilever (proportional to Q/f). While each pixel in a ringdown image requires a ~16 ms measurement cycle, we were able to image with significantly shorter acquisition times compared to BE, likely because BE acquires additional data over a wider frequency range. For example, on an Asylum Research Cypher ES AFM (Oxford Instruments), BE images at a resolution of 256 points by 256 lines with only one average per point took roughly seven times longer than the ringdown imaging method. Furthermore, the processing of our raw data is performed at the end of each image line, allowing the user to see images as they are collected, whereas data is processed in post with BE. The ~3 ms ringdown time of the cantilevers used in this study allots time for several ringdown cycles within a single 16 ms measurement cycle, allowing for an increase in averages without adding to image acquisition time. Lastly, ringdown imaging in non-contact mode is straightforward to implement by making comparatively minor changes to existing time-resolved electrostatic force microscopy code.[36]

Figure 4.1B shows the cantilever amplitude vs. time after turning off the piezo over an illuminated polymer/fullerene film. After the driving force is turned off at t = 5 ms, the cantilever amplitude decays to zero with the single-exponential form expected for a damped simple harmonic oscillator. The amplitude decay shows very good signal/noise with only one average. The cantilever amplitude recovers to its original value after the driving force is turned back on at 10 ms. We fit the amplitude decay vs. time to an exponential decay function, where τ is the fit lifetime that we use to calculate cantilever Q via:[37]

$$Q = \pi f_0 \tau \tag{4.1}$$

where f_0 is the resonance frequency of the cantilever in Hz. Q can further be used to calculate cantilever power dissipation:[22]

$$P_{tip} = \frac{1}{2} kA^2 \omega_0 \left[\frac{1}{Q_0} - \frac{1}{Q}\right] \tag{4.2}$$

where k is spring constant, A is the amplitude of the cantilever prior to turning the cantilever drive off, and ω_0 is the resonance frequency of the cantilever far from the sample surface. Because there is no feedback loop employed to keep the cantilever at resonance, the amplitude, A, of the cantilever prior to turning the driving force off shifts with changes in the cantilever Q and with the resonance frequency that arise due to local film structure, and as a result shows structure similar to the frequency shift images measured in FM-EFM when a phase-locked loop is used to hold the cantilever at resonance (comparisons shown in Appendix Figure C.1).

We are concerned specifically with changes in cantilever power dissipation that arise from photogenerated charge carriers. Therefore, we consider the change in the total dissipation that arises when the sample is illuminated by measuring Q in the light and dark:

$$P_{tip} = \frac{1}{2} kA^2 f_0 \left[\frac{1}{Q_{surface}} - \frac{1}{Q_{+10V,light}}\right] \tag{4.3}$$

where $Q_{surface}$ is measured in the dark with no electrical bias, and $Q_{+10V,light}$ is measured when the biased cantilever interacts with photogenerated carriers in the film. By calculating P_{tip} between $Q_{surface}$ and $Q_{+10V,light}$, we do not concern ourselves with mechanical energy loss due to being in close proximity of a material or the presence of dopants in the film, and instead report only the additional energy lost from the cantilever as a result of electrostatic interactions between tip and photogenerated charge carriers.

To demonstrate ringdown imaging, we chose the model polymer/fullerene OPV blend PTB7:$PC_{71}BM$ due to the ability to easily change the final film morphology using different

solvents, solvent additives, or polymer:fullerene ratio. PTB7 once held the record efficiency for single junction OPVs,[38] and has since become the focal point of a significant amount of recent OPV research.[39] Recently, Collins *et al.* used resonant X-ray scattering to measure and relate the domain composition to local device performance of PTB7:$PC_{71}BM$ devices processed with and without DIO.[11] In both cases, fullerene aggregates are dispersed in a largely amorphous mixed matrix of both polymer and fullerene. Increased performance in the DIO films is attained through a reduction of fullerene aggregate size, leading to increased exciton dissociation yield due to greater polymer access to pure fullerene aggregates. Building on these results, we prepared films with three very different PTB7:$PC_{71}BM$ morphologies and corresponding variations in device performance for local stability testing with ringdown imaging.

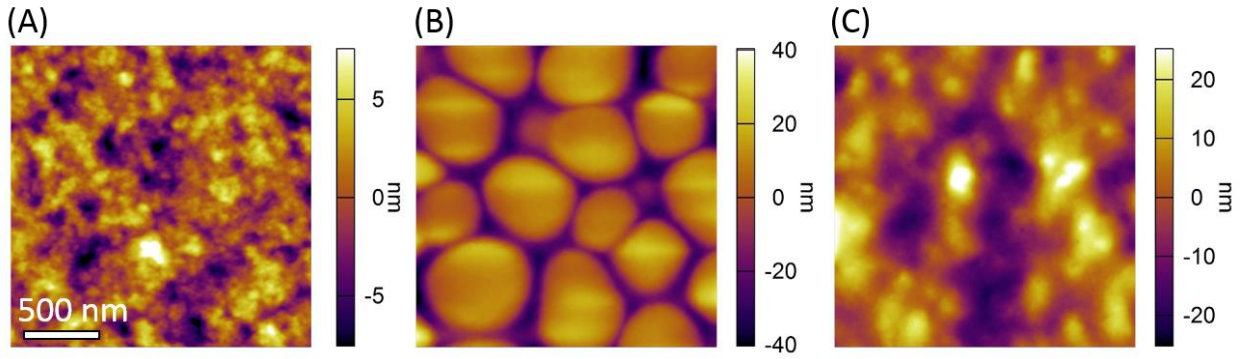

Figure 4.2 Representative AFM topography images of the film morphologies used in this study: (A) 1:1.5 3% DIO from DCB, (B) 1:3 No Additive from CB, and (C) 1:3 3% DIO from CB PTB7:$PC_{71}BM$.

Figure 4.2 shows representative AFM topography images of the different PTB7:$PC_{71}BM$ morphologies used in this study. Figure 4.2A shows the topography of the film from 1,2-dichlorobenzene (DCB) in a 1:1.5 polymer:fullerene ratio with DIO added. These films show the well-known, highly-mixed morphology that has been widely studied and produces very efficient devices for the PTB7:$PC_{71}BM$ system.[39] Figure 4.2B shows a highly phase-separated morphology with very poor performance generated by casting the film from chlorobenzene (CB) in a 1:3 polymer:fullerene ratio with no additive. Finally, Figure 4.2C shows the morphology resulting from a 1:3 polymer:fullerene ratio in CB, with 3% v/v ratio of DIO added just prior to spincoating.

Figure 4.2C shows that the effect of adding DIO is dramatic, and prevents the formation of the very large (250 – 500 nm) fullerene aggregates seen in Figure 4.2B, even at these higher fullerene concentrations. These three film morphologies exhibit very different device performance, as expected, but also exhibit extremely different stabilities, which we discuss next.

Figure 4.3 shows device EQE and local cantilever dissipation measurements for the three PTB7:$PC_{71}BM$ film morphologies shown in Figure 4.2 at varying doses of 660 nm light in air at room temperature and 27% humidity. The reported dose is calculated by measuring the light intensity of a 660 nm LED used for degradation (wavelength chosen for preferential excitation of PTB7)[17] and multiplying by the time of exposure. For local dissipation measurements, degradations were administered sequentially and *in situ* on the AFM setup by controlling the atmosphere of the flow cell encasing the sample and cantilever. During imaging, the sample is exposed to a constant flow of dry nitrogen, while during photooxidation a constant flow of compressed air of 27% relative humidity is used. For device EQE measurements, separate devices are degraded on a home-built photo-oxidation setup using a 660 nm LED and house air of 27% relative humidity. We note that exposure to air alone in the dark for over 10 hours had no measurable effect on the local electrical properties of the films, indicating the degradation is photoactivated.

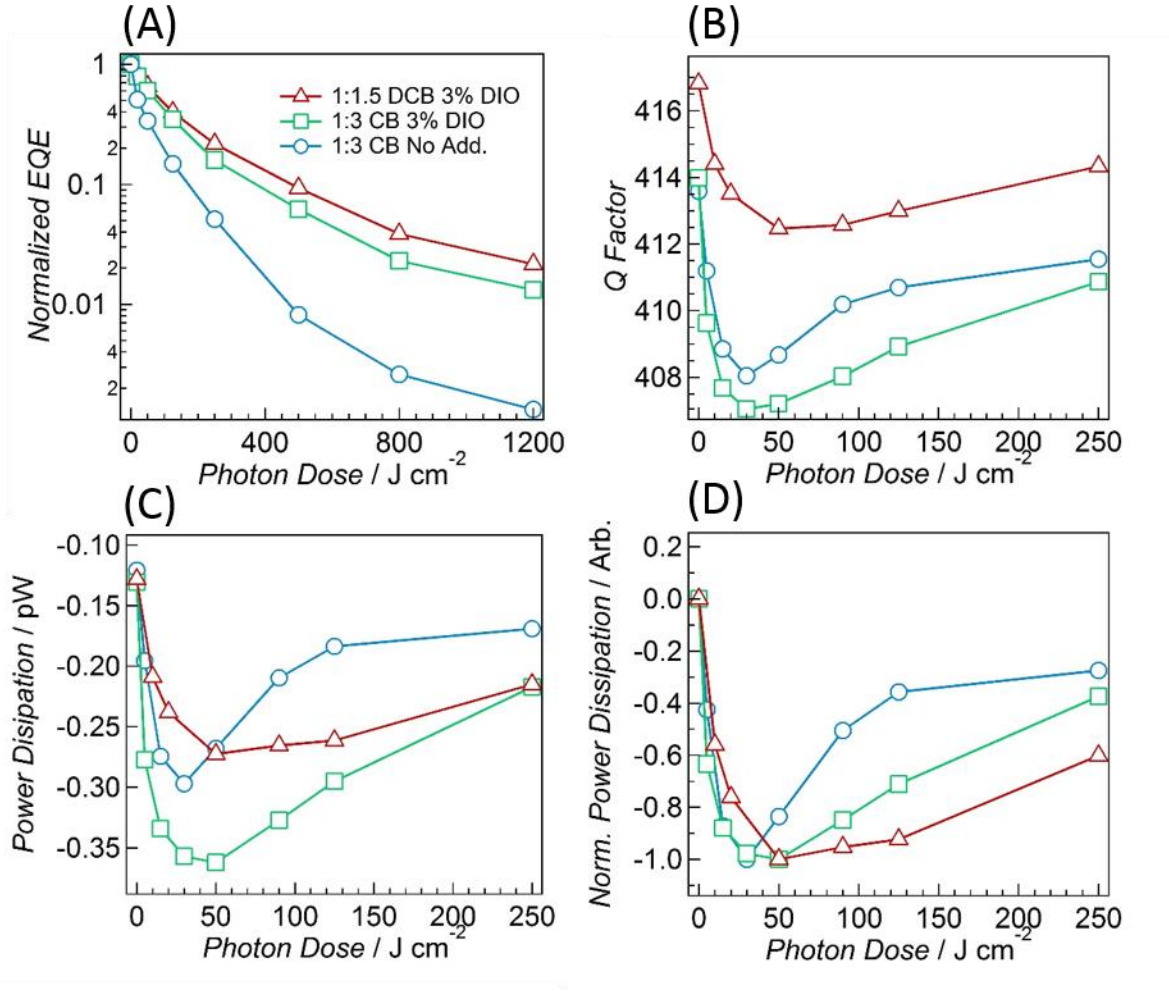

Figure 4.3 (A) Normalized EQE at 660 nm of 1:1.5 3% DIO from DCB (red trace, triangles), 1:3 3% DIO from CB (green trace, squares), and 1:3 No Additive from CB (blue trace, circles) PTB7:$PC_{71}BM$ devices from 0 to 1200 J/cm^2 photon dose. Remaining plots follow the same color/shape scheme. (B) Q factor, (C) cantilever power dissipation, and (D) normalized cantilever power dissipation as a function of photon dose.

Figure 4.3A shows the EQE of the 1:1.5 3% DIO (red triangles), 1:3 3% DIO (green squares), and 1:3 no additive (blue circles) PTB7:$PC_{71}BM$ devices as a function of degradation for doses up to 1200 J/cm^2. We report EQE at 660 nm, which coincides with the wavelength of excitation used in the AFM measurements for both degradation and imaging. The EQE traces are normalized so that the highest EQE is set to 1.0 (full EQE spectra and non-normalized comparison can be found in Appendix Figure C.2) to highlight the relative differences in rates of EQE decay.

Figure 4.3A shows that the film cast with DIO at a 1:1.5 polymer:fullerene ratio is the most stable with respect to EQE loss. In contrast, the film cast without DIO at a ratio of 1:3 loses photocurrent the fastest when exposed to photooxidation, but using DIO in conjunction with a 1:3 polymer:PCBM ratio increases both device performance and stability, placing it firmly in between the other two films. Interestingly, we observe that films with greater degrees of phase-separation not only begin with lower initial EQE values (initial EQE values at 660 nm are 69% for 1:1.5 DIO films, 55% for the 1:3 DIO films, and 21% for no additive 1:3 no additive films), but their performance also degrades at a faster rate when exposed to light and oxygen. We note that these results appear to contradict recent reports suggesting that residual DIO additive results in films that are less stable against photo-oxidation,[40] however those studies used photobleaching of the films as their primary metric of stability, whereas both our group[17] has found that device performance often drops much faster the absorbance of an OPV film, presumably because small densities of trap states can result in large recombination losses, without appreciably affecting the UV-Vis spectrum. Taken together, these results suggest that DIO processing may result in films that are less susceptible to early photo-oxidative damage, while being less stable to photobleaching over the long term.

Figure 4.3B shows the average cantilever Q factor measured via cantilever ringdown for the same three blend morphologies shown in Figure 4.2. The same cantilever was used for all three film morphologies, and each point in the plot was collected by imaging over a 4 μm^2 area of 32 x 32 pixels at 1 average/pixel and then averaging together all 1024 pixels over the imaged area. The area imaged is sufficiently large compared to the nanoscale structure of the films to be representative of general device performance (i.e. moving to another 4 μm^2 area would result in roughly the same values of Q). We plot Q and dissipation out to a photon dose of 250 J/cm^2 to more clearly show the most substantial changes that occur in the initial stages of degradation (full Q and dissipation versus dose curves are shown in Appendix Figure C.3 and C.4). For the 1:1.5 ratio film cast with DIO in Figure 4.3B, cantilever Q decreases by about 1% from 0 to 50 J/cm^2, which corresponds to an EQE loss of 35%. By a dose of 90 J/cm^2, Q has risen only slightly and increases at a slow rate before tapering off at higher doses. For the film cast at 1:3 polymer:fullerene ratio with DIO (green squares), Q drops by about 1.7% by a dose of only 30 J/cm^2, where EQE has decreased by ~30%. Q then rises for higher doses but at a rate faster than

the 1:1.5 film with DIO. Lastly, Q for the film cast without DIO at a 1:3 polymer:fullerene ratio drops by 1.3% by a dose of 30 J/cm^2, but then rises at a significantly faster rate than the other two films.

The sharp decline in cantilever Q during the beginning stages of degradation is a result of greater damping forces acting on the cantilever as photogenerated charge carriers move through the active layer. Since it has been shown that exposure to light and oxygen creates deep level traps in the fullerene,[28] we speculate that greater cantilever power dissipation is related to charge trapping in the photo-degraded film. We suggest that the fact that Q rises after reaching its minimum value can be explained by significant carrier losses occurring at higher photon doses. As carrier density decreases, the strength of the electrostatic forces between tip and sample declines, causing smaller detectable differences in cantilever Q when the sample is illuminated. Thus, when comparing these results to the device EQEs in Figure 4.3A, it is clear that the rate at which Q evolves with photo-oxidative damage correlates with device stability. This result shows that tracking cantilever Q with device degradation is an effective local stability probe.

An advantage of obtaining cantilever Q *via* the ringdown method over FM-EFM is the ability to quantitatively convert Q to cantilever power dissipation, which we plot in Figure 4.3C. We calculated dissipation according to Eq. 4.3, where the reported value is the *additional* cantilever power loss arising from interactions with photogenerated charge carriers compared to the purely mechanical losses. Values of dissipation that are more negative are higher in dissipation, as this is energy lost from the system. We find that initial cantilever power dissipation is nearly equivalent for the fresh, undamaged films. Similar to Q, cantilever power dissipation increases most drastically in the beginning stages of photooxidation before turning over and decreasing at higher doses when charge carrier losses become severe. In Figure 4.3D we normalize the dissipation versus dose traces such that initial dissipation is set to zero and maximum power dissipation is equal to one. In this manner, we highlight the differences between the three morphologies, particularly in the rate at which dissipation decreases at doses past 30 – 50 J/cm^2. This result is consistent with the device EQE measurements.

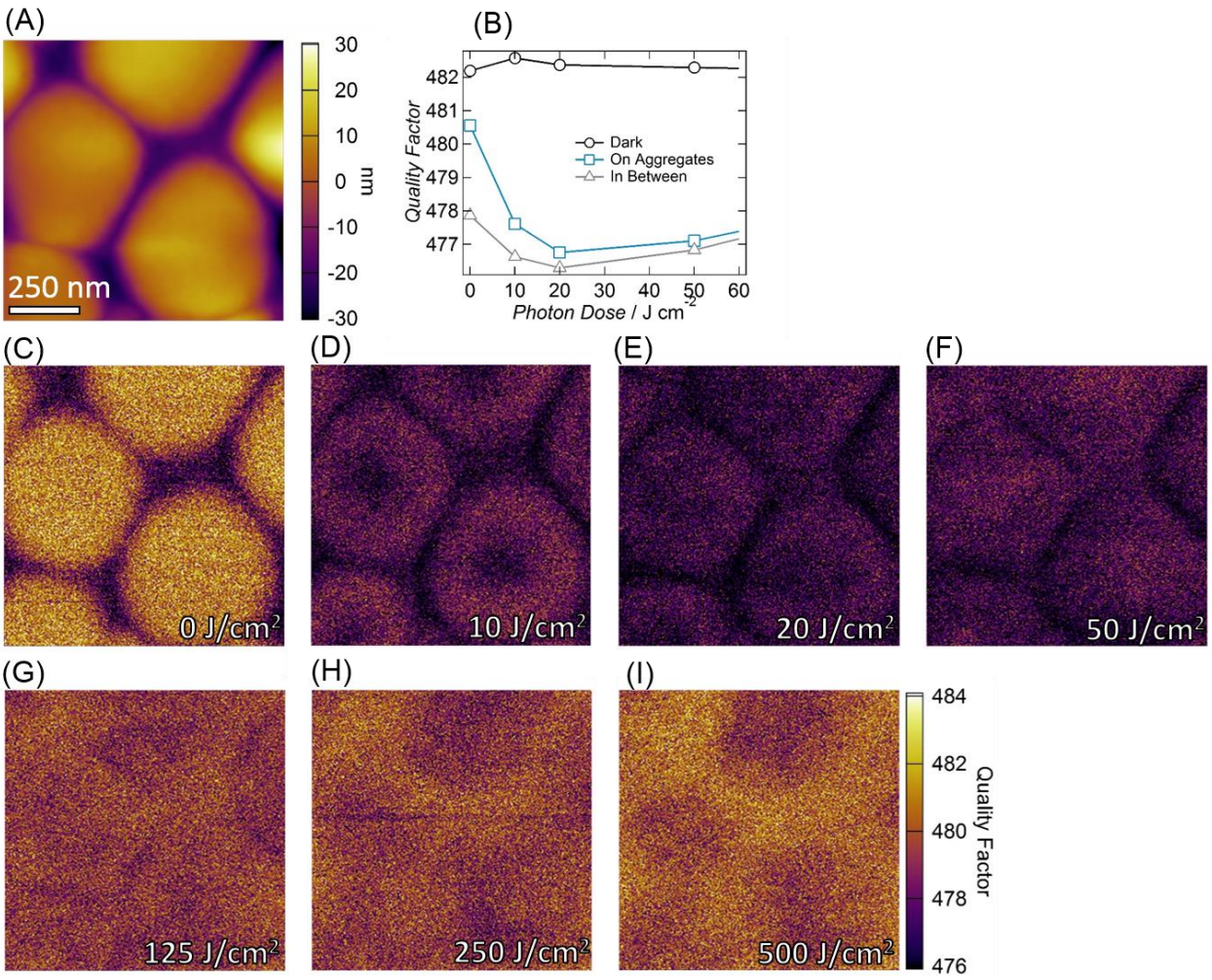

Figure 4.4 (A) Topography of a no additive 1:3 PTB7:$PC_{71}BM$ film. (B) Area averages of cantilever Q as a function of photon dose for fullerene aggregates (squares) and areas in between aggregates (triangles), as well as average Q taken in the dark with no tip bias for the entire region (circles). The different regions are masked off using the topography and selecting areas above or a below a particular height threshold. (C-I) Q images *via* cantilever ringdown of the same film degraded to (C) 0, (D) 10, (E) 20, (F) 50, (G) 125, (H) 250, and (I) 500 J/cm^2.

To better understand how degradation is accelerated by local film morphology in the 1:3 blend, we took high resolution Q images *via* cantilever ringdown to see which areas in the film exhibit the greatest changes upon exposure to light and oxygen. Figure 4.4 shows the Q images collected *via* cantilever ringdown of a 1:3 PTB7:$PC_{71}BM$ film cast with no solvent additive degraded *in situ* from 0 to 500 J/cm^2. Figure 4.4A shows the topography of the film, which consists

of very large fullerene aggregates roughly 250-500 nm in diameter with well-mixed regions of polymer and dispersed fullerene in between.[11] When the film is fresh in Figure 4.4C, we find significant heterogeneity in dissipation that reflects local film structure, with dissipation lowest directly on top of fullerene aggregates, and highest over the mixed regions occupying the space in between aggregates. After an initial dose of 10 J/cm^2, average Q for the image drops significantly, consistent with our results in Figure 4.3. However, the largest contribution to the average change in Q is due to substantial changes in Q directly on top of fullerene aggregates, with very little change in Q occurring over the mixed regions. This is illustrated more clearly in Figure 4.2B, where the average value of Q for masked regions of the film is plotted as a function of photon dose. Continuing to doses of 20 and 50 J/cm^2, changes in Q for both regions occur by roughly the same amount which continues to a dose of 125 J/cm^2. Past this point, Q for fullerene aggregate areas evolves at a slower rate than the mixed regions, eventually becoming highest in dissipation, with the well-mixed regions becoming lowest in dissipation. The significant heterogeneity in dissipation for the film cast without DIO is in sharp contrast to the films cast with DIO, which exhibited very little to no local variation in dissipation even after photo-oxidation due to the high degree of polymer/fullerene mixing (these images can be found in Appendix Figure C.5).

Based on our local Q images, it is clear that substantial increases in power dissipation occur during the initial steps of degradation, and that these increases in dissipation center on the large fullerene aggregates. The well-mixed regions in between aggregates appear to be substantially more resistant to changes in dissipation. This result suggests that a property intrinsic to fullerene aggregation is the root cause for instigating or accelerating photo-oxidative losses in photocurrent for polymer/fullerene solar cells. Reese and coworkers[28] found that oxidation of the PCBM fullerene cage was a critical component in degradation of the active layer for P3HT:PCBM solar cells. Despite minor changes in PCBM absorbance throughout photo-oxidation (i.e. minimal photobleaching of PCBM), they found with MALDI-TOF that the fullerene cage is oxidized by a single oxygen at a time, with the rate-limiting step being the first oxygen addition and subsequent additions occurring at a faster rate. Additionally, DFT calculations showed a monotonic decrease in the PCBM LUMO with each addition of oxygen, forming deep level traps in the active layer. With this in mind, our results suggest that the fast rise in power dissipation is caused by formation

of traps on the PCBM domains. Both the dense packing and longer carrier lifetimes[34] in fullerene aggregates give rise to a higher probability that electrons will reach these traps.

Although speculative, we can use this hypothesis to explain the differences in stability between the three different PTB7:$PC_{71}BM$ morphologies studied herein. By using EQE as a metric for device stability, we consider only how quickly losses in collected photocurrent occur as a function of photooxidation. This does not necessarily mean that photochemical reactions occur more quickly in films with large fullerene aggregates, but rather that pathways for photocurrent collection are eliminated at a faster rate. If this is the case, then films composed of large areas of densely packed traps (PCBM) will lose current collection pathways faster than when these same traps, even if they are generated at the same rate *via* photooxidation, are dispersed more evenly through the film. Thus, stability is enhanced when processing additives are used to reduce aggregation and disperse and distribute fullerene more uniformly within the polymer matrix, as seen in our results for both the 1:3 and 1:1.5 films cast with DIO. Other studies have also reported a strong fullerene influence on stability.[28, 34] This would indicate a more universal principle in polymer/fullerene solar cells that processing methods which reduce aggregation of the fullerene, or perhaps changing the electronic structure of fullerene, can enhance stability in polymer/fullerene solar cells.

4.3 Conclusion

We have developed an implementation of dissipation imaging *via* cantilever ringdown for the study of energy loss processes in organic semiconductor films. The ringdown time of the cantilever is directly related to cantilever energy loss when interacting with photogenerated charge carriers. We have shown that for three PTB7:$PC_{71}BM$ morphologies, cantilever power dissipation correlates with device stability, making ringdown imaging an effective local stability probe. We show that ringdown imaging is capable of resolving local heterogeneity in dissipation for phase-segregated films, and show that dissipation increases as a function of photodegradation more quickly in regions dominated by fullerene aggregation, providing local evidence in favor of reducing fullerene aggregation for more photochemically stable devices. Dissipation imaging *via* cantilever ringdown is a powerful technique for resolving charge carrier loss processes at

nanometer length scales and with further development will prove useful in understanding loss mechanisms in a variety of nanostructured energy materials.

4.4 METHODS

4.4.1 *Device Preparation*

Device fabrication and photo-oxidation procedures have been slightly modified from Ref. 12. PTB7:$PC_{71}BM$ devices were made from separate solutions of 25 mg/mL PTB7 (poly[[4,8-bis[(2-ethylhexyl)oxy]benzo[1,2-b:4,5-b']dithiophene-2,6-diyl][3-fluoro-2-[(2-ethylhexyl)carbonyl]thieno[3,4-b]thiophenediyl]]) (1-Material) and $PC_{71}BM$ (3'H-cyclopropa[8,25][5,6]fullerene-C71-D5h(6)-3'-butanoic acid, 3'-phenyl-, methyl ester) (American Dye Source) in 1,2-dichlorobenzene (Sigma-Aldrich) for the 1:1.5 blend and chlorobenzene (Sigma-Aldrich) for the 1:3 blends. ITO-coated glass substrates (Thin Film Devices) were sonicated in subsequent solutions of acetone and 2-propanol and plasma cleaned before spincoating a ~30 nm layer of PEDOT:PSS (Clevios P VP Al 4083, H.C. Starck Chemicals) and annealing at 150 °C under nitrogen for 20 minutes. The PTB7 and $PC_{71}BM$ solutions were stirred at 80 °C and 800 RPM for at least 12 hours before being combined by adding the PTB7 and $PC_{71}BM$ to a third vial in a 1:1.5 v/v ratio, or by adding the PTB7 directly into the $PC_{71}BM$ solution in a 1:3 v/v ratio. 1,8-diiodooctane (TCI Chemicals) was added at 3% v/v just prior to spincoating the 1:1.5 blend and the 1:3 blend with DIO. The final solutions were spincast from 70 °C to a final active layer thickness of ~100 nm in a nitrogen glovebox. Films were then dried in the glovebox at 80 °C on a hotplate. For device testing, 80 nm aluminum electrodes were thermally evaporated through a shadow mask, but only after the photo-oxidation process. Photo-oxidations were carried out in a controlled environment of ~27% relative humidity by flowing compressed air through a sealed chamber. Films were exposed to a 5 W 660 nm LED (LEDEngin LZ1-00R200) with an intensity of ~500 W/m^2. The intensity of the LED was measured using a calibrated Si-photodiode (OSI Optoelectronics) and sourcemeter (Keithley 2400). Photon doses are calculated by multiplying the power of the LED by the time of exposure.

4.4.2 *Device Measurements*

External quantum efficiencies were measured with a monochromated 250 W tungsten-halogen lamp (Acton) and sourcemeter (Keithley 2400) and referenced to a calibrated Si-photodiode (OSI-optoelectronics). A device mask ensured the same 0.013 cm^2 area was illuminated during each measurement. For very low EQE values lock-in detection EQE was performed with a Stanford Research Systems lock-in amplifier for enhanced signal to noise.

4.4.3 *Atomic Force Microscopy*

AFM measurements were taken with an Asylum Research MFP-3D BIO atomic force microscope (Oxford Instruments) installed on an inverted Nikon Eclipse Ti inverted microscope and Table Stable vibration isolation stage. 320 kHz resonance frequency silicon cantilevers with conductive Pt coating (MikroMasch) were used for all measurements. Samples were housed in a closed flow-cell where the environment could be controlled by flowing either nitrogen (for imaging) or compressed air (for photo-oxidation, relative humidity 27%) through the enclosure. Before photo-oxidation, compressed air was flowed through the enclosure for 5 minutes. After photo-oxidation, the enclosure was purged with nitrogen for 5 minutes before imaging with illumination using a 10 W 660 nm LED (LEDEngin LZ4-series) at ~900 W/m^2 (intensity measurements vary slightly by day and are retaken each time an AFM trial is performed) through diffuser (Thor Labs). *In situ* photo-oxidation is carried out with the 660 nm LED over an area of ~2120 μm^2. Q images were taken with a 20 nm lift height, drive amplitude set to ~30% of the topography pass amplitude, and +10 V bias on the tip, with the sample ITO attached to ground. Tip parameters such as spring constant and amplitude inverse optical lever sensitivity are calibrated for quantitative conversion of Q into power dissipation.

4.5 ACKNOWLEDGEMENTS

We thank Dr. David Moerman for many thought-provoking discussions on the physics behind cantilever energy loss in semiconductor systems.

4.6 REFERENCES

1. Jørgensen, M.; Norrman, K.; Krebs, F. C. Stability/Degradation of Polymer Solar Cells. *Sol. Energy Mater. Sol. Cells* **2008,** *92*, 686-714.
2. Jorgensen, M.; Norrman, K.; Gevorgyan, S. A.; Tromholt, T.; Andreasen, B.; Krebs, F. C. Stability of Polymer Solar Cells. *Adv. Mater. (Weinheim, Ger.)* **2012,** *24*, 580-612.
3. Peters, C. H.; Sachs-Quintana, I. T.; Mateker, W. R.; Heumueller, T.; Rivnay, J.; Noriega, R.; Beiley, Z. M.; Hoke, E. T.; Salleo, A.; McGehee, M. D. The Mechanism of Burn-in Loss in a High Efficiency Polymer Solar Cell. *Adv. Mater. (Weinheim, Ger.)* **2012,** *24*, 663-+.
4. Madsen, M. V.; Tromholt, T.; Norrman, K.; Krebs, F. C. Concentrated Light for Accelerated Photo Degradation of Polymer Materials. *Adv. Energy Mater.* **2013,** *3*, 424-427.
5. Alem, S.; Wakim, S.; Lu, J.; Robertson, G.; Ding, J.; Tao, Y. Degradation Mechanism of Benzodithiophene-Based Conjugated Polymers When Exposed to Light in Air. *ACS Appl. Mater. Interfaces* **2012**.
6. Nikiforov, M. P.; Strzalka, J.; Darling, S. B. Delineation of the Effects of Water and Oxygen on the Degradation of Organic Photovoltaic Devices. *Sol. Energy Mater. Sol. Cells* **2013,** *110*, 36-42.
7. Angmo, D.; Sommeling, P. M.; Gupta, R.; Hösel, M.; Gevorgyan, S. A.; Kroon, J. M.; Kulkarni, G. U.; Krebs, F. C. Outdoor Operational Stability of Indium-Free Flexible Polymer Solar Modules over 1 Year Studied in India, Holland, and Denmark. *Advanced Engineering Materials* **2014,** *16*, 976-987.
8. Kawano, K.; Pacios, R.; Poplavskyy, D.; Nelson, J.; Bradley, D. D. C.; Durrant, J. R. Degradation of Organic Solar Cells Due to Air Exposure. *Sol. Energy Mater. Sol. Cells* **2006,** *90*, 3520-3530.
9. Matsumoto, F.; Vorpahl, S. M.; Banks, J. Q.; Sengupta, E.; Ginger, D. S. Photodecomposition and Morphology Evolution of Organometal Halide Perovskite Solar Cells. *The Journal of Physical Chemistry C* **2015,** *119*, 20810-20816.
10. Niu, G.; Guo, X.; Wang, L. Review of Recent Progress in Chemical Stability of Perovskite Solar Cells. *J. Mater. Chem. A.* **2015,** *3*, 8970-8980.
11. Collins, B. A.; Li, Z.; Tumbleston, J. R.; Gann, E.; McNeill, C. R.; Ade, H. Absolute Measurement of Domain Composition and Nanoscale Size Distribution Explains Performance in Ptb7:Pc71bm Solar Cells. *Adv. Energy Mater.* **2013,** *3*, 65-74.
12. Cox, P. A.; Glaz, M. S.; Harrison, J. S.; Peurifoy, S. R.; Coffey, D. C.; Ginger, D. S. Imaging Charge Transfer State Excitations in Polymer/Fullerene Solar Cells with Time-Resolved Electrostatic Force Microscopy. *The Journal of Physical Chemistry Letters* **2015,** *6*, 2852-2858.
13. Giridharagopal, R.; Ginger, D. S. Characterizing Morphology in Bulk Heterojunction Organic Photovoltaic Systems. *J. Phys. Chem. Lett.* **2010,** *1*, 1160-1169.
14. Groves, C.; Reid, O. G.; Ginger, D. S. Heterogeneity in Polymer Solar Cells: Local Morphology and Performance in Organic Photovoltaics Studied with Scanning Probe Microscopy. *Acc. Chem. Res.* **2010,** *43*, 612-620.
15. Mateker, W. R.; Heumueller, T.; Cheacharoen, R.; Sachs-Quintana, I. T.; McGehee, M. D.; Warnan, J.; Beaujuge, P. M.; Liu, X.; Bazan, G. C. Molecular Packing and Arrangement Govern the Photo-Oxidative Stability of Organic Photovoltaic Materials. *Chem. Mater.* **2015,** *27*, 6345-6353.
16. Kumar, A.; Hong, Z.; Sista, S.; Yang, Y. The Critical Role of Processing and Morphology in Determining Degradation Rates in Polymer Solar Cells. *Adv. Energy Mater.* **2011,** *1*, 124-131.

17. Cox, P. A.; Waldow, D. A.; Dupper, T. J.; Jesse, S.; Ginger, D. S. Mapping Nanoscale Variations in Photochemical Damage of Polymer/Fullerene Solar Cells with Dissipation Imaging. *ACS Nano* **2013,** *7*, 10405-10413.
18. Reid, O. G.; Rayermann, G. E.; Coffey, D. C.; Ginger, D. S. Imaging Local Trap Formation in Conjugated Polymer Solar Cells: A Comparison of Time-Resolved Electrostatic Force Microscopy and Scanning Kelvin Probe Imaging†. *J. Phys. Chem. C* **2010,** *114*, 20672-20677.
19. Sengupta, E.; Domanski, A. L.; Weber, S. A. L.; Untch, M. B.; Butt, H.-J.; Sauermann, T.; Egelhaaf, H. J.; Berger, R. Photoinduced Degradation Studies of Organic Solar Cell Materials Using Kelvin Probe Force and Conductive Scanning Force Microscopy. *J. Phys. Chem. C* **2011,** *115*, 19994-20001.
20. Lu, L.; Zheng, T.; Wu, Q.; Schneider, A. M.; Zhao, D.; Yu, L. Recent Advances in Bulk Heterojunction Polymer Solar Cells. *Chem. Rev. (Washington, DC, U. S.)* **2015**.
21. Lou, S. J.; Szarko, J. M.; Xu, T.; Yu, L.; Marks, T. J.; Chen, L. X. Effects of Additives on the Morphology of Solution Phase Aggregates Formed by Active Layer Components of High-Efficiency Organic Solar Cells. *J. Am. Chem. Soc.* **2011,** *133*, 20661-3.
22. Liang, Y.; Xu, Z.; Xia, J.; Tsai, S. T.; Wu, Y.; Li, G.; Ray, C.; Yu, L. For the Bright Future-Bulk Heterojunction Polymer Solar Cells with Power Conversion Efficiency of 7.4%. *Adv. Mater. (Weinheim, Ger.)* **2010,** *22*, E135-8.
23. Córcoles, L.; Abad, J.; Padilla, J.; Urbina, A. Wavelength Influence on the Photodegradation of P3ht:Pcbm Organic Solar Cells. *Sol. Energy Mater. Sol. Cells* **2015,** *141*, 423-428.
24. Guerrero, A.; Heidari, H.; Ripolles, T. S.; Kovalenko, A.; Pfannmöller, M.; Bals, S.; Kauffmann, L.-D.; Bisquert, J.; Garcia-Belmonte, G. Shelf Life Degradation of Bulk Heterojunction Solar Cells: Intrinsic Evolution of Charge Transfer Complex. *Adv. Energy Mater.* **2015,** *5*, 1614-6840.
25. Kettle, J.; Waters, H.; Ding, Z.; Horie, M.; Smith, G. C. Chemical Changes in Pcpdtbt:Pcbm Solar Cells Using Xps and Tof-Sims and Use of Inverted Device Structure for Improving Lifetime Performance. *Sol. Energy Mater. Sol. Cells* **2015,** *141*, 139-147.
26. Romero-Gomez, P.; Betancur, R.; Martinez-Otero, A.; Elias, X.; Mariano, M.; Romero, B.; Arredondo, B.; Vergaz, R.; Martorell, J. Enhanced Stability in Semi-Transparent Ptb7/Pc71bm Photovoltaic Cells. *Sol. Energy Mater. Sol. Cells* **2015,** *137*, 44-49.
27. Denk, W.; Pohl, D. W. Local Electrical Dissipation Imaged by Scanning Force Microscopy. *Appl. Phys. Lett.* **1991,** *59*, 2171.
28. Reese, M. O.; Nardes, A. M.; Rupert, B. L.; Larsen, R. E.; Olson, D. C.; Lloyd, M. T.; Shaheen, S. E.; Ginley, D. S.; Rumbles, G.; Kopidakis, N. Photoinduced Degradation of Polymer and Polymer–Fullerene Active Layers: Experiment and Theory. *Adv. Funct. Mater.* **2010,** *20*, 3476-3483.
29. Schafferhans, J.; Baumann, A.; Wagenpfahl, A.; Deibel, C.; Dyakonov, V. Oxygen Doping of P3ht:Pcbm Blends: Influence on Trap States, Charge Carrier Mobility and Solar Cell Performance. *Org. Electron.* **2010,** *11*, 1693-1700.
30. Heumueller, T.; Burke, T. M.; Mateker, W. R.; Sachs-Quintana, I. T.; Vandewal, K.; Brabec, C. J.; McGehee, M. D. Disorder-Induced Open-Circuit Voltage Losses in Organic Solar Cells During Photoinduced Burn-In. *Adv. Energy Mater.* **2015,** *5*, n/a-n/a.
31. Cleveland, J. P.; Anczykowski, B.; Schmid, A. E.; Elings, V. B. Energy Dissipation in Tapping-Mode Atomic Force Microscopy. *Appl. Phys. Lett.* **1998,** *72*, 2613.

32. B. Anczykowski, B. G., H. Fuchs, J.P. Cleveland, V.B. Elings. How to Measure Energy Dissipation in Dynamic Mode Atomic Force Microscopy. *Appl. Surf. Sci.* **1998,** *140*, 376-382.
33. Jesse, S.; Kalinin, S. V.; Proksch, R.; Baddorf, A. P.; Rodriguez, B. J. The Band Excitation Method in Scanning Probe Microscopy for Rapid Mapping of Energy Dissipation on the Nanoscale. *Nanotechnology* **2007,** *18*, 435503.
34. Hoke, E. T.; Sachs-Quintana, I. T.; Lloyd, M. T.; Kauvar, I.; Mateker, W. R.; Nardes, A. M.; Peters, C. H.; Kopidakis, N.; McGehee, M. D. The Role of Electron Affinity in Determining Whether Fullerenes Catalyze or Inhibit Photooxidation of Polymers for Solar Cells. *Adv. Energy Mater.* **2012,** *2*, 1351-1357.
35. Gannepalli, A.; Yablon, D. G.; Tsou, A. H.; Proksch, R. Mapping Nanoscale Elasticity and Dissipation Using Dual Frequency Contact Resonance Afm. *Nanotechnology* **2011,** *22*, 355705.
36. Coffey, D. C.; Ginger, D. S. Time-Resolved Electrostatic Force Microscopy of Polymer Solar Cells. *Nat. Mater.* **2006,** *5*, 735-740.
37. Albrecht, T. R.; Grütter, P.; Horne, D.; Rugar, D. Frequency Modulation Detection Using High-Q Cantilevers for Enhanced Force Microscope Sensitivity. *J. Appl. Phys.* **1991,** *69*, 668.
38. He, Z.; Zhong, C.; Su, S.; Xu, M.; Wu, H.; Cao, Y. Enhanced Power-Conversion Efficiency in Polymer Solar Cells Using an Inverted Device Structure. *Nat Photon* **2012,** *6*, 591-595.
39. Lu, L.; Yu, L. Understanding Low Bandgap Polymer Ptb7 and Optimizing Polymer Solar Cells Based on It. *Adv. Mater. (Weinheim, Ger.)* **2014,** *26*, 4413-4430.
40. Tremolet de Villers, B. J.; O'Hara, K. A.; Ostrowski, D. P.; Biddle, P. H.; Shaheen, S. E.; Chabinyc, M. L.; Olson, D. C.; Kopidakis, N. Removal of Residual Diiodooctane Improves Photostability of High-Performance Organic Solar Cell Polymers. *Chem. Mater.* **2016,** *28*, 876-884.

Chapter 5. Conclusions and Future Directions

We have presented three scanning probe microscopy methods based on EFM for probing local optoelectronic properties in nanostructured solar materials. In each case, the properties studied were all affected by the local morphology of the materials system, demonstrating the need for such local probes in better understanding the underlying physics behind device operation and stability at the nanoscale. The methods presented here were demonstrated on polymer/fullerene solar materials, but their operation requires only the ability to measure variations in capacitive force gradients or cantilever power dissipation due to charge motion, making them widely applicable to any materials system with dynamic charge carriers.

In chapter one we studied the weakly absorbing charge transfer state in polymer/fullerene solar cells with time-resolved electrostatic force microscopy. We showed that if excitation wavelength is varied across the solar spectrum, our trEFM measurements are proportional to device EQE, even for the low photocurrents associated with charge transfer states. We demonstrated that trEFM is sensitive to currents as low as a few attoAmps, making it well-suited to studying the low currents obtained from sub-gap excitation. We used trEFM to collect local EQE maps of two very different morphologies of MDMO-PPV:PCBM films, and found that while the local distribution of EQE varies with local film composition, it does not vary with excitation wavelength. This result provided nanoscale evidence in support of a controversial result that internal quantum efficiency does not vary with excitation wavelength, and that the probability of forming separated charge carriers is equivalent regardless of whether the exciton is formed at the singlet or charge transfer state.

Our study used the polymer/fullerene system MDMO-PPV:PCBM, which has been studied in great detail for over a decade. Today, some of the highest performing solar materials such as PTB7 and its variants have a greater amorphous character than polyphenylvinylenes such as MDMO-PPV. Thus, a straightforward continuation of this study would be to image the local CT state properties of newer, state-of-the-art materials. Is the probability that charge carriers form from above- and below-gap excitation equivalent for these newer polymers as well? Or does the local distribution of EQEs vary with excitation wavelength? The high sensitivity of trEFM to

capacitive force gradient changes allows for detection of very low currents (attoAmpere levels). It would be interesting to take advantage of this sensitivity and apply it to sub-gap states in other materials, such as defect states in organometal halide perovskites, another solar material whose film structure is intimately tied to overall device performance. Does the current acquired from these sub-gap states decrease with common surface passivation treatments? Furthermore, we showed that trEFM can be used as a local EQE probe for a range of excitation wavelengths. In theory, then, it should be possible to collect nanoscale EQE spectra using the right excitation source – a high power monochromated white light source coupled into the AFM setup that can be toggled on and off with <10 μs rise times but remain on for ~4 ms at a time would accomplish this. EQE spectra could then be collected as a function of local materials properties.

In chapter three we showed that the cantilever amplitude measured *via* frequency-modulated electrostatic force microscopy is inversely proportional to cantilever energy dissipation, and that this parameter is highly sensitive to photo-oxidative changes in organic semiconductor materials. Using PTB7:$PC_{71}BM$ as a model system, we found that decreases in cantilever amplitude were related to EQE loss over the functional lifetime of a device, and that local variations in dissipation exist when films are cast with or without the solvent additive 1,8-diiodooctane. Our EQE measurements confirmed that films cast with the additive were more stable, explaining the slower evolution of local power dissipation as a function of degradation. We qualitatively compared our dissipation measurements to those measured with impedance spectroscopy by imaging the same photodegraded spots with multiple cantilevers of varying resonance frequencies which suggests FM-EFM measurements may be related to the imaginary term of the complex relative permittivity.

Further development of the actual physical properties in organic semiconductors that give rise to variations in local dissipation would propel this instrumental capability forward into a much more broadly applicable technique. At the moment, we can only hypothesize that charge carrier trapping and detrapping is responsible for energy loss in the cantilever. If we knew for certain trapping/detrapping was the dominant mechanism, the imaging technique would be more robust and could be applied to a range of systems with more straightforward interpretation of the results, potentially serving as a quick nanoscale check for intrinsic charge carrier loss for a range of processing conditions or materials. FM-EFM can only qualitatively be used to measure dissipation

in materials, a drawback when compared to our ringdown technique presented in chapter four. However, FM-EFM images can be collected quickly at high resolution. While it may make more sense to develop the theory behind dissipation imaging with a quantitative technique such as ringdown imaging, once the principles are known FM-EFM will benefit researchers as a commercially available and fast imaging tool for studying loss processes in solar cells.

In chapter four we presented our method for quantitatively measuring cantilever Q, and thus cantilever energy dissipation, by implementing a version of cantilever ringdown imaging. Collecting cantilever Q as a function of film degradation shows that initially total cantilever power dissipation increases with increasing levels of film damage and maximizes at a level indicative of the device lifetime. By comparing device EQE measurements for three very different PTB7:$PC_{71}BM$ film morphologies with our local dissipation measurements, we show that measuring cantilever power dissipation as a function of materials degradation is correlated with device stability. For PTB7 morphologies comprised of significant fullerene aggregation, we find that dissipation increases significantly faster with degradation in areas of high fullerene concentration than in well-mixed regions. These results are consistent with other studies that show the fullerene has a profound effect on device stability.

Similar to FM-EFM, ringdown imaging would benefit from a more robust understanding of the underlying physical processes in semiconductor materials that lead to cantilever energy loss. In the case of ringdown imaging, quantitative measurements can be made, making it ideal for image to image and sample to sample comparisons. Preliminary results show that tracking cantilever Q as a function of degradation can be used to study local performance loss in organometal halide perovskite devices, making ringdown imaging more broadly applicable. While we have thus far measured cantilever Q changes with device degradation, Q should be sensitive to a variety of variables in semiconductor systems. Therefore, future studies that track Q as a function of changing materials properties can be performed. Beyond solar materials, measuring cantilever Q can be applied to other electronically active systems as well.

With further advances and development, local scanning probes will continue to play an integral part in our ability to design robust and efficient electronic devices. Beyond the organic solar materials studied here, many emerging device technologies make use of similarly

nanostructured materials whose morphology profoundly influences device performance. Therefore, the contributions to general scanning probe presented in this dissertation will serve to more broadly impact materials design fields in the future.

APPENDIX A.

Appendix A accompanies Chapter 2. Imaging Charge Transfer State Excitations in Polymer/Fullerene Solar Cells with Time-Resolved Electrostatic Force Microscopy

1. LED Spectra and Si diode responsivity used in EQE adjustments for Figure 2B.

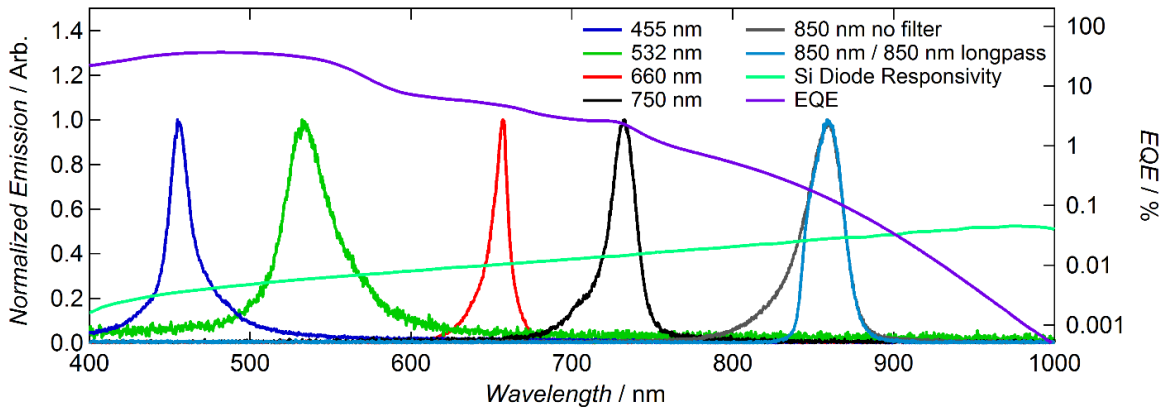

Figure A.1 The LED emission spectra, Si diode responsivity, and EQE used in the construction of Figure 2.2B.

Figure A.1 shows the led emission spectra at 455, 532, 660, 750 and 850 nm along with the Si diode responsivity and EQE of 1:4 MDMO-PPV:PCBM in chlorobenzene. Due to the broad spectrum of the LEDs, the responsivity used in calculating LED intensities and EQE used in Figure 2.2B was calculated using a weighted average of the emission spectra.

2. Point scans of 1:4 MDMO-PPV:PCBM cast from chlorobenzene at various wavelengths and intensities used for Figure 2B.

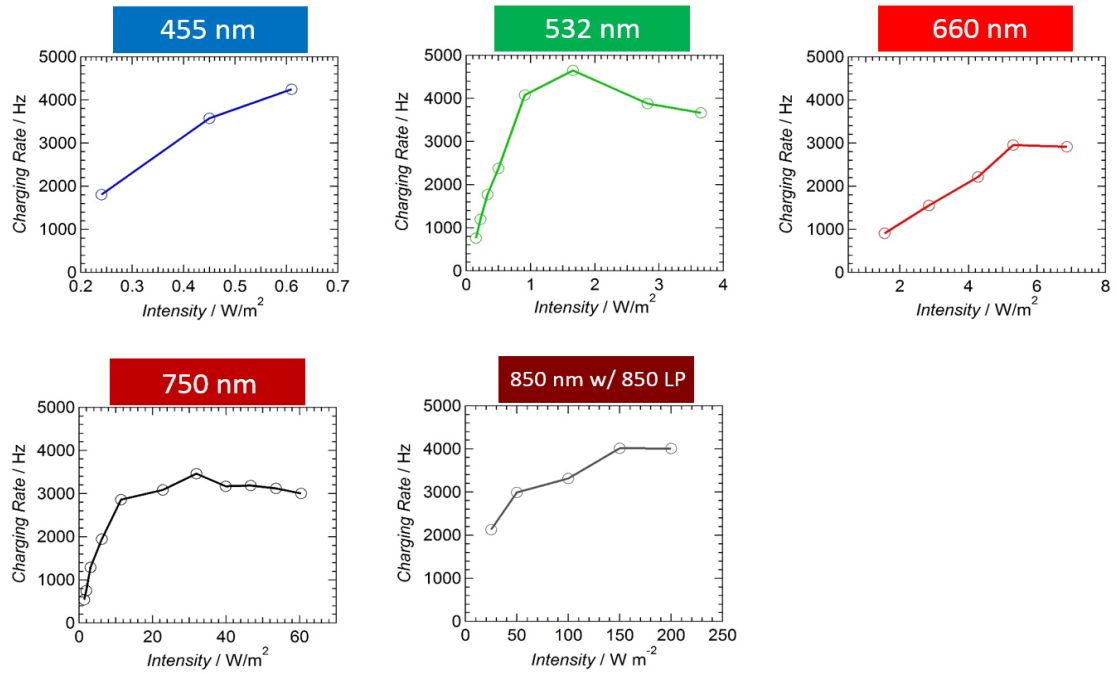

Figure A.2 trEFM point scans of a 1:4 MDMO-PPV:PCBM film cast from chlorobenzene at wavelengths 455, 523, 660, 750, and 850 nm with 850 nm longpass filter as a function of LED intensity.

Figure A.2 shows trEFM charging rate point scans for a 1:4 MDMO-PPV:PCBM film cast from chlorobenzene at wavelengths 455, 532, 660, 750, and 850 nm with an 850 nm longpass filter as a function of LED intensity. The intensity is lowered until the cantilever frequency shift is slow enough as to not be faster than the feedback loop that keeps the cantilever at resonance. The charging rate is approximately linear with LED intensity once the charging rate is appropriately slow enough to measure. This is shown in Figure A.2 where the charging rate plateaus for high LED intensities, but decreases linearly when LED intensity is low enough. To construct Figure 2.1B, the charging rates from Figure A.2 are normalized to photons/s incident on the film, and then averaged together to yield a value that resembles "charges/photons" so that the trEFM charging rates can better be compared to the bulk device EQEs. We used only charging rates that are within

the linear regime and/or under 4000 Hz (which equates to a slower than 250 μs charging rate, well within our instrumental resolution).

3. Frequency shift images of 1:4 MDMO-PPV:PCBM film cast from toluene.

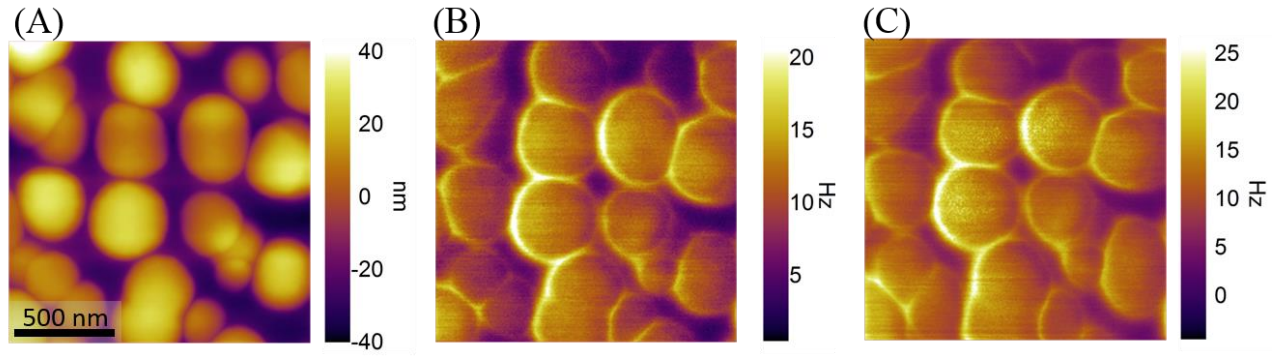

Figure A.3 (A) Topography, (B) singlet state and (C) CT state frequency shift images of a 1:4 MDMO-PPV:PCBM film cast from toluene.

The frequency shift images in Figure A.3 accompany the charging rate images in Figure 2.3 for the 1:4 MDMO-PPV:PCBM film cast from toluene. The frequency shift is largest over the fullerene aggregates, despite having the slowest charging rates. This is likely due to greater charge carrier density in areas where the film is thicker (this is consistent with what is reported in reference 20).

4. Frequency shift images of 1:4 MDMO-PPV:PCBM film cast from chlorobenzene.

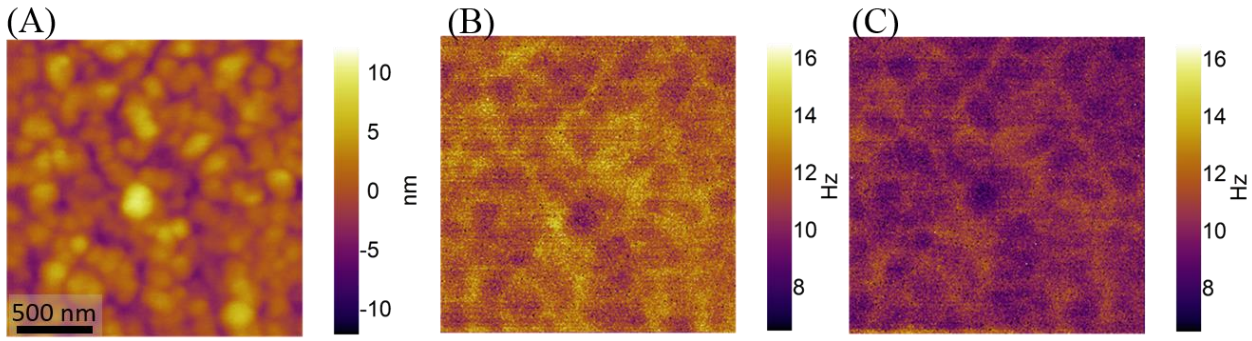

Figure A.4 (A) Topography, (B) singlet state and (C) CT state frequency shift images of a 1:4 MDMO-PPV:PCBM film cast from chlorobenzene.

The frequency shift images in Figure A.4 accompany the charging rate images in Figure 2.4 for the 1:4 MDMO-PPV:PCBM film cast from chlorobenzene. In this case, the frequency shift is smallest in areas of higher topography, which is contrast to the film cast from toluene. The structure in the frequency shift images is not seen in the charging rate images. Note that a slight drift occurred in between imaging Figure A.4B and Figure A.4C.

5. MDMO-PPV and PCBM neat trEFM point scans.

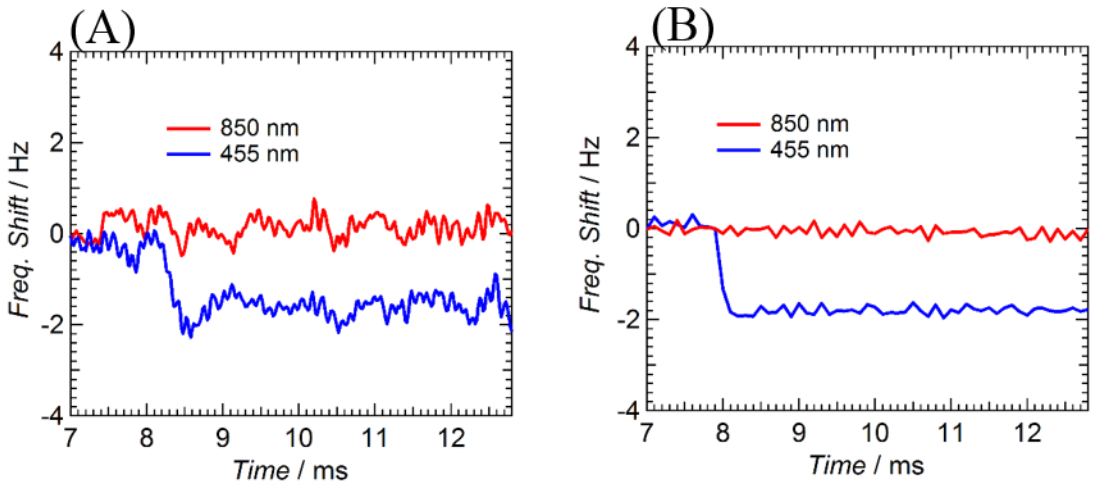

Figure A.5 Frequency shift traces of trEFM point scans for (A) neat MDMO-PPV and (B) neat PCBM films excited at 455 nm and 850 nm. Without both materials present in the film, there is no detectable frequency shift/charging rate at the wavelength where CT state absorption occurs.

In Figure A.5 we show the frequency shift traces of trEFM point scans done on films of neat MDMO-PPV and neat PCBM at wavelengths 455 and 850 nm. Here we show that without both materials present in the film there is no detectable charging rate at 850 nm where CT state absorption occurs (even at the highest LED intensity we can create in the AFM at 850 nm). There is, however, a detectable change at the wavelength where singlet state absorption occurs in either material.

6. Incremental addition of wt/wt% PCBM to establish lower limits of CT state resolution.

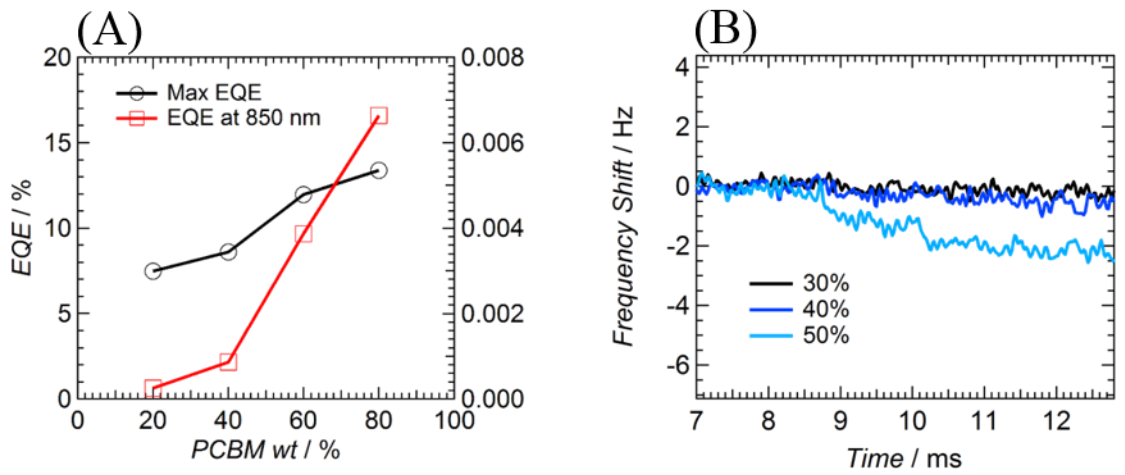

Figure A.6 (A) External quantum efficiency measurements for devices cast from chlorobenzene where the mass of MDMO-PPV is held constant and PCBM wt/wt% is incrementally increased. The black curve (circles) corresponds to the left axis and is the maximum EQE of each device. The red curve (squares) corresponds to the right axis and is the EQE at 850 nm. (B) trEFM point scans as a function of PCBM wt/wt% excited at 850 nm with an 850 nm longpass filter.

In Figure A.6A we show the external quantum efficiencies of a series of devices cast from chlorobenzene where the mass of MDMO-PPV is held constant and the wt/wt% of PCBM is increased from one device to the next. We find that as a function of PCBM weight content, the EQE at 850 nm (corresponding to direct to CT state excitation) grows in at a faster rate than the EQE of singlet state excitation. Additionally, we can resolve the EQE at 850 nm down to ~0.0002-0.0003% beginning at 20% PCBM content. At 10% PCBM content (not shown) the structure of the EQE spectrum resembles that of pure MDMO-PPV. Figure A.6B shows trEFM point scans using 850 nm (and 850 nm longpass filter) excitation of similar devices fabricated as a function of PCBM content. Here we find that our trEFM instrumentation is capable of resolving CT state originating charge carriers down to 50% PCBM content, and possibly at 40% (the charging rate is too slow to fit adequately though a slight frequency shift does exist). Based on our bulk device EQE results, our trEFM measurements are capable of resolving EQEs down to ~0.001-0.002%.

7. Photoconductive-AFM and trEFM images of MDMO-PPV:PCBM devices.

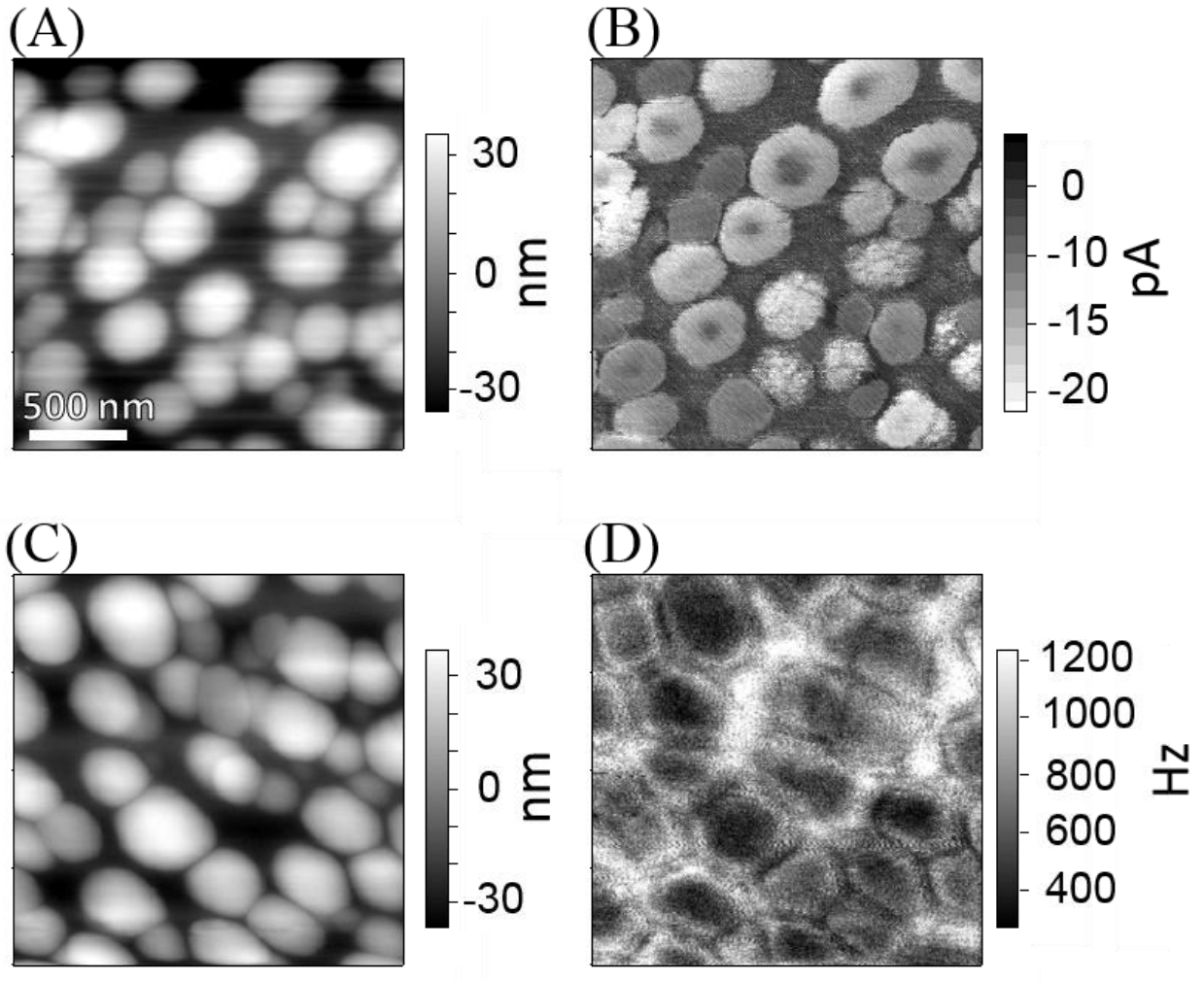

Figure A.7 (A) Topography and (B) corresponding photoconductive current map for a 1:4 MDMO-PPV:PCBM film cast from toluene. (C) Topography and (D) corresponding trEFM charging rate map for the same film.

Figure A.7A and B show the topography and current maps obtained through photoconductive AFM (pcAFM) of a 1:4 MDMO-PPV:PCBM film cast from toluene. With pcAFM, photocurrent is collected primarily on top of fullerene aggregates, with lower current collection in the middle of the aggregates. No current is collected in between the fullerene aggregates. Figure A.7C and D show topography and charging rate images obtained through trEFM for the same film. In this case, photocurrent is collected in all areas, but primarily in

between the aggregates, which is in sharp contrast to the current map obtained with pcAFM. pcAFM is less sensitive and prone to tip contact effects, making it unreliable in collecting photocurrent in the regions in between the aggregates.

8. Correlation Scatter Plots

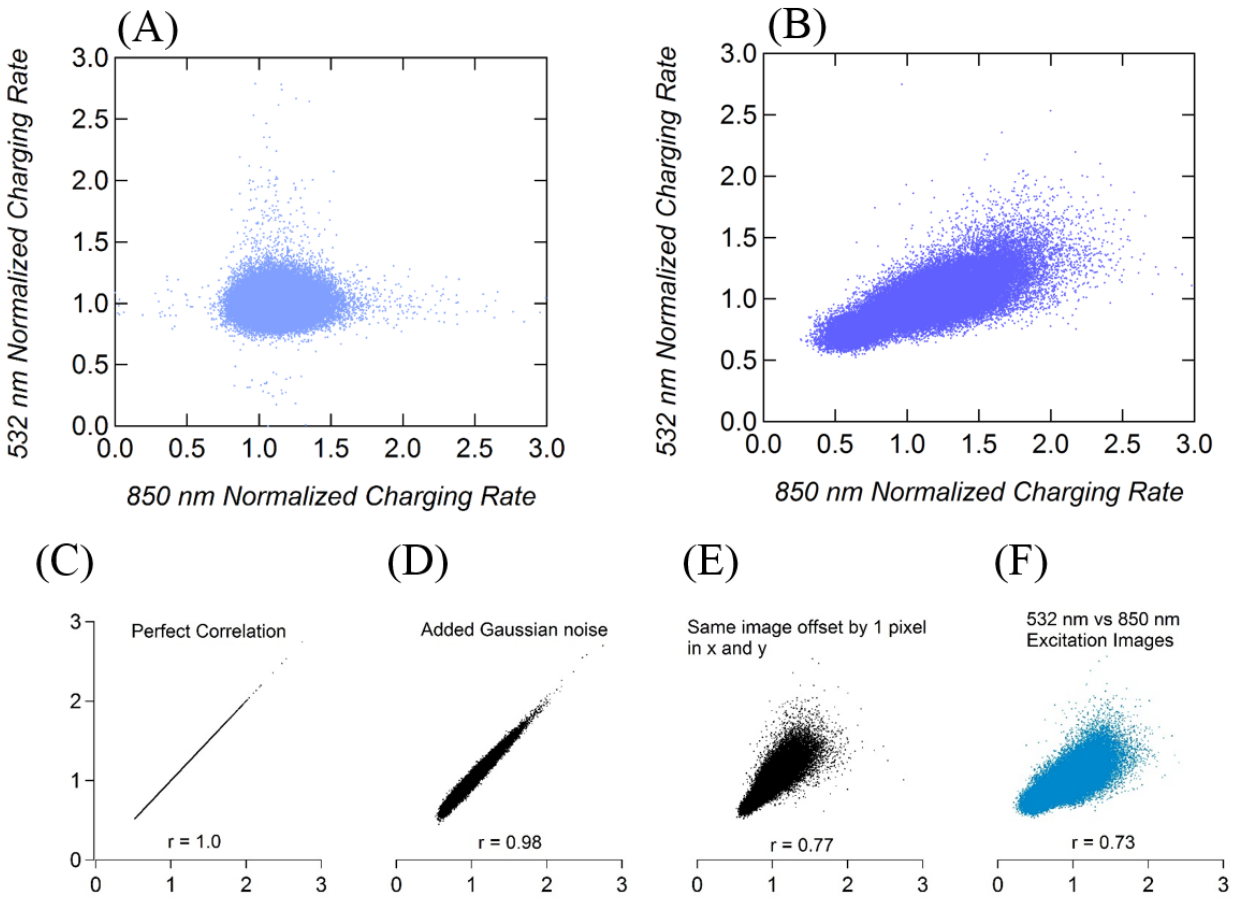

Figure A.8 Analysis of the correlation between the 532 nm and 850 nm charging rate images shows that the correlation is very strong approaching that expected within experimental limits. (A) Correlation plot of the 532 nm photoexcitation charging rates versus 850 nm photoexcitation charging rates for the images shown in Figure 2.3 (1:4 MDMO-PPV:PCBM film cast from chlorobenzene). Each point in the scatter plots represents a pair of pixels from the image sets. (B) Correlation plot of the 532 nm photoexcitation charging rates versus 850 nm photoexcitation charging rates for the images shown in Figure 2.4 (1:4 MDMO-PPV:PCBM film cast from

toluene). The Pearson correlation coefficient between the pixels is r =0.73. This is a good correlation, and in fact approaches the level of correlation one expects when correlating two identical *experimental* images taken under these conditions. For comparison, Figs A.8C-F show A.8C: perfect correlation (for an image correlated with itself), A.8D: correlation of an image with the same perfectly aligned image with an experimentally meaningful level of noise, A.8E: correlation of the same image against itself but offset by one pixel in x and y, A.8F: the same plot shown in A.8B, with Pearson r = 0.73.

Plotting the charging rates from the images in Figures 2.3 and 2.4 as scatter plots, where the normalized singlet state charging rates (532 nm excitation) are on the y-axis and CT state (850 nm excitation) charging rates are on the x-axis shows how well correlated the images are regardless of excitation wavelength. In Figure A.8A, the scatter plot shows a very tight distribution as expected because of the lack of variation in charging rate structure in the images for films cast from chlorobenzene. The charging rates are uniform and homogeneous throughout, at least within our detection resolution. In Figure A.8B, a strong positive correlation is shown in the scatter plot, showing that the charging rate images are highly correlated regardless of excitation wavelength. Performing a Pearson coefficient calculation results in a coefficient of 0.73 (the closer to 1, the more positively correlated two data sets are), further demonstrating the strong correlation between the two images.

In Supporting Fig. A.8C, we show a range of possible scatter correlation plots. In the first case, when the same image is plotted against itself, perfect correlation results in a straight line with Pearson correlation coefficient 1.0. When we add a meaningful amount of random Gaussian noise of the same standard deviation we see in our own trEFM images, the correlation coefficient is slightly lowered to 0.98, with a marked increase in the distribution of values. The largest change in correlation occurs when we take the same image but shift it by a single pixel in both the x and y (no noise added), dropping the coefficient to 0.77. During normal imaging, drift in the scanning piezo causes the subsequent images to not be in precisely the same location as the original. In our case, the CT excitation image was taken after the singlet excitation image, which causes spatial differences between the two. During post-processing we then try to overlap the two images as best as possible by shifting the CT image. However, this process is imperfect and it is very likely we are not perfectly overlapping the singlet and CT images when computing their correlation.

Combining the random noise from image to image, as well as imperfect overlap, it is reasonable to believe that the correlation between singlet and CT images shown in Figure A.8B are as best as possible.

9. Additional discussion of IQE dependence on excitation wavelength

The local EQE measured by trEFM at any position in the film, $\vec{r}$, can be described as follows:

$$EQE(\vec{r},\lambda) = \alpha(\vec{r},\lambda) * IQE(\vec{r},\lambda) \quad (1)$$

where EQE and IQE are a function of position and excitation wavelength, and α is the absorptivity, also a function of position and wavelength. To compare the local EQE at above and below-gap excitation (532 and 850 nm), we can take the ratio of the two:

$$\frac{EQE(\vec{r},532nm)}{EQE(\vec{r},850nm)} = \frac{\alpha(\vec{r},532nm)*IQE(\vec{r},532nm)}{\alpha(\vec{r},850nm)*IQE(\vec{r},850nm)} \quad (2)$$

Since the absorption at each wavelength in the film is a combination of the contributions from the polymer, fullerene, and interface states, we can then write the absorptivity as

$$\alpha(\vec{r},\lambda) = \sum_i c_i(\vec{r}) * \alpha_i(\lambda) \quad (3)$$

where *i* indexes the different contributions arising from variations in film composition. If we make the reasonable assumptions that at 532 nm the polymer absorption dominates and that only the CT state is responsible for sub-gap absorption, the ratio of EQEs in (2) becomes

$$\frac{EQE(\vec{r},532nm)}{EQE(\vec{r},850nm)} = \frac{c_{polymer}(\vec{r})*\alpha_{polymer}(532nm)*IQE(\vec{r},532nm)}{c_{CT}(\vec{r})*\alpha_{CT}(850nm)*IQE(\vec{r},850nm)} = \left[\frac{c_{polymer}(\vec{r})}{c_{CT}(\vec{r})}\right] * \left[\frac{\alpha_{polymer}(532nm)}{\alpha_{CT}(850nm)}\right] * \left[\frac{IQE(\vec{r},532nm)}{IQE(\vec{r},850nm)}\right] \quad (4)$$

We can ignore the absorption coefficient ratio as we are interested in the spatial variation (*i.e.* the polymer absorption at 532 nm and CT absorption at 850 nm do not change with position). If we also assume, based on our results, that IQE is independent of position or excitation wavelength, the relation becomes

$$\frac{EQE(\vec{r},532nm)}{EQE(\vec{r},850nm)} = \left[\frac{c_{polymer}(\vec{r})}{c_{CT}(\vec{r})}\right] \quad (5)$$

In the case of the well-mixed morphology (film cast from chlorobenzene, Figure 3), it is reasonable to assume that the ratio of polymer to CT state concentration is constant throughout the film, since the polymer and fullerene are spread homogeneously. As a result, the ratio of EQEs is equal to a proportionality constant, and any variations in the measured local EQE arise due to random fluctuations in polymer/fullerene concentration or image error. Indeed, this is what we observe, as clearly depicted in the scatter plot in Supporting Figure A.8, which shows a random distribution of values with no spatial correlation when the trEFM image taken at 532 nm is plotted against the image taken at 850 nm.

For the phase-segregated film, we cannot easily assume that the ratio of polymer to CT state concentration is constant.

$$\frac{EQE(\vec{r},532nm)}{EQE(\vec{r},850nm)} = \left[\frac{c_{polymer}(\vec{r})}{c_{CT}(\vec{r})}\right] * \left[\frac{IQE(\vec{r},532nm)}{IQE(\vec{r},850nm)}\right] \quad (6)$$

We show in Figure 2.4 that the ratio of local EQEs does not vary spatially or with excitation wavelength within the limits of the experiment. This result leaves two possible explanations for our observations: (A) changes in the polymer to CT state absorption ratio are exactly canceled by an equal and opposite change in the ratio of polymer to CT state IQE or (B) the ratio of polymer to CT concentration is constant and IQE is independent of excitation wavelength. Because case (A) is statistically unlikely due to the need for perfect anti-correlation between concentration and IQE, we conclude that case (B) is most likely. Since MDMO-PPV is known to intercalate fullerene,[1] the regions outside of the fullerene domains are a well-mixed combination of MDMO-PPV and PCBM, and the large fullerene aggregates are regularly capped by a skin-like layer of MDMO-PPV,[2] we posit that it is thus *not* unlikely for the concentration of CT states to track with concentration of polymer, even for the film cast from toluene. Therefore, we believe the highly similar distribution of local EQE for both above- and below-gap excitation is indicative of IQE being independent of excitation wavelength.

REFERENCES

1. Wise, A. J.; Precit, M. R.; Papp, A. M.; Grey, J. K. Effect of Fullerene Intercalation on the Conformation and Packing of Poly-(2-Methoxy-5-(3′-7′-Dimethyloctyloxy)-1,4-Phenylenevinylene). *ACS Appl. Mater. Interfaces* **2011,** 3, (8), 3011-3019.

2. Hoppe, H.; Sariciftci, N. S. Morphology of Polymer/Fullerene Bulk Heterojunction Solar Cells. *J. Mater. Chem.* **2006,** 16, (1), 45-61.

FULL AUTHOR LIST FOR REFERENCES WITH MORE THAN 10 AUTHORS

1. Jingbi, Y.; Letian, D.; Yoshimura, K.; Kato, T.; Ohya, K.; Moriarty, T.; Emery, K.; Chen, C.; Gao, J.; Li, G.; Yang, Y. A Polymer Tandem Solar Cell with 10.6% Power Conversion Efficiency. *Nat. Commun.* **2013**, 1446.

4. Chueh, C.-C.; Yao, K.; Yip, H.-L.; Chang, C.-Y.; Xu, Y.-X.; Chen, K.-S.; Li, C.-Z.; Liu, P.; Huang, F.; Chen, Y.; Chen, W.-C.; Jen, A. K. Y. Non-Halogenated Solvents for Environmentally Friendly Processing of High-Performance Bulk-Heterojunction Polymer Solar Cells. *Energy Environ. Sci.* **2013,** 6, 3241-3248.

12. Vandewal, K.; Albrecht, S.; Hoke, E. T.; Graham, K. R.; Widmer, J.; Douglas, J. D.; Schubert, M.; Mateker, W. R.; Bloking, J. T.; Burkhard, G. F.; Sellinger, A.; Fréchet, J. M. J.; Amassian, A.; Riede, M. K.; McGehee, M. D.; Neher, D.; Salleo, A. Efficient Charge Generation by Relaxed Charge-Transfer States at Organic Interfaces. *Nat. Mater.* **2014,** 13, 63-68.

13. Maurano, A.; Hamilton, R.; Shuttle, C. G.; Ballantyne, A. M.; Nelson, J.; O'Regan, B.; Zhang, W.; McCulloch, I.; Azimi, H.; Morana, M.; Brabec, C. J.; Durrant, J. R. Recombination Dynamics as a Key Determinant of Open Circuit Voltage in Organic Bulk Heterojunction Solar Cells: A Comparison of Four Different Donor Polymers. *Adv Mater* **2010,** 22, 4987-92.

15. Schlenker, C. W.; Chen, K.-S.; Yip, H.-L.; Li, C.-Z.; Bradshaw, L. R.; Ochsenbein, S. T.; Ding, F.; Li, X. S.; Gamelin, D. R.; Jen, A. K. Y.; Ginger, D. S. Polymer Triplet Energy Levels Need Not Limit Photocurrent Collection in Organic Solar Cells. *J. Am. Chem. Soc.* **2012,** 134, 19661-19668.

18. Piersimoni, F.; Chambon, S.; Vandewal, K.; Mens, R.; Boonen, T.; Gadisa, A.; Izquierdo, M.; Filippone, S.; Ruttens, B.; D'Haen, J.; Martin, N.; Lutsen, L.; Vanderzande, D.; Adriaensens, P.; Manca, J. V. Influence of Fullerene Ordering on the Energy of the Charge-Transfer State and Open-Circuit Voltage in Polymer:Fullerene Solar Cells. *J. Phys. Chem. C* **2011,** 115, 10873-10880.

41. Hammond, M. R.; Kline, R. J.; Herzing, A. A.; Richter, L. J.; Germack, D. S.; Ro, H.-W.; Soles, C. L.; Fischer, D. A.; Xu, T.; Yu, L.; Toney, M. F.; DeLongchamp, D. M. Molecular Order in High-Efficiency Polymer/Fullerene Bulk Heterojunction Solar Cells. *ACS Nano* **2011,** 5, 8248-8257.

APPENDIX B.

Appendix B accompanies Chapter 3. Mapping Nanoscale Variations in Photochemical Damage of Polymer/Fullerene Solar Cells with Dissipation Imaging.

1. Comparison Between EQE and Absorption Loss

To illustrate the increased reduction in EQE versus absorption, we plot the percent change in EQE (at 450 nm) and absorption (also at 450 nm) as a function of *absorbed* photon dose in Figure B.1. The EQE at each dose is referenced to the fresh device EQE. The absorbed photon dose corrects for the loss in absorbance of the film as it degrades.

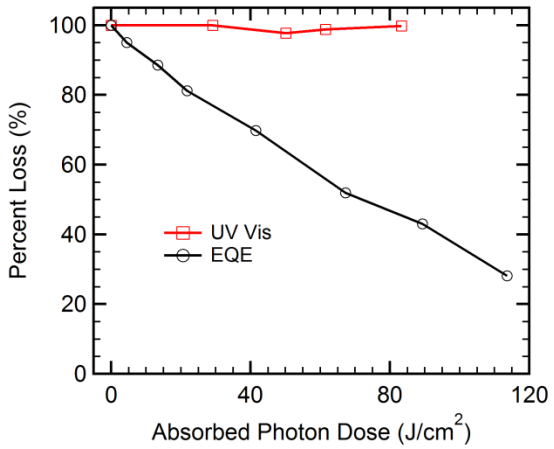

Figure B.1 Percent change of UV-Vis and EQE (at 450 nm) for 3% PTB7:$PC_{71}BM$ devices as a function of absorbed photon dose. The absorbed photon dose accounts for loss in absorbance as the devices degrade.

2. Band Excitation Data: Relationship of Q to FM-EFM Amplitude

To show that amplitude measured via FM-EFM is proportional to Q measured via Band Excitation (BE), we photo-oxidized a 3% DIO PTB7:$PC_{71}BM$ sample through a TEM Grid (PELCO 400 Mesh) to create a sharp step between fresh and degraded areas in the film. We degraded the sample to a photon dose of ~400 J/cm^2 using a 660 nm 5 W LED (LEDEngin LZ10R200). We imaged the sample using FM-EFM and BE on an Asylum Cypher AFM at the

Center for Nanophase Materials sponsored by Oak Ridge National Laboratory. Like our measurements on the MFP-3D BIO system, we applied +10 V to the tip at a lift height of 10 nm during FM-EFM imaging. Due to difficulties with the particular BE hardware used, we applied a tip bias of +7.5 V. Regardless, the images show that cantilever amplitude is proportional to cantilever Q under our imaging conditions.

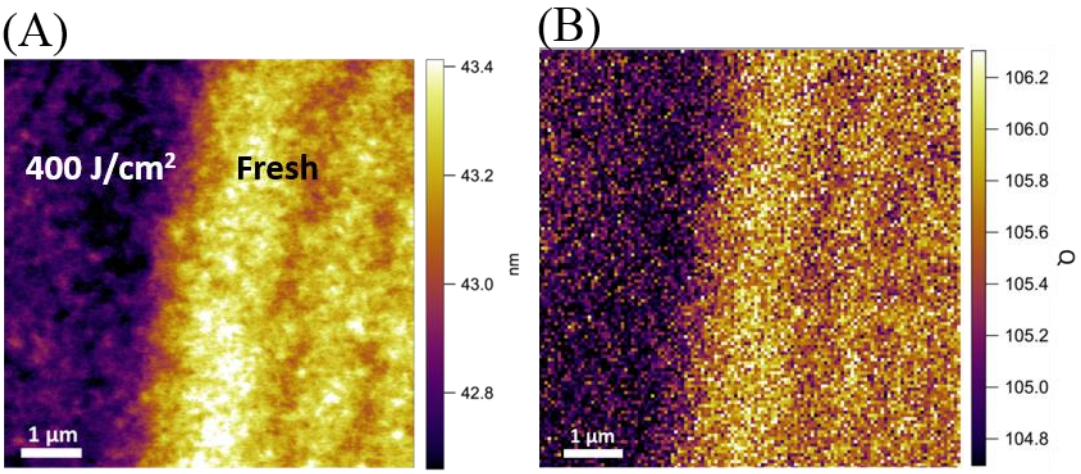

Figure B.2 A comparison between (A) amplitude from FM-EFM and (B) Q from Band Excitation for a 3% DIO PTB7:$PC_{71}BM$ sample photodegraded through a TEM grid using cw 660 nm light.

We report FM-EFM amplitude images as ΔQ/Q to account for variations in drive amplitude from image to image. ΔQ/Q is equivalent to ΔA/A and eliminates the need to measure drive amplitude:

$$\frac{\Delta Q}{Q} = \frac{Q_{eff} - Q_{avg}}{Q_{eff}} = \frac{\frac{A_{eff}}{A_d} - \frac{A_{avg}}{A_d}}{\frac{A_{eff}}{A_d}} = \frac{\frac{A_{eff} - A_{avg}}{A_d}}{\frac{A_{eff}}{A_d}} = \frac{A_{eff} - A_{avg}}{A_{eff}} = \frac{\Delta A}{A} \qquad (1)$$

Here, A_d is the drive amplitude, Q_{eff} and A_{eff} are Q and amplitude of the cantilever at any given pixel in the image, while Q_{avg} and A_{avg} are the average Q and amplitude over the fresh areas of the device. In the case of films photo-oxidized with spots by the HeNe laser, the average amplitude excludes the degraded areas.

3. Sensitivity of Q-Imaging in Photo-Oxidative Studies

To provide evidence for the sensitivity of Q-imaging compared to SKPM in photodegraded OPVs, we carried out an additional *in situ* photo-oxidation experiment where a sample was exposed to a 633 nm HeNe laser (5 mW Research Electro-Optics) at ~5030 W/m^2 for photon doses ranging from ~600 to 3000 J/cm^2. SKPM images were taken both in the dark and under 660 nm illumination (5060 W/m^2 LEDEngin). Even for doses up to 3000 J/cm^2, differences in sample work function are difficult to discern.

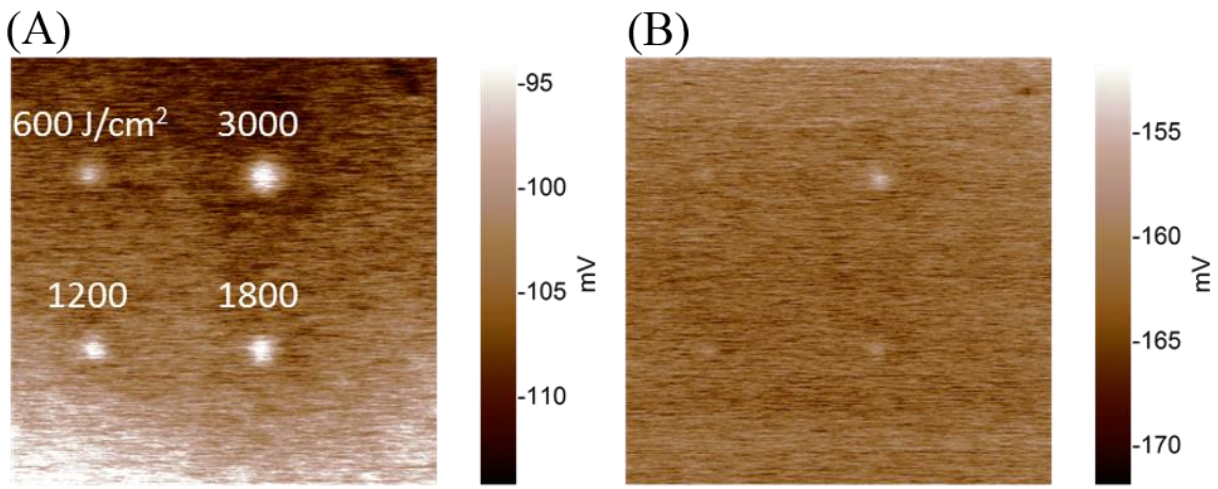

Figure B.3 Changes in tip bias measured via amplitude-feedback SKPM for a 3% DIO PTB7:$PC_{71}BM$ sample photo-oxidized *in situ* with cw 633 nm laser at ~5030 W/m^2 for photon doses ranging from ~600 to 3000 J/cm^2 in (A) dark and (B) 660 nm illumination. Images are 20x20 microns.

On the same sample in Figure B.3, we collected a ΔQ/Q image to show that when the sample is degraded past its functional lifetime, the sign of ΔQ/Q changes and Q begins to rise in the degraded areas. At high enough doses, Q actually exceeds that of a fresh film. This is important to note as it essentially means the relationship between ΔQ/Q and external quantum efficiencies that we show in Figure 3.3 breaks down once the device has been degraded past normal functionality. Care must be taken in degrading to reasonable photon doses when comparing local FM-EFM results with bulk device measurements.

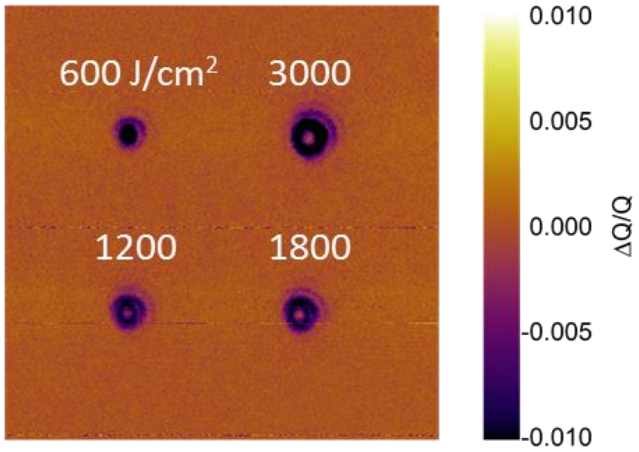

Figure B.4 The ΔQ/Q image of a 3% DIO PTB7:$PC_{71}BM$ sample photo-oxidized *in situ* with cw 633 nm laser at ~5030 W/m^2 for photon doses ranging from ~600 to 3000 J/cm^2. Image is 20x20 microns.

4. Table of Cantilever Constants

Table B.1 Manufacturer reported constants for the cantilevers used in this study.

	Resonance Frequency	Spring Constant	Quality Factor*
Multi75-G	75 ± 15 kHz	3 N/m	164
Tap190-G	190 ± 60 kHz	48 N/m	391
Tap300-G	300 ± 100 kHz	40 N/m	508

*Experimentally determined.

5. Additional Images

The photo-oxidation images shown in Figure 3.5 and Figure 3.6 were also taken at higher photon doses (800, 1200, 1800, and 3000 J/cm^2) to assess the evolution of photochemical damage throughout the lifetime of the device. We chose to display only the fresh and 400 J/cm^2 images to highlight the most important differences between PTB7:PC$_{71}$BM films made with and without DIO. Figure B.5 (DIO) and Figure B.6 (no DIO) show the images over the entire range of photon dose.

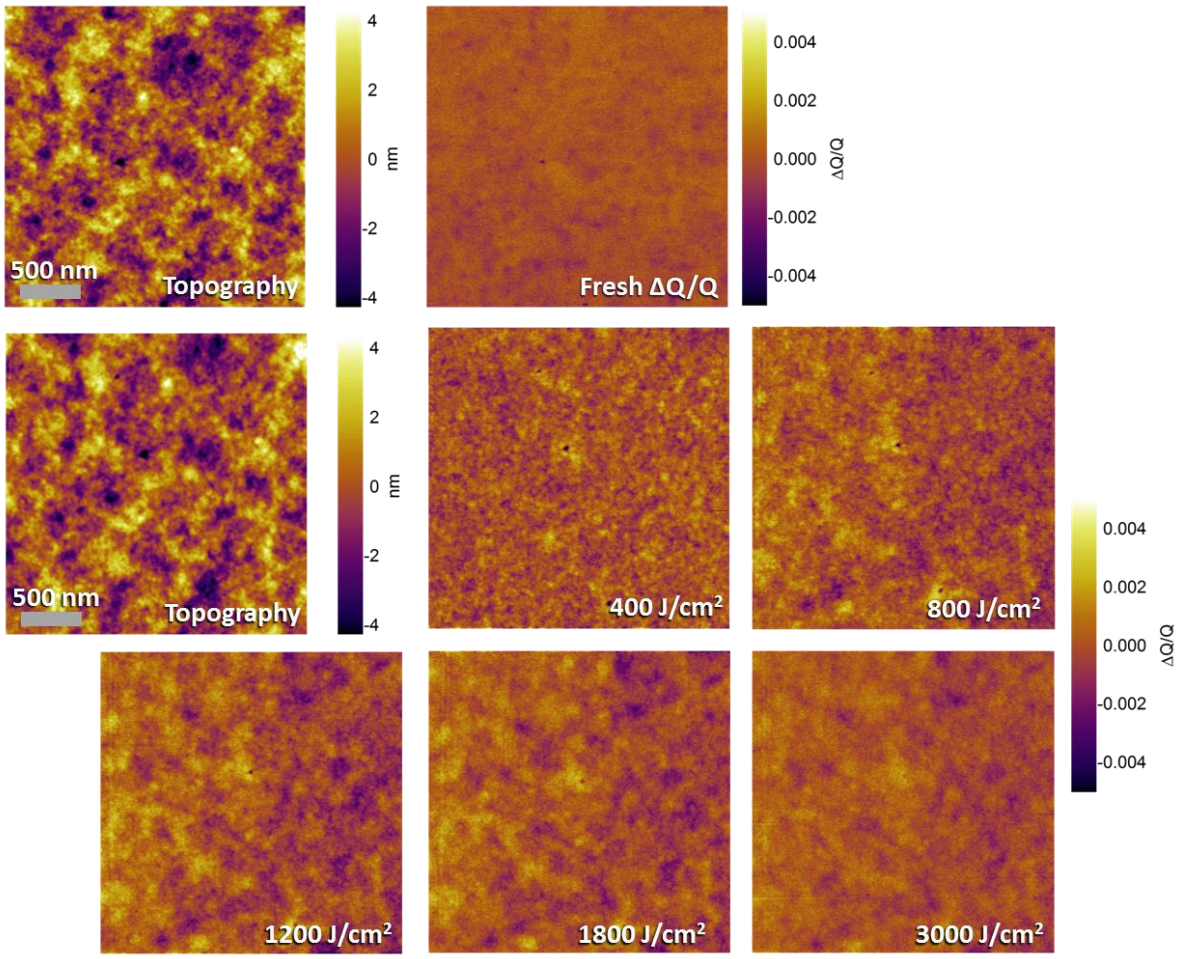

Figure B.5 Topography and ΔQ/Q for all photon doses (0, 400, 800, 1200, 1800, 3000 J/cm^2) of a 3% DIO PTB7:PC$_{71}$BM film photo-oxidized *in situ* with a 660 nm LED.

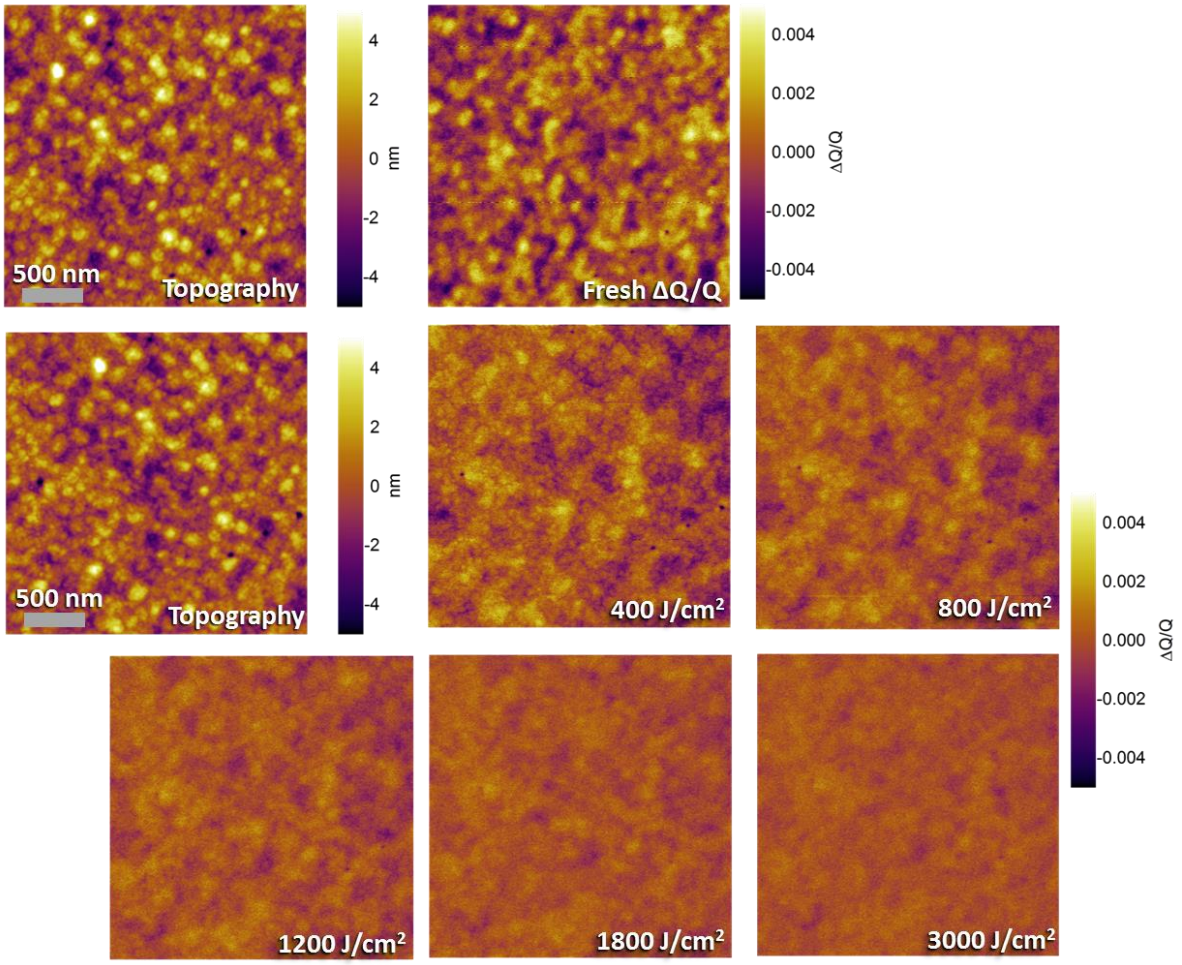

Figure B.6 Topography and ΔQ/Q for all photon doses (0, 400, 800, 1200, 1800, 3000 J/cm^2) of a 0% DIO PTB7:$PC_{71}BM$ film photo-oxidized *in situ* with a 660 nm LED.

6. Evolution of Q Distribution in PTB7:$PC_{71}BM$ Films Processed With and Without DIO

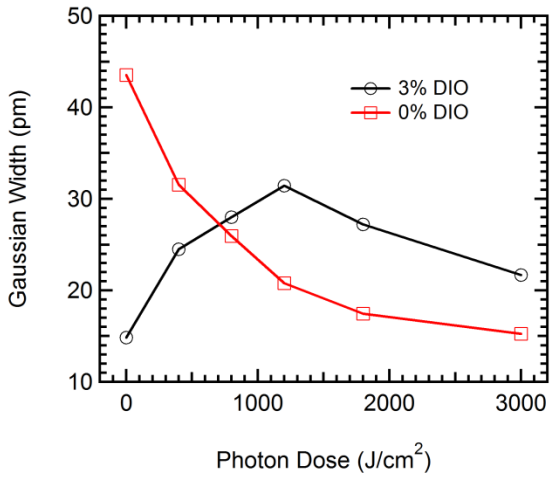

Figure B.7 Distribution of amplitudes measured by FM-EFM as a function of photon dose for PTB7:$PC_{71}BM$ films processed with and without DIO.

To more quantitatively assess the distribution of Q changes seen in photo-oxidizing PTB7:$PC_{71}BM$ films processed with and without DIO, we fit a histogram of flattened FM-EFM amplitude images from figures B.5 and B.6 (not converted to $\Delta Q/Q$ in this case) with a Gaussian and then plotted the value of the Gaussian width of each image against photon dose. The greater the variation in tip amplitude over the image, the greater the Gaussian width (i.e. a uniformly performing device would have a very small Gaussian width).

7. Comparison between 0% and 3% DIO PTB7:$PC_{71}BM$ EQEs as a function of photon dose.

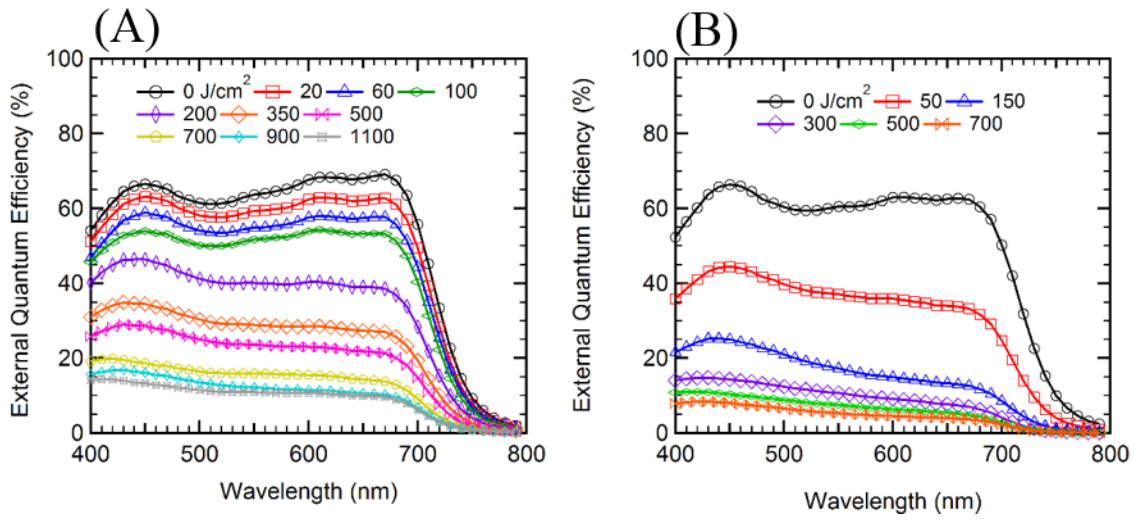

Figure B.8 External quantum efficiencies of PTB7:$PC_{71}BM$ processed (A) with and (B) without DIO photo-oxidized over photon doses ranging from 0 to 1100 J/cm^2.

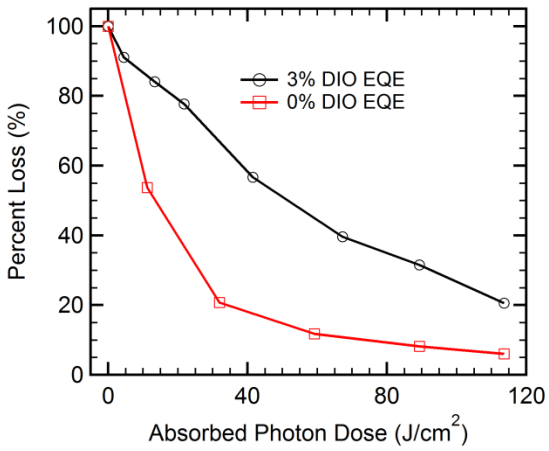

Figure B.9 A comparison between the % change in EQE at 660 nm of 0% and 3% DIO PTB7:$PC_{71}BM$ devices as they are subjected to increasing photon doses.

We show in Figure B.8 and Figure B.9 the difference in stabilities between PTB7:$PC_{71}BM$ devices processed with and without DIO. Devices processed without DIO degrade at a faster rate. We note that the devices made with 0% DIO were fabricated using a different batch of PTB7

polymer from 1-Material and, despite the exact same processing conditions, resulted in a higher performing device. We do not believe this affects the stability of the devices. Figure B.9 shows the percent loss in EQE as a function of photon dose for both 0% and 3% DIO devices. We did this by calculating the %-difference from the fresh device for each photon dose and then plotting it against the *absorbed* photon dose. The absorbed photon dose corrects for the loss in absorbance of the film as it degrades.

APPENDIX C.

This appendix accompanies Chapter 4. Dissipation Imaging *via* Cantilever Ringdown for the Study of Loss Processes in Polymer/Fullerene Solar Cells.

1. Comparisons between FM-EFM and ringdown imaging.

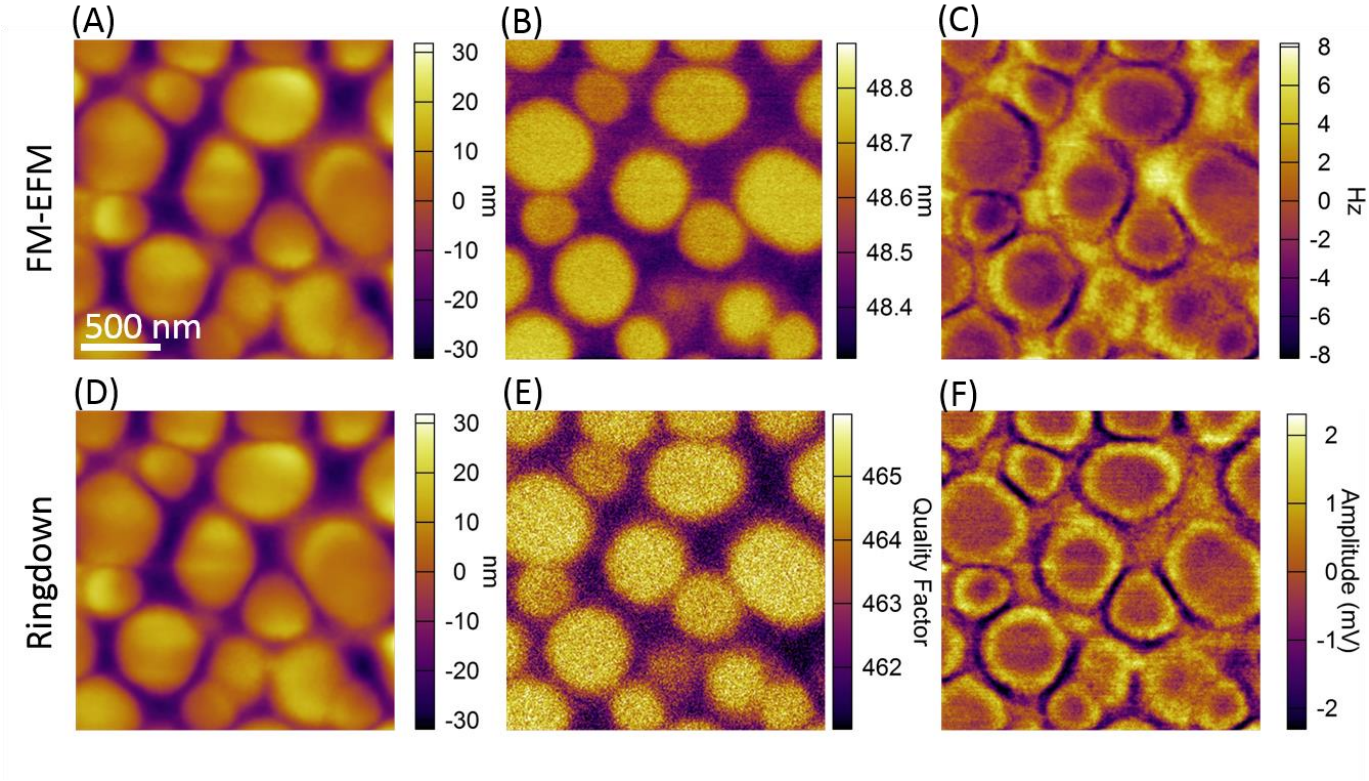

Figure C.1 (A-C) FM-EFM images of topography, lift amplitude and lift frequency, respectively of a fresh no additive 1:3 PTB7:$PC_{71}BM$ film. (D-E) Ringdown images of topography, cantilever Q, and amplitude shift of the same film in the same area.

Figure C.1 shows a comparison between images obtained using frequency-modulated electrostatic force microscopy and ringdown imaging of the same no additive 1:3 PTB7:$PC_{71}BM$ film prior to photo-oxidation. There is no difference in the implementation of the topography pass for the two imaging techniques, resulting In identical topography images. In FM-EFM, the lift amplitude (Figure C.1B) during the second pass is proportional to Q by A over A_d, where A is the

amplitude of the cantilever and A_d is the drive amplitude of the shake piezo. Because the drive amplitude is very difficult to measure, FM-EFM amplitude images cannot be converted directly into Q and are instead left in units of amplitude and used as qualitative dissipation maps. The drawback here is system drift causes the cantilever amplitude to change from one image to another, making quantitative comparisons between images or different samples impossible. Figure C.1C shows the lift frequency, which is simply a measure of how much the drive frequency needed to shift in order to keep the cantilever at the peak of its resonance curve due to electrostatic differences that occur as a result of the local variations in film performance. Typically we do not see significant changes in resonance frequency as a result of film degradation, and only see significant spatial changes in the Q/dissipation images.

Figure C.1D-F show the corresponding images taken with our implementation of ringdown imaging to their FM-EFM counterparts. Figure C.1E is actual cantilever Q, and can be used in quantitative comparisons over multiple images or samples, and can further be used to calculate cantilever power dissipation with Eq. 2. Interestingly, the shifts in cantilever resonance as a response to local performance variations are retained in the amplitude shift of the cantilever ringdown, i.e. the amplitude of the cantilever prior to turning off the driving force. This makes sense as any changes in cantilever resonance curve will cause not only changes in resonance frequency but also amplitude. Therefore it makes sense that the changes in amplitude would reflect those seen in the frequency shifts obtained when using a phase-locked feedback loop to keep the cantilever at resonance.

2. Full EQE Spectra for 3% DIO 1:1.5 and No Additive 1:3 PTB7:$PC_{71}BM$ Films as a Function of Photon Dose

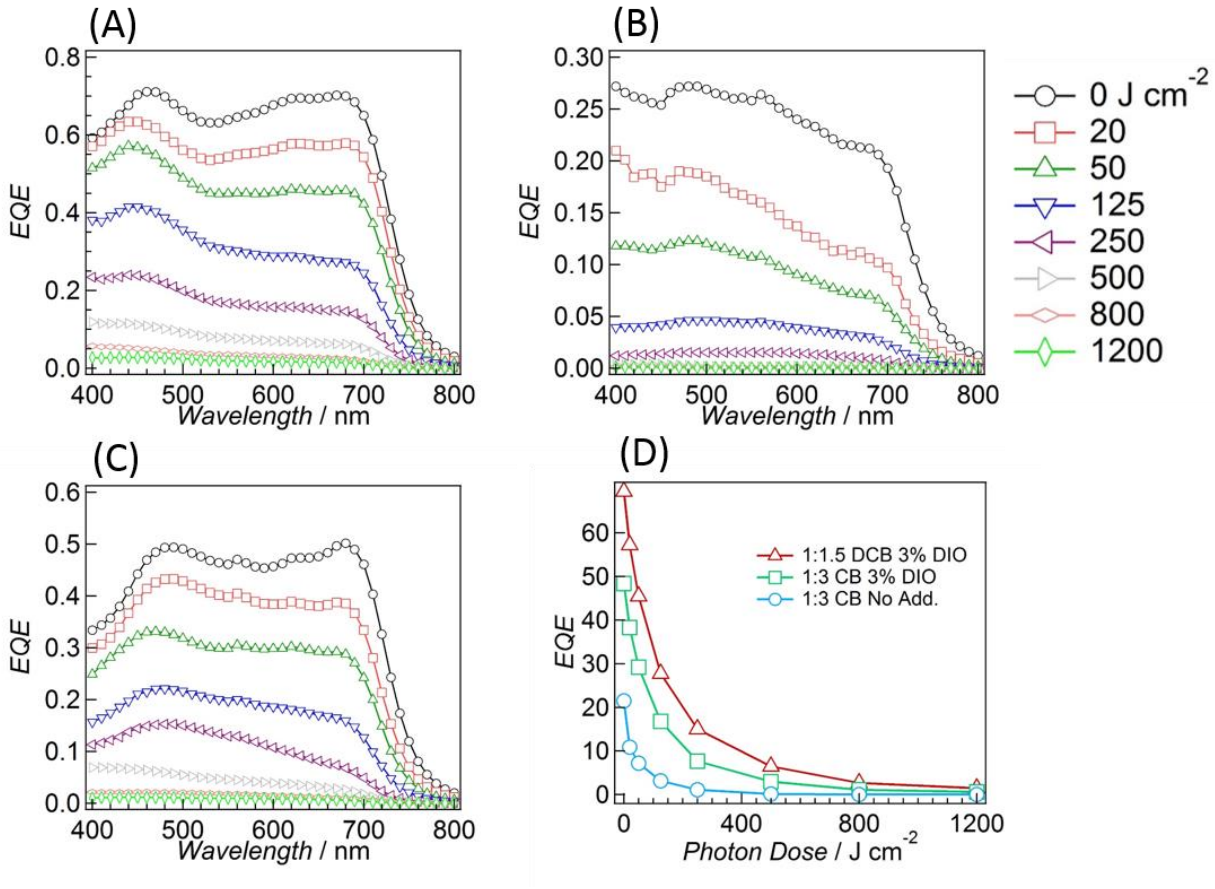

Figure C.2 EQE spectra of completed devices subjected to a range of photon doses ranging from 0 to 1200 J/cm^2. (A) 3% DIO 1:1.5 from DCB, (B) no additive 1:3 PTB7:$PC_{71}BM$ from CB, and (C) 3% DIO 1:3 PTB7:$PC_{71}BM$ from CB. (D) EQEs at 660 nm for all types of device on a linear scale as a function of photon dose.

Figure C.2 shows the full EQE spectra as a function of wavelength for the 3% DIO 1:1.5 and no additive 1:3 films used in this study. The extremely low EQEs seen in Figure C.2B for doses past 125 J/cm^2 were collected using lock-in detection EQE for increased signal to noise. Figure C.2C shows the non-normalized EQEs at 660 nm for both types of device.

3. Full Q versus photon dose curves for local dissipation measurements shown in Figure 4.3.

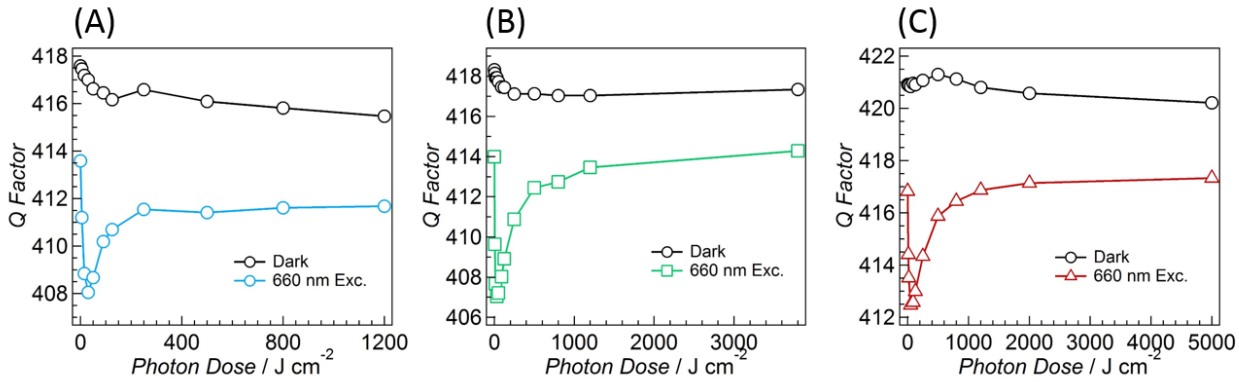

Figure C.3 Full Q versus photon dose curves obtained for (A) 1:3 from CB, (B) 1:3 3% DIO from CB, and (C) 1:1.5 3% DIO from DCB PTB7:$PC_{71}BM$ films.

Figure C.3 shows the full Q versus photon dose curves obtained during ringdown imaging to accompany Figure 4.3. Q values were obtained out to high doses where changes in Q were minimal and show that for sufficiently high doses the value of Q essentially no longer changes past the functional lifetime of the device.

4. Full cantilever power dissipation versus photon dose curves for local dissipation measurements shown in Figure 4.3.

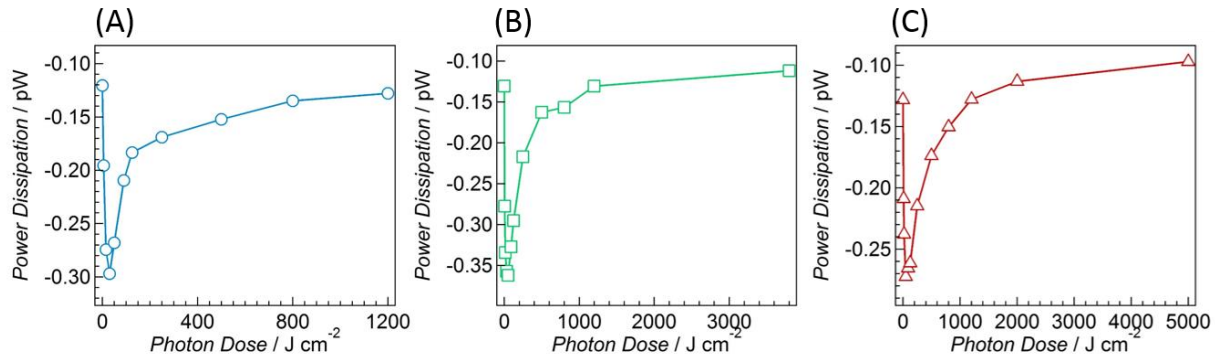

Figure C.4 Full cantilever power dissipation versus photon dose curves obtained for (A) 1:3 from CB, (B) 1:3 3% DIO from CB, and (C) 1:1.5 3% DIO from DCB PTB7:$PC_{71}BM$ films.

Figure C.4 shows the full power dissipation versus photon dose curves collected for each morphology studied. Per equation 4.3, each point is calculated using $Q_{surface}$ and $Q_{+10V,light}$ for each step of degradation. The tip amplitude is taken to be the average amplitude before the driving force is turned off. The spring constant and cantilever resonance frequency (as well amplitude invOLS) are measured prior to imaging.

5. High resolution images of 1:1.5 3% DIO and 1:3 3% DIO PTB7:$PC_{71}BM$ films.

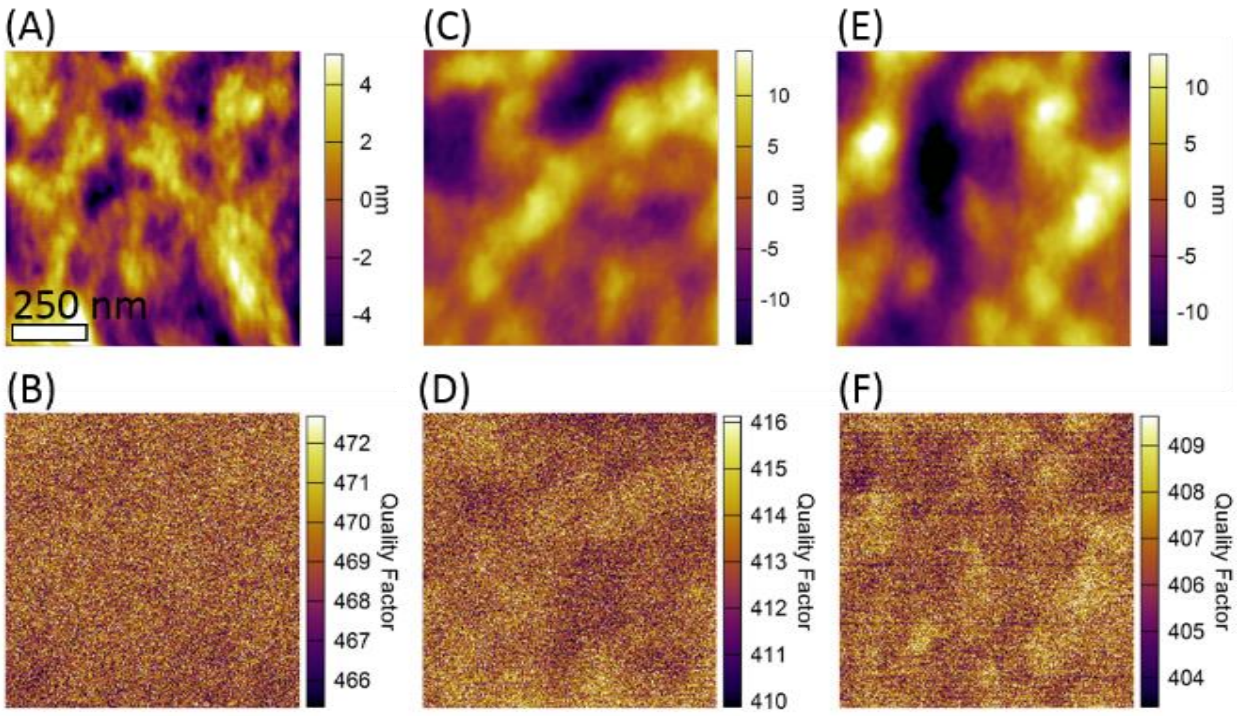

Figure C.5 (A) Topography and (B) ringdown Q image of a fresh, undamaged 1:1.5 3% DIO from DCB PTB7:$PC_{71}BM$. (C) Topography and (D) ringdown Q image of a fresh, undamaged 1:3 3% DIO from CB PTB7:$PC_{71}BM$. (E) Topography and (F) ringdown Q image of the same 1:3 3% DIO from CB PTB7:$PC_{71}BM$ film degraded to 20 J/cm^2. Each image is 1 μm^2, 256 x 256 pixels, 1 average per pixel.

Figure C.5 shows the topography and ringdown Q images of the two films cast using DIO. In both cases, the resulting Q image is highly homogeneous with little to no variation in the distribution of cantilever dissipation as a function of film morphology. The use of DIO reduces both structural and dissipative heterogeneity in the films, resulting in higher performing and more stable devices. Even after degrading the 1:3 film from CB with 3% DIO to 20 J/cm^2 as shown in Figure C.5F, very little heterogeneity appears in the Q image.

VITA

EDUCATION

2016 Ph.D. Chemistry – University of Washington

Advisor: Prof. David S. Ginger

2011 B.S. Chemistry/Chemical Physics – Pacific University

Advisor: Prof. Kevin E. Johnson

PUBLICATIONS

6. Giridharagopal, R.; **Cox, P.A.**; Ginger, D.S.; Advances in Local Characterization of Energy Materials by Scanning Probe Microscopy. *Accounts of Chemical Research*. (In Preparation).

5. **Cox, P.A.**; Flagg, L.A.; Giridharagopal, R.; Ginger, D.S.; Dissipation Imaging *via* Cantilever Ringdown for the Study of Loss Processes in Polymer/Fullerene Solar Cells. (In Preparation)

4. Bleecker, J.V.; **Cox, P.A.**; Keller, S.L.; Thickness differences between Lo and Ld bilayers do not uniquely determine mixing temperatures. *Biophys J* (Submitted)

3. Bleecker, J.V.; **Cox, P.A.**; Foster, R.N.; Litz, J.P.; Blosser, M.C.; Castner, D.G.; Keller, S.L.; Thickness Mismatch of Coexisting Liquid Phases in Non-Canonical Lipid Bilayers. *J. Phys. Chem. B.* **2016** DOI: 10.1021/acs.jpcb.5b10165.

2. **Cox, P.A.**; Glaz, M.S.; Harrison, J.S.; Peurifoy, S.R.; Coffey, D.C.; Ginger, D.S.; Imaging Charge Transfer State Excitations in Polymer/Fullerene Solar Cells with Time-Resolved Electrostatic Force Microscopy. *J. Phys. Chem. Lett.* **2015** DOI: 10.1021/acs.jpclett.5b01360 ***(Selected for ACS Editor's Choice)***

1. **Cox, P.A**.; Waldow, D.A.; Dupper, T.J.; Jesse, S.; Ginger, D.S.; Mapping Nanoscale Variations in Photochemical Damage of Polymer/Fullerene Solar Cells with Dissipation Imaging. *ACS Nano* **2013** DOI: 10.1021/nn404920t

AWARDS AND HONORS

Larry R. Dalton Fellowship in Chemistry (Awarded Twice)	2015
Larry R. Dalton Fellowship in Chemistry	2013
Graduate School Fund for Excellence and Innovation Travel Award	2013
Rowland Endowed Fellowship	2011
NASA Oregon Space Grant Consortium Undergraduate Achievement Award	2011
Outstanding Senior in Chemistry *(Awarded to top senior in chemistry)*	2011
Grey Gown Flag Bearer (*Awarded to top 10 GPA in junior year*)	2010
Boxer Spirit Scholarship	2010
Boxer Experience Award	2009
McGill Scholarship	2009
Outstanding General Chemistry Student	2008
Presidential Merit Scholarship	2007
Dean's List	2007-2011